

# **TOMOGRAPHIC INVESTIGATION OF THE CRUST OF CENTRAL JAVA, INDONESIA**

Dissertation  
zur Erlangung des Doktorgrades  
der Mathematischen-Naturwissenschaftlichen Fakultät  
der Christian-Albrechts-Universität zu Kiel

vorgelegt von

Diana Wagner

Kiel, 2007

Referent:

Korreferentin:

Tag der mündlichen Prüfung:

Zum Druck genehmigt:

Prof. Dr. W. Rabbel

Prof. Dr. H. Kopp

9. Juli 2007

Kiel, den 9. Juli 2007

Der Dekan

# TABLE OF CONTENTS

ABSTRACT .....	I
ZUSAMMENFASSUNG .....	III
1. INTRODUCTION.....	1
2. THE SUNDA ARC .....	7
2.1 The Tectonic Setting .....	7
2.2 Seismicity .....	10
2.3 Volcanism Along the Sunda Arc.....	13
3. THE MERAMEX DATA SET .....	17
4. CRUSTAL STRUCTURE SOUTH OF CENTRAL JAVA .....	23
4.1 Forward Modeling of OBH Data .....	23
4.2 Gravity Modeling .....	31
5. TOMOGRAPHIC COMPARISON STUDY .....	33
5.1 Introduction .....	33
5.2 The Techniques .....	34
5.2.1 Code LOTOS-06 .....	34
5.2.2 Code 3DTH .....	36
5.3 Resolution Tests of the Active Data set .....	38
5.4 Results .....	41
5.5 RMS Travel Time Residuals .....	50
5.6 Discussion and Conclusions .....	53

6. SEISMIC STRUCTURE OF CENTRAL JAVA .....	55
6.1 Introduction .....	55
6.2 3D Tomographic Studies of Active Seismic Data .....	57
6.3 The Java Earthquake and its Aftershocks .....	63
6.4 Summary and Discussion .....	66
7. JOINT INVERSION OF ACTIVE AND PASSIVE SEISMIC DATA.....	69
7.1 Introduction .....	69
7.2 The Algorithm .....	73
7.3 Results .....	75
7.3.1 Active Data Inversion.....	75
7.3.2 Passive Data Inversion .....	77
7.4 Synthetic Tests .....	80
7.5 Discussion and Conclusions.....	81
8. GEOPHYSICAL AND GEOCHEMICAL INSIGHTS INTO FORMATION OF A LARGE MAGMATIC SYSTEM IN CENTRAL JAVA, INDONESIA .....	87
8.1 Introduction .....	87
8.2 Results .....	88
8.3 Interpretation .....	93
9. CONCLUDING REMARKS .....	95
10. REFERENCES.....	99
APPENDIX A: Seismic sections.....	107
APPENDIX B: OBH stations.....	115
APPENDIX C: Tables.....	119
ACKNOWLEDGEMENTS .....	125
CURRICULUM VITAE .....	127

## **ABSTRACT**

Seismic and volcanic activity in Central Java, Indonesia, is directly or indirectly related to the subduction of the Indo-Australian plate beneath the Sunda plate. The MERAMEX project (MERapi AMphibious EXperiments) studied the relationship between subduction zone processes and arc volcanism in Central Java, as manifested in the active strato-volcano Merapi. In May 2004, a temporary seismological network was installed around Merapi volcano to monitor natural seismic activity. Simultaneously, Ocean Bottom Hydrophones (OBH) and Seismometers (OBS) were deployed during RV Sonne cruise SO176 to extend the land network offshore. The second cruise in September/October 2004, SO179, acquired seismic refraction and reflection profiles, bathymetric, gravimetric, and magnetic data. Two dip lines extend from close to the coast across the trench onto the oceanic plate. A coast-parallel profile was located about 50 km off the south coast of Java. The airgun signals of the three profiles were recorded both at OBH stations deployed along the seismic profiles and within the onshore receiver array. The additional recording of the marine seismic experiments onshore Central Java resulted in the onshore elongation of the profiles. This provided constraints on the tectonic setting of the subduction zone in three dimensions.

The reflection and refraction data of the three seismic profiles were modeled using a 2D forward modeling technique that made it possible to develop a detailed model of the forearc region and the descending oceanic plate. The P-wave velocity information was used to generate background velocity models for the tomographic calculations. Tomographic inversions of the active onshore data were performed using the 3DTH (Hole 1992) and LOTOS-06 (Koulakov et al. 2007) code and the results of each method were compared. Additionally, the onshore active data and local earthquakes were also jointly inverted using LOTOS-06.

The tomographic models show a low-velocity structure aligned in a NNE-SSW direction that separates the rigid forearc into two blocks. The hypocenter of the May 26, 2006 Java magnitude  $M_w=6.4$  earthquake and its aftershocks are concentrated along the eastern edge of this elongated low-velocity zone which can be described as a weakened zone of the seismogenic crust.

The most important feature in the tomographic models is an anomalously-strong low-velocity anomaly located in the backarc crust just north of the volcanoes Sumbing, Merapi and Lawu. The main anomaly extends about 80 km in an EW and 30 km in a NS direction,

and over 50 km in depth. The velocity perturbations, the attenuation of P- and S- waves, the high Poisson's ratio of 0.3, its correlation with a gravity low and the location in the active Sunda Arc, all suggest that the low-velocity anomaly is caused by multiple magma reservoirs and ascending feeder systems below the volcanoes of Central Java.

## ZUSAMMENFASSUNG

Seismische und vulkanische Aktivitäten in Zentraljava, Indonesien, sind direkt oder indirekt mit der Subduktion der indo-australischen Platte unter die Sundaplatte verbunden. Das MERAMEX- (AMphibious MERapi EXperiment) Projekt untersuchte die strukturellen Wechselbeziehungen zwischen dem Bogenvulkanismus, insbesondere des Stratovulkans Merapi, und der Subduktionszone im Bereich von Zentraljava. Um die natürliche Seismizität im Subduktionsbereich zu erfassen, wurde im Mai 2004 ein temporäres seismologisches Netzwerk (onshore) um den Vulkan Merapi installiert. Gleichzeitig wurden Ozeanbodenhydrophone (OBH) und -seismometer (OBS) während der Sonne-Ausfahrt SO176 eingerichtet, um das Landnetzwerk zu erweitern. Die zweite Ausfahrt SO179 im September/Oktober 2004 diente der Akquisition refraktions- und reflexionsseismischer Profile, bathymetrischer, gravimetrischer und magnetischer Daten. Zwei Profile reichten von der Südküste Javas über den Tiefseegraben bis zur ozeanischen Platte. Ein weiteres Profil befand sich in einem Abstand von etwa 50 km parallel zur Küste Zentraljavas. Die Airgunsignale aller drei Profile wurden sowohl mit Ozeanbodeninstrumenten als auch im Landnetzwerk aufgezeichnet. Mit Hilfe der zusätzlichen Registrierung der marinen Seismik an Land wurden die Seeprofile ins Landesinnere fortgesetzt und die Subduktionszone dreidimensional abgebildet.

Aus den reflexions- und refraktionsseismischen Daten wurde interaktiv ein detailliertes Geschwindigkeits-Tiefen-Modell der Forearcregion und der abtauchenden ozeanischen Platte in zwei Dimensionen entlang der drei seismischen Profile entwickelt. Die P-Wellengeschwindigkeitsinformationen stellten die Basis für die Hintergrundmodelle der tomographischen Berechnungen dar. Tomographische Inversionen der aktiven Landdaten wurden mit den Codes 3DTH (Hole 1992) und LOTOS-06 (Koulakov et al. 2007) durchgeführt und deren Ergebnisse miteinander verglichen. Außerdem wurden die aktiven Landdaten und Lokalbeben gemeinsam mit dem Code LOTOS-06 invertiert.

Die tomographischen Modelle zeigen eine Niedriggeschwindigkeitsstruktur, die sich in NNE-SSW Richtung erstreckt und den rigiden Forearc in zwei Blöcke teilt. Das Hypozentrum des Java Erdbebens mit der Magnitude  $M_w=6.4$  vom 26. Mai 2006 und dessen Nachbeben häufen sich entlang des östlichen Randes dieser ausgedehnten Niedriggeschwindigkeitszone an, die als geschwächte Zone der seismogenen Kruste bezeichnet werden kann.

Das Hauptergebnis der tomographischen Modelle ist eine ungewöhnlich starke Niedriggeschwindigkeitsanomalie, die sich nördlich der Vulkane Sumbing, Merapi und Lawu in der

Backarckruste befindet. Die Hauptanomalie erstreckt sich 80 km in EW-, 30 km in NS-Richtung und über 50 km in die Tiefe. Die Geschwindigkeitsperturbationen, die Dämpfung der P- und S-Wellen, das hohe Poissonverhältnis von 0,3, die Übereinstimmung mit einem gravimetrischen Tief und die Lokation am aktiven Sundabogen suggerieren, daß die Niedriggeschwindigkeitsanomalie durch multiple Magmenreservoirire und Aufstiegspfade unter den Vulkanen Zentraljavas verursacht wird.

## 1. INTRODUCTION

The Sunda Arc is a classical example for an active convergent plate margin, a destructive plate boundary, where the Indo-Australian oceanic plate is subducted beneath the overriding continental Eurasian plate (Figure 1.1 & 2.1). Seismic and volcanic activity is very high along this margin resulting in great interest in understanding the subduction zone processes related to natural hazards, such as the generation of earthquakes, tsunamis and volcanic activity. The island of Java, Indonesia, which represents the research area in this study, is situated along the active Sunda Arc (Figure 1.1) and was confronted with several natural hazards within the last years:

On July 17, 2006 a devastating tsunami earthquake occurred with a magnitude of  $M_w=7.7$  in the southwest of Java at  $9.25^\circ$  S and  $107.41^\circ$  E (source NEIC earthquake catalogue 2007) (Ammon et al. 2006; Fujii & Satake 2006). The earthquake had thrust-faulting character and occurred on the shallow part of the plate boundary in 20 km depth, about 50 km north of the Java trench (Figure 1.1 & 2.2). Run-up heights of 5-8 m along the southern coast of central Java to Yogyakarta caused intensive damages and killed over 600 people (Ammon et al. 2006). The tsunami was generated by a rupture propagating about 200 km along the trench and causing a slip of about 2.5 m (Ammon et al. 2006; Fujii & Satake 2006).

In mid-May 2006, villages located within a radius of seven to eight kilometers to the summit of Merapi volcano were evacuated because of highly increased rates of volcanic tremors, dome growth and rock falls. On May 26, 2006 a destructive magnitude  $M_w=6.4$  earthquake (Global CMT catalogue 2007) occurred in the Yogyakarta district (Figure 1.1 & 2.2). The hypocenter was located in the coastal area at shallow depth within the overriding Sunda plate (at  $8.03^\circ$  S and  $110.54^\circ$  E) and showed a strike-slip mechanism. The epicentral area of the May 26, 2006 earthquake suffered from intensive damages causing more than 5,800 fatalities, 30,000 injured and over 200,000 homeless people. The small distance between Merapi volcano and the epicentral area of the earthquake suggests a possible linkage between the volcano and the recent strong earthquake. Ash layers and fluvial sediments constitute the soil conditions in the area of Yogyakarta. Therefore, site effects probably contributed to the severe damage. After the occurrence of the so-called Java earthquake, the local observatory BPPTK (former Merapi Volcano Observatory MVO) observed higher ex-

trusion rates and volumes of the collapsed material at Merapi volcano. It was found that the earthquake enhanced the volcanic activity by a factor of three. Growth of the lava dome continued to the southeast, causing a collapse of parts of the eastern crater rim and releasing more than 100 pyroclastic flows (Awan Panas) per day. On June 14, 2006 the dome collapsed releasing a south-directed pyroclastic flow of 7 km length, destroying houses and farmland of the village Kali Adem. Although the village was evacuated shortly before the pyroclastic flow, two persons died.

A thrust earthquake on June 02, 1994 with a magnitude of  $M_w=7.8$  located off the southeastern coast of Java near the east end of the Java trench at  $11.03^\circ$  S and  $113.04^\circ$  E (Figure 1.1& 2.2) in a depth of 15 km, generated a devastating tsunami with run-up heights of 14 m (Tsuji et al. 1995). The tsunami killed more than 250 people. The Java earthquake probably resulted from a slip over a locked seamount (Abercrombie et al. 2001).

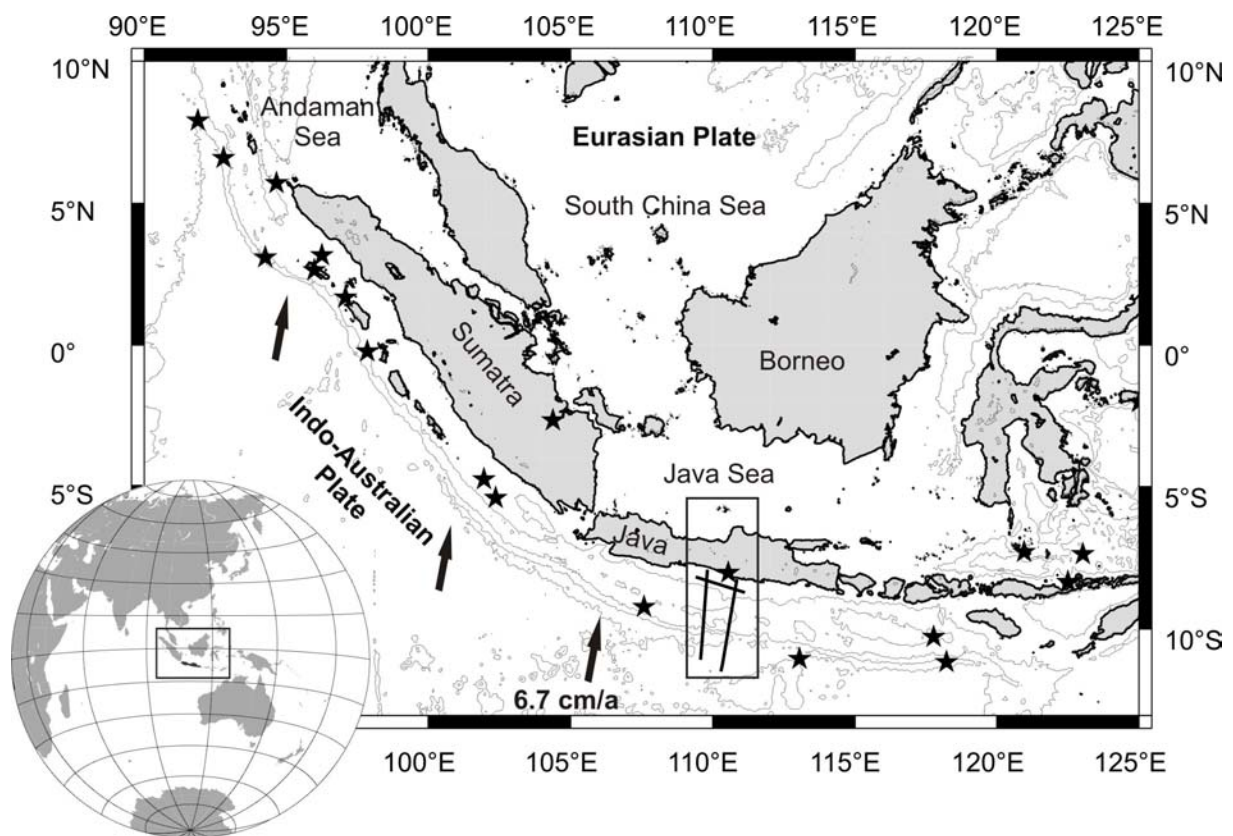


**Figure 1.1:** Geographic map of Indonesia showing the main topographic units where the Indo-Australian plate is subducted beneath the Eurasian plate. The rectangle marks the study area of the MERAMEX project in Central Java. The stars mark major earthquakes which occurred between 1976 and 2007 with magnitude  $M_w > 7$  with one exception: the May 26, 2006 magnitude  $M_w=6.4$  event located within the study area of the MERAMEX project.

The results presented in this study contribute to the understanding of the tectonic structure of the subducting oceanic and overriding Sunda plate and link the subduction processes to the active volcanism and earthquake activity in Central Java:

First of all, the seismic investigation of the tectonic regime off Central Java yielded a three-dimensional structural model of the subduction zone (Chapter 4) including the velocity-depth distribution and the layer thickness along the seismic profiles. The linkage between subduction and earthquake activity as well as volcanism was mainly achieved by seismic tomography, a technique similar to a medical CAT scan which derives three-dimensional images from the processing of the integrated properties of the medium that rays encounter along their paths through it. Seismic tomography is based on perturbation theory, therefore preliminary one-dimensional velocity-depth models are required as a basis of the tomographic studies. The one-dimensional models serve as a background velocity model to which the tomographically determined velocity perturbations apply. Three-dimensional tomographic images of the Central Javan crust were produced on the basis of two different data sets:

- a) airgun shots as source positions in combination with the onshore receiver array and
- b) local earthquakes as natural sources in combination with the on- and offshore receiver array.

Data set a) has the advantage that both source and receiver positions are well known in contrast to the location of the natural sources (b) and provides, therefore, images with a higher accuracy in the upper crust. The differences are discussed in detail in Chapter 7.

The three-dimensional tomography of the active seismic data (data set (a)) revealed two distinct low-velocity anomalies in the crust of Central Java which can be related to the active volcanism and the earthquake activity (Chapter 6):

1. A northeast-southwest elongated anomaly separates the rigid forearc into two blocks. When represented at a small scale, there seems to be a correlation between the edge of the low-velocity zone in-between the two rigid blocks and the likely location of the hypocenter of the destructive Java earthquake in May 2006. In order to understand this tectonic framework, the aftershocks of the May 2006 event were analysed in regard of the tomographic results. This study shows that the events and its aftershocks cluster at the eastern edge of this elongated low-velocity zone in the Gunung Kidul mountains in Central Java and not as expected along the Opak fault.

2. One large anomaly is located along the footprint of the volcanic arc. However, the active seismic data show just the southern edge of a larger low-velocity anomaly in the backarc crust, which could be manifested by the joint inversion of active and passive seismic data recorded in the MERAMEX network (data sets (a) and (b)). The results of the joint inversion show an exceptionally strong low-velocity anomaly in the backarc crust northward of the active volcanoes which extends about 80 x 30 x 50 km in size within the crust and upper mantle of Central Java (Chapter 7). In the lower crust and upper mantle beneath the volcanoes, the low-velocity anomaly is inclined towards the slab, which probably reflects the paths of fluids and partially melted materials in the mantle wedge.

The body of anomalously low velocity identified in the tomographic study (2) could be interpreted as a zone of magma ascent by involving also petrochemical data. The results of the combined tomographic- petrochemical analysis are presented in Chapter 8 in form of a manuscript which was written mainly by Jane P. Chadwick (Dept. of Geology, University of Dublin, Trinity College) and me. Analyses of the physical characteristics of this body combined with chemical characteristics of lavas from adjacent volcanism indicate that molten magma comprises a significant percentage of this low-velocity anomaly. The study aimed in comprehensively identifying and describing a previously unknown, large-volume magmatic system and a prospective pre-cursor to a catastrophic caldera forming eruption: a so-called super-volcano. Super-volcanoes form from magma rising from deep within the Earth, often at subduction zones. Rather than breaching the surface in a standard eruption, it is thought that magma feeding a super-volcano pools and melts the adjacent crust, forming an immense underground reservoir of molten rock. Our knowledge of this stage of super-volcano development is poor, as the last super-eruption occurred at Toba caldera, Sumatra, Indonesia ~75,000 years ago. Other examples for super-volcanoes are the Yellowstone caldera in USA or the Taupo caldera in New Zealand. In Central Java, the most populous island in the world, prolonged volcanism has generated conditions suitable for the accumulation of such a large magma reservoir.

The tomographic studies were mainly performed with the code LOTOS-06 (Koulakov et al. 2006, 2007). Since this code is newly developed and still in a further developing stage, this study also includes a comparison study of code LOTOS-06 with the well tested three-dimensional travel time tomography code (3DTH) designed for seismic refraction surveys developed by J. Hole (1992) (Chapter 5). To verify the tomographic results of the two applied codes, vertical sections along several profiles are compared with each other and with the two-dimensional velocity-depth models of the wide angle seismic data (Chapter 4).

The following Chapter 2 provides a short overview about the tectonic setting, the seismicity distribution along the Sunda Arc with special emphasis on Java and the volcanism in Java. The MERapi AMphibious EXperiments (MERAMEX) and the acquired data are described in Chapter 3 in detail. The processing of the OBH/OBS and the streamer data was carried out on board of RV Sonne and at IFM-GEOMAR and is documented in the cruise report for leg SO 176 & SO179 (Kopp & Flueh 2004). Therefore, the processing of these data sets is not described herein.



## 2. THE SUNDA ARC

### 2.1 The Tectonic Setting

The Sunda Arc, which extends from the Bay of Bengal in the northwest, along Sumatra and Java eastwards to Flores, is the result of the northward orthogonal subduction of the Indo-Australian plate beneath the Eurasian plate (Hamilton 1979; Jarrard 1986) at rate of approximately  $6.7 \pm 0.7$  cm/yr (Tregoning et al. 1994) (Figure 2.1). This convergent plate boundary evolved after the collision of India with Eurasia in the Eocene and dominates the tectonic and volcanic processes of the Indonesian islands.

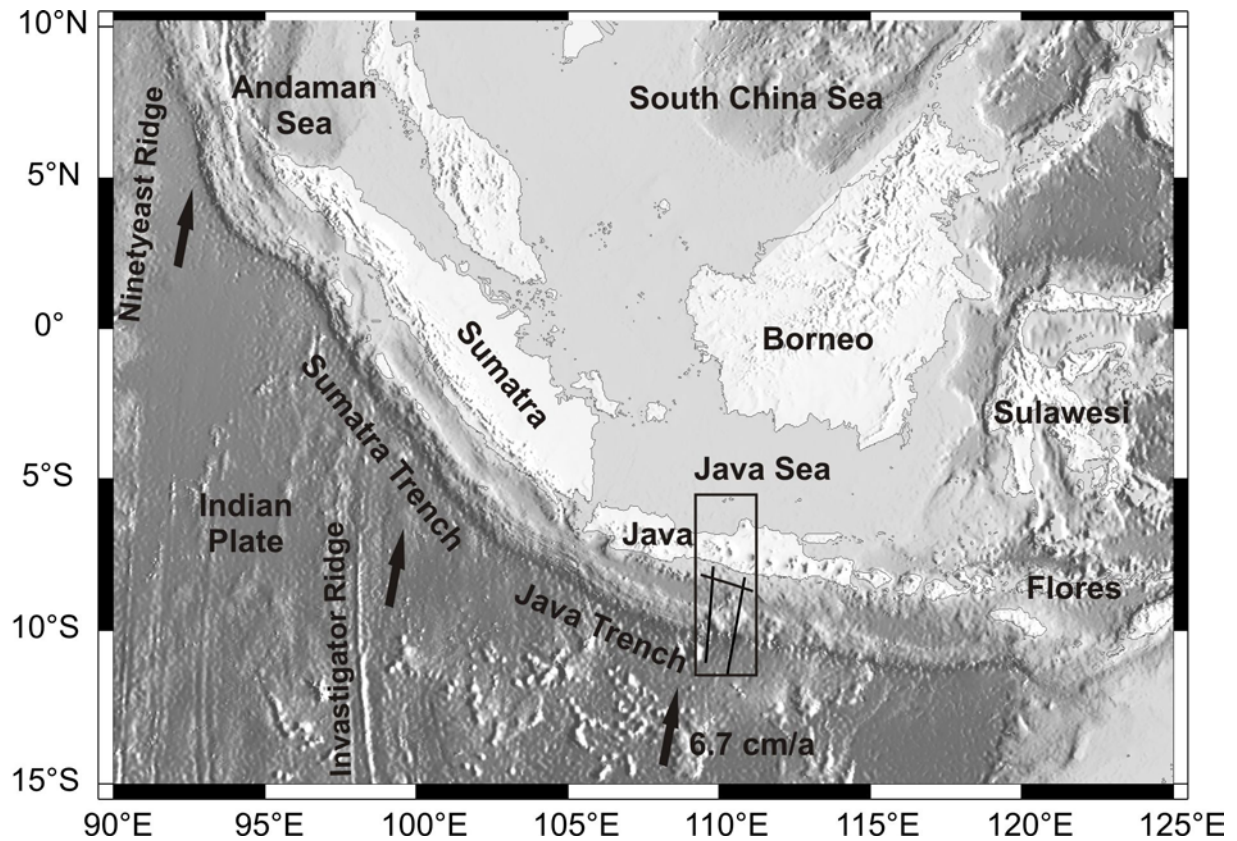


**Figure 2.1.** Bathymetric and topographic map of the Sunda Arc. The study area of the MERAMEX project is indicated by the rectangle and the three seismic profiles.

Along the Sunda Arc, the subduction obliquity changes from Sumatra to Java as a result of changes in the orientation of the plate margin. Along Sumatra the subduction is oblique whereas off Java the subduction direction is normal to the trench. The oblique subduction beneath Sumatra and further north results in partitioning of the convergent motion into thrust and strike-slip faulting. The age and thickness of the oceanic crust increases considerably from west to east: from 49 Ma to 96 Ma beneath Sumatra, from 96 Ma off western Java to 135 Ma off eastern Java and from 142 Ma to 161 Ma under Flores (Moore et al. 1980; Lasitha et al. 2006; Schöffel et al. 1999).

Accretionary Subduction zones are typically characterized by the incoming subducting oceanic plate, the trench, an accretionary prism, the forearc with a forearc basin and the volcanic arc on the overriding plate. Subduction zones are also classified into erosive convergent plate margins if the convergence rate exceeds  $6\pm 0.1$  cm/yr and the trench sedimentary cover is  $< 1$  km. If the convergence rate is less than 7.6 cm/yr and the trench sediment cover is  $> 1$  km, tectonic accretion is present (Clift & Vannucchi 2004). Not only the convergence rate and the sediment cover defines whether accretion or subduction erosion dominates, but important are also the thickness of the oceanic plate, the properties of the incoming sediments and the oceanic plate roughness, because these features define the amount of material necessary for accretion and subsequent growth of a prism. Tectonic accretion can be detected along the northwestern and western Sunda margin and off West Java, but along Central Java the subduction style changes to an erosive regime (Kopp et al. 2005). This change is based on the following facts:

- Only small amounts of sediments are transported into the trench off Java compared to the Sumatra region. The sediments in the system off Central Java are captured in the sedimentary basins.
- The roughness of the oceanic crust is relatively high (Masson 1991) due to a broad band of seamounts oriented in W- E direction. The Roo Rise, located south of Central Java, is approximately 2 - 2.5 km higher than the surrounding seafloor, irregular in shape, interacts with the trench and is largely responsible for the observed trench retreat to the north by approximately 50 – 60 km from a normal curvature of the trench between longitude 109°E and 115°E (Figure 2.1 & 2.2).
- The high convergence rate of  $\sim 6.7$  cm/a.

- There is no frontal accretionary prism developed along the Central Java margin which is proved by bathymetric data.
- The outer high is much higher than the one in the west at the Sumatra segment where the sediment influx on the incoming plate is greater than off Java (Kopp et al. 2002 & 2005). The outer high consists of several isolated bathymetric highs which could be caused by seamount subduction.
- Off Central Java, an active frontal accretionary prism, a continuous forearc high and a forearc basin are not developed (Figure 2.2).
- Wittwer et al (in prep.) identified a steep forearc slope angle of over  $6^\circ$  off Central Java whereas in western Java the slope angle is less steep ( $3^\circ$ ). The higher slope angle value off Central Java classifies the system as an erosive regime. The value off western Java is more typical for an accretionary system (Kopp et al. 2005).

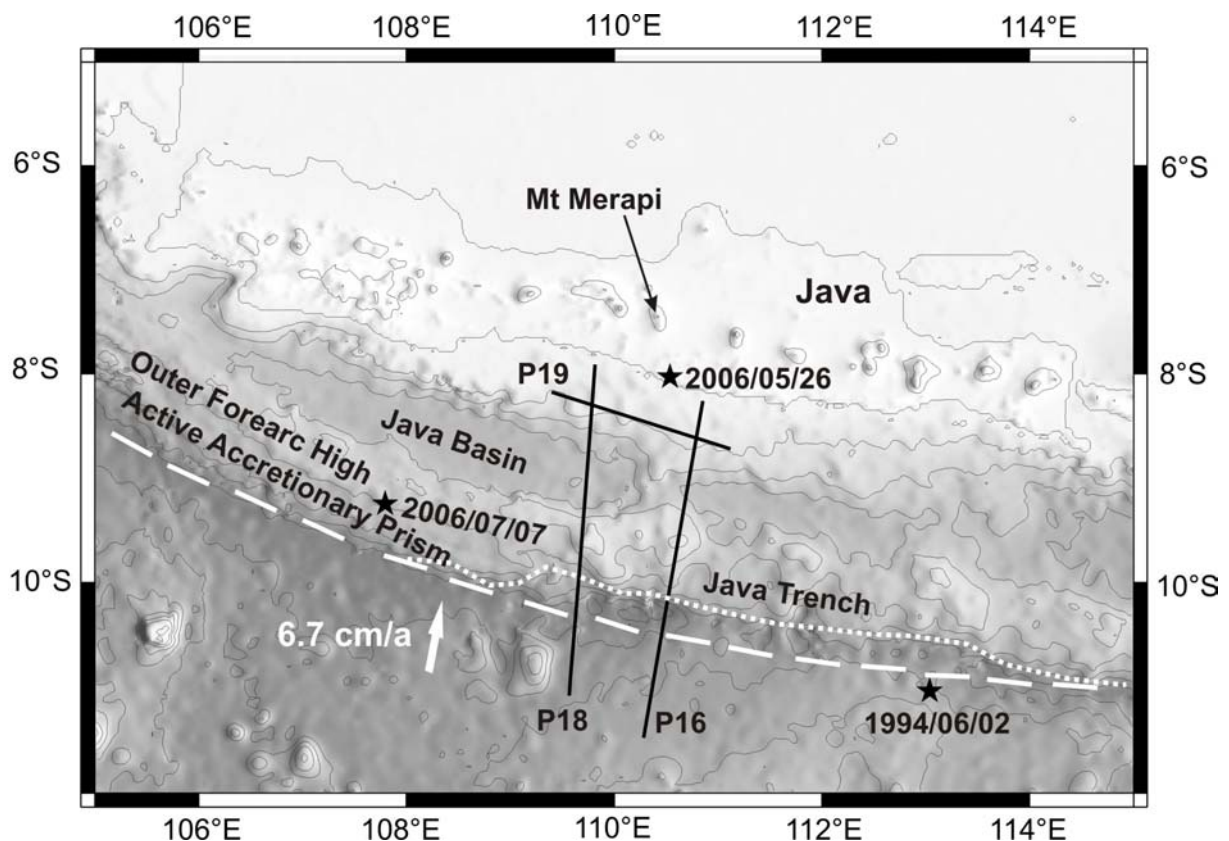


**Figure 2.2:** Topographic and bathymetric map of Java, Indonesia. The black lines mark the seismic profiles of the MERAMEX project. The Java trench, the active accretionary prism, the outer forearc high, the Java basin and Mt Merapi are indicated. The dotted line corresponds to the current track of the trench, which is retreating northward from the normal curvature trend (dashed line) in front of Central Java. The stars mark the three major earthquakes between 1994 and 2006.

## 2.2 Seismicity

The seismicity distribution along the Sunda Arc is not uniform (Figure 2.3). The depth of the Wadati-Benioff zone reaches from 200 km down to about 400 km depth beneath Sumatra. Deep seismicity does not exist beneath Sumatra, whereas deep events down to 670 km occur beneath Java and Flores. Deep seismicity accumulates north of Java around 111° E and 113° E, whereas the deep events in Central Java occur further north than the events to the east (Figure 2.3 & 2.4). The change of the hypocentral depth is explained by the increasing age of the subducting plate and the higher convergent rates compared to the Sumatra segment and further north (Kirby et al. 1996; Lasitha et al. 2006). The dip of the subduction zone also increases from west to east.

In general, seismic activity is higher regarding intensity and frequency along Sumatra than along Java. This might be due to a younger, and more shallowly dipping seafloor that enters the trench along Sumatra (Figure 2.2). Along the central part of the Java margin around 110° E seismic activity is highly reduced compared to the earthquake hypocenter accumulations to the west and east of this 100 km wide corridor. This led to the discussion of the so called ‘seismic gap’ of Central Java, which was one of the key elements within the study area of the MERAMEX project. The ‘seismic gap’ can clearly be detected in Figures 2.3 and 2.4.

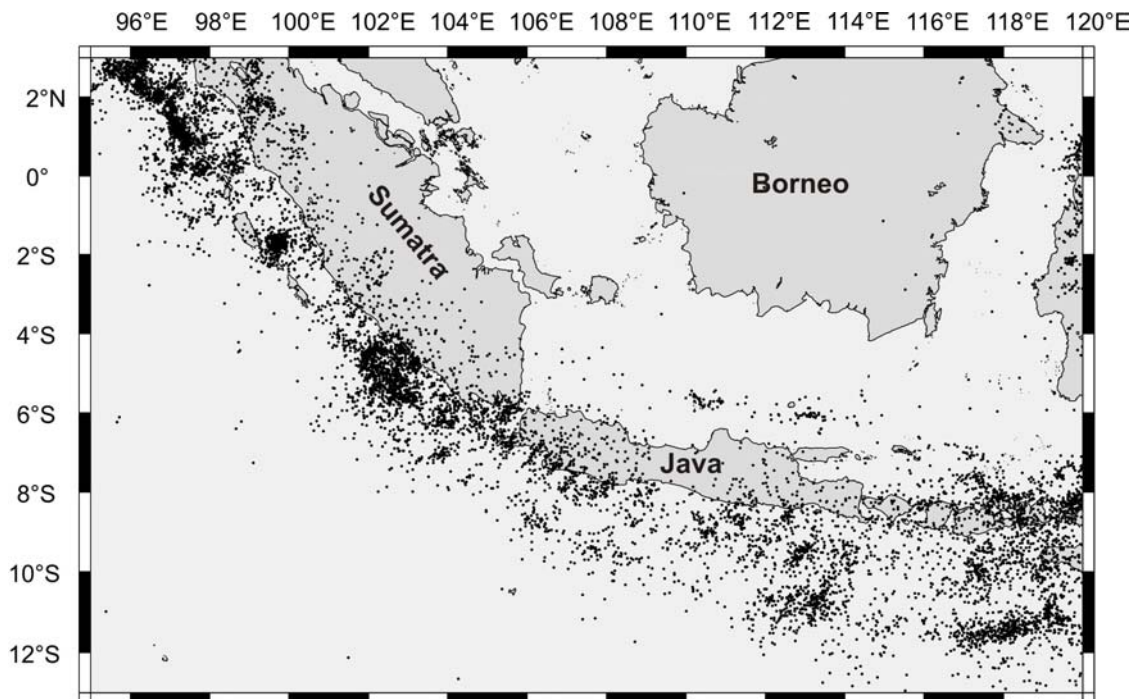


**Figure 2.3:** Epicenter distribution of earthquakes ( $M_w > 3$ ) recorded along the Sunda Arc between 1976 and 2007 (from Global CMT catalogue 2007).

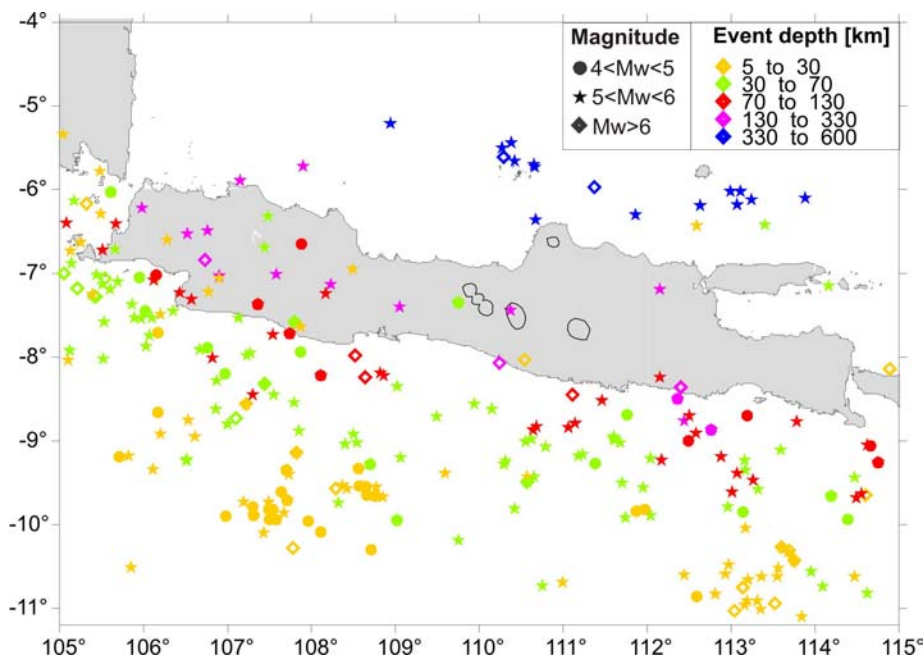


**Figure 2.4:** Event distribution along the Java margin (from Global CMT catalogue 2007). Different colours indicate the hypocenter depth and different symbols refer to the magnitude of the events.

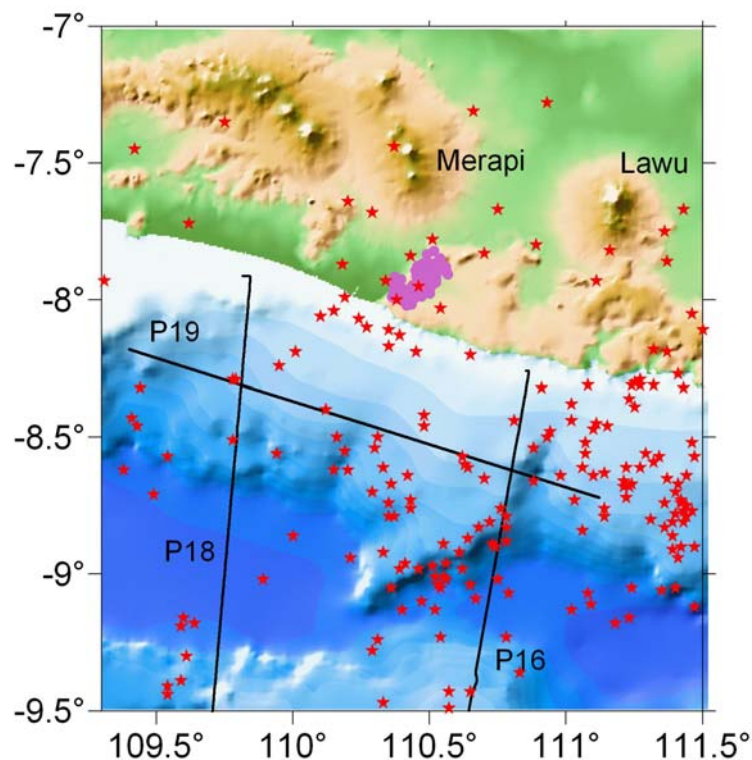


**Figure 2.5:** Topographic and bathymetric map of Central Java. The black lines mark the seismic profiles of the MEAMEX network. Merapi and Lawu volcano are indicated. The red stars mark events with magnitudes  $M_w > 3$  recorded between 1990 and 2007 (NEIC earthquake catalogue). The pink dots correspond to aftershocks of the May 26, 2006 earthquake recorded by the German Task Force.

Spicak et al. (2005) studied the seismotectonics in relation to the source region of volcanism along the Sunda Arc and also detected an aseismic intermediate-depth gap in the Wadati-Benioff zone in Central Java where earthquakes with magnitude  $m_b > 4$  in the depth range between 100 and 200 km do not exist or are highly reduced (Figure 2.4). No seismically active columns beneath the active volcanoes Guntur, Slamet, Merapi, Kelut and Raung in Central and East Java were observed whereas such columns exist beneath Gedeh volcano in west Java and beneath the volcanoes located further to the east. The existence of such an aseismic intermediate-depth gap in the Wadati-Benioff zone is interpreted as a partially melted portion of the slab which does not fulfil the necessary conditions to generate strong earthquakes.

Events listed in the NEIC catalogue between 1990 and 2007 and the aftershocks of the May 26, 2006 Java event are plotted on top of a topographic map in Figure 2.5. North of the volcanoes Merapi and Lawu only few events were recorded within the last years (see also Figure 2.3 & 2.4). The aftershocks of the May 26, 2006 event accumulate in the Gunung Kidul Mountains in the south west of Merapi volcano. Some events seem to line up in NNE-SSW direction forming a line reaching from the aftershock cluster in south west direction to the intersection of the marine seismic profiles P18 and P19. Along the bathymetric structure interrupting the Java basin between  $110.3^\circ$  E and  $111^\circ$  E, several events accumulate and line up along this structure further north east up to the coast line of Central Java. Spicak et al. (2007) related the seismicity pattern at the Java margin to the morphology of the seafloor because the along-trench seismicity correlates with the position of the Java trench and the onset of the Wadati-Benioff zone correlates with the Java basin.

### 2.3 Volcanism Along the Sunda Arc

The subducting oceanic plate releases fluids, which ascend from a depth of approximately 100 km and cause partial melting (e.g. Peacock 1990; Ruepke et al. 2002). Fluids and melts ascend to form the volcanic arc, which consists of more than 100 active volcanoes in Indonesia including the largest Quaternary caldera on Earth, Toba caldera, in northern Sumatra (Bindeman 2006) and the most active volcano in Java, Merapi volcano.

Since van Bemmelen (1949) Java has been divided into four zones running parallel to the length of the island (Figure 2.6) (Smyth et al. 2005). The active arc in Central and East Java is bound to the south by the Southern Mountains Zone, eroded remnants of the Middle Eocene to Early Miocene (from 42 to 18 Ma) volcanic arc which is built on Mesozoic basement (Figure 2.6). Prior to the Middle Eocene no evidence for active subduction south of Java along the Java trench was detected. Between 18 and 12 Ma volcanic activity was strongly reduced and resumed during the Late Miocene volcanism further north at the position of the present day volcanic arc approximately along the center of the island. The present-day volcanic arc is built on parts of the Kendeng zone, the main Cenozoic depocentre for the region which contains thick sequences of volcanogenic and pelagic sediments. The Kendeng Zone is a basin that is thought to contain between 8 km (de Genevraye & Samuel 1972) and 11 km (Untung & Sato 1978) of sediment. This sediment overlies a basement of uncertain composition that has been referred to as quasi-continental, immature arc crust, which extends approximately 25 km below the surface (Curry et al. 1977; Jarrard 1986; Van Bemmelen 1949). The Kendeng zone is an east-west trending fold and thrust belt (Smith et al. 2003 & 2005) and is prominent for its strong negative Bouguer gravity anomaly (Figure 2.7) which indicates the deep basement. To the north of the Kendeng zone is the Rembang zone located representing the edge of the Sunda shelf. This zone consists of Eocene to Pliocene shelf deposits i.e. mainly marine clastic sediments and carbonates (Smyth et al. 2003 & 2005).

The most active volcano of the present-day volcanic arc in Central Java is Mt. Merapi. Recent volcanic activity at Merapi volcano has been largely restricted to extrusion of viscous crystal- and inclusion-rich dome-forming lavas (Gertisser & Keller 2003). It is assumed that these lavas had only minimal interaction with the Java crust (Gertisser & Keller 2003). However, the numerous inclusions of both igneous and sedimentary origin hosted in recent deposits suggest the operation of complex and numerous crustal magmatic processes (see Chapter 7).

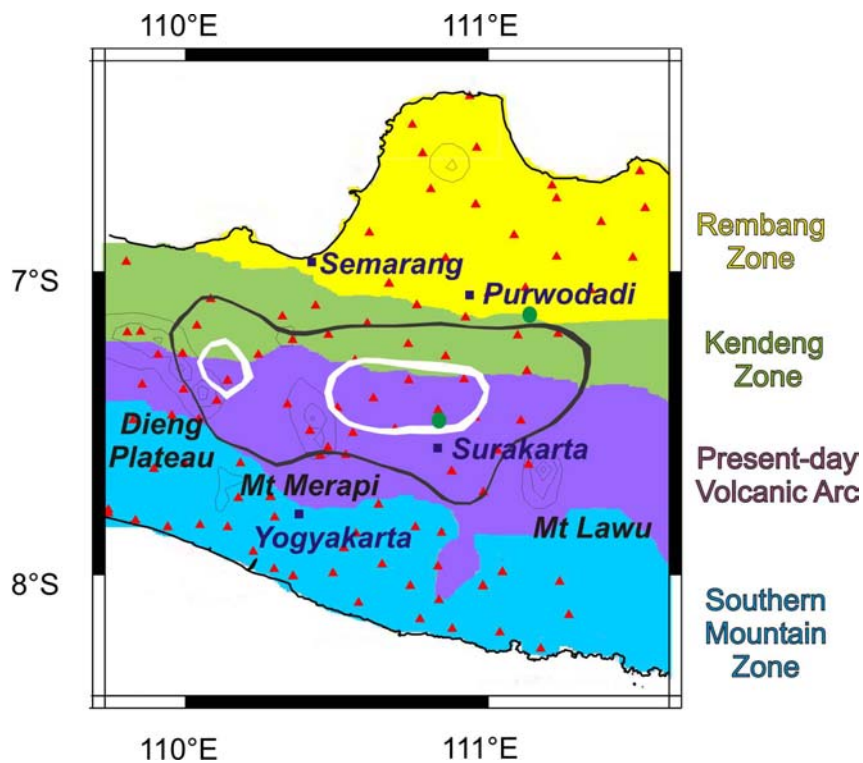


**Figure 2.6:** Map of Central Java showing the stratigraphic and structural zones (after Van Bemmelen 1949). The red triangles mark the receiver distribution of the MERAMEX network and the green dots the locations of well known mud volcanoes. The black surrounded area represents the size of the detected low-velocity anomaly with maximum amplitudes of  $-10\%$  and the white framed areas the size of the low-velocity anomaly with maximum amplitudes of over  $-20\%$  in 10 km depth (see Chapter 7 for details).

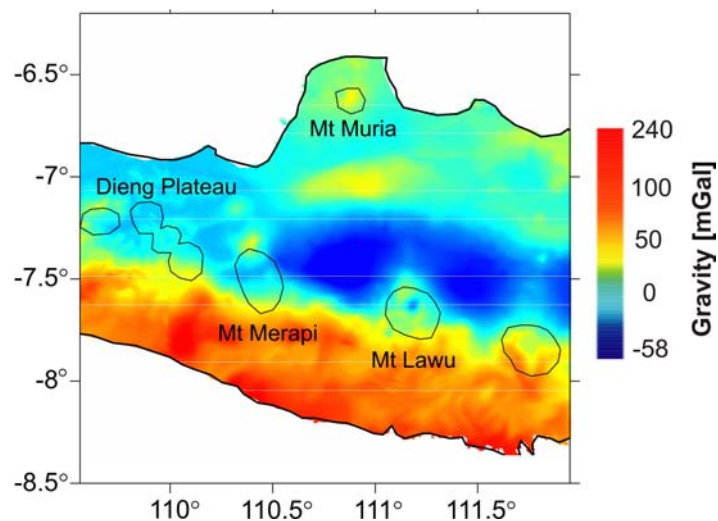


**Figure 2.7:** Bouguer gravity anomaly map after Smith et al. (2005). The gravity low corresponds to the Kendeng basin, which extends about 400 km in east-west and 100-120 km in north-south direction and contains more than eight kilometers of sediments.

Previous geophysical studies in Central Java have typically focused on the internal structure of Merapi volcano (Müller & Haak 2004; Müller et al. 2002; Wegler & Lühr 2001) with the deeper structure remaining poorly understood. An aseismic zone at a depth of approximately 2.5 to 3 km below Merapi's summit has been reported and may indicate the existence of a shallow melt pocket, fed from a deeper reservoir below 5 km depth (Ratdomopurbo & Poupinet 2000). This is in agreement with petrological results (Gertisser & Keller 2003). Deeper storage chambers were postulated on the basis of geobarometry (Gertisser 2001), GPS and tilt data (Beauducel & Cornet 1999; Westerhaus et al. 1998) and seismic data (Wasserman et al. 1998).



### 3. THE MERAMEX DATA SET

The MERapi AMphibious EXperiments (MERAMEX) were conducted in 2004 in order to study the tectonic structure of Central Java, and to gain a better understanding of the linkage between subduction and arc volcanism. In May 2004, a temporary seismological network was installed in a dense grid of about 10-20 km station spacing around Merapi volcano in Central Java to monitor the natural seismic activity. The network consisted of 106 continuously recording short-period three-component seismometers (Mark L4-3D) in combination with Earth data loggers (EDL) and 14 broadband stations operated with Guralp seismometers (CMG3T and CMG3ESP) and SAM data loggers. The sampling rate of the data loggers was 100 Hz. Two of the short-period seismometers were installed 60 km north of the main network on the Karimunjawa islands in the Java Sea. Nine Ocean Bottom Hydrophones (OBH) and five Ocean Bottom Seismometers (OBS) extended the land network offshore, south of Central Java (Figure 3.1 & 3.2). The offshore stations were in operation for a period of 18 weeks while the onshore network operated for 21 weeks.

The recorded local events resulted in a huge data set. Up to now, about 500 events were picked and relocalized in the local earthquake tomographic studies performed by I. Koulakov (2007). The events mainly occurred in a strip between the volcanic arc in the north and the trench in the south. North of the volcanic arc only few events were detected. Two stations were installed on the Karimunjawa islands north of Central Java because deep events around 600 km depth were expected. Unfortunately, the deepest earthquakes detected in the MERAMEX network up to now occurred in a depth of about 320 km. The vertical section in Figure 3.2 presents a projection of the events on top of the profile marked in the horizontal map above. The events clearly image the shape of the subducting oceanic plate beneath Central Java. Along the Benioff zone the events line up in a 30-40 km thick layer. Between 40 and 130 km depth, a double seismic zone with a dipping angle of about 45° and a thickness of 20-30 km is visible (Koulakov et al. 2007). The thickness of the double seismic zone seems to decrease with increasing depth. The dipping angle of the subducting oceanic plate is about 10° in the upper 40 km and about 45° between 40 and 200 km depth. The dipping angle of 10° in the upper crust could also be manifested by the forward models of the OBH data (see Chapter 4). The local earthquake data set used in Chapter 7 includes 8000 P- and 5800 S-phases from 292 local events.

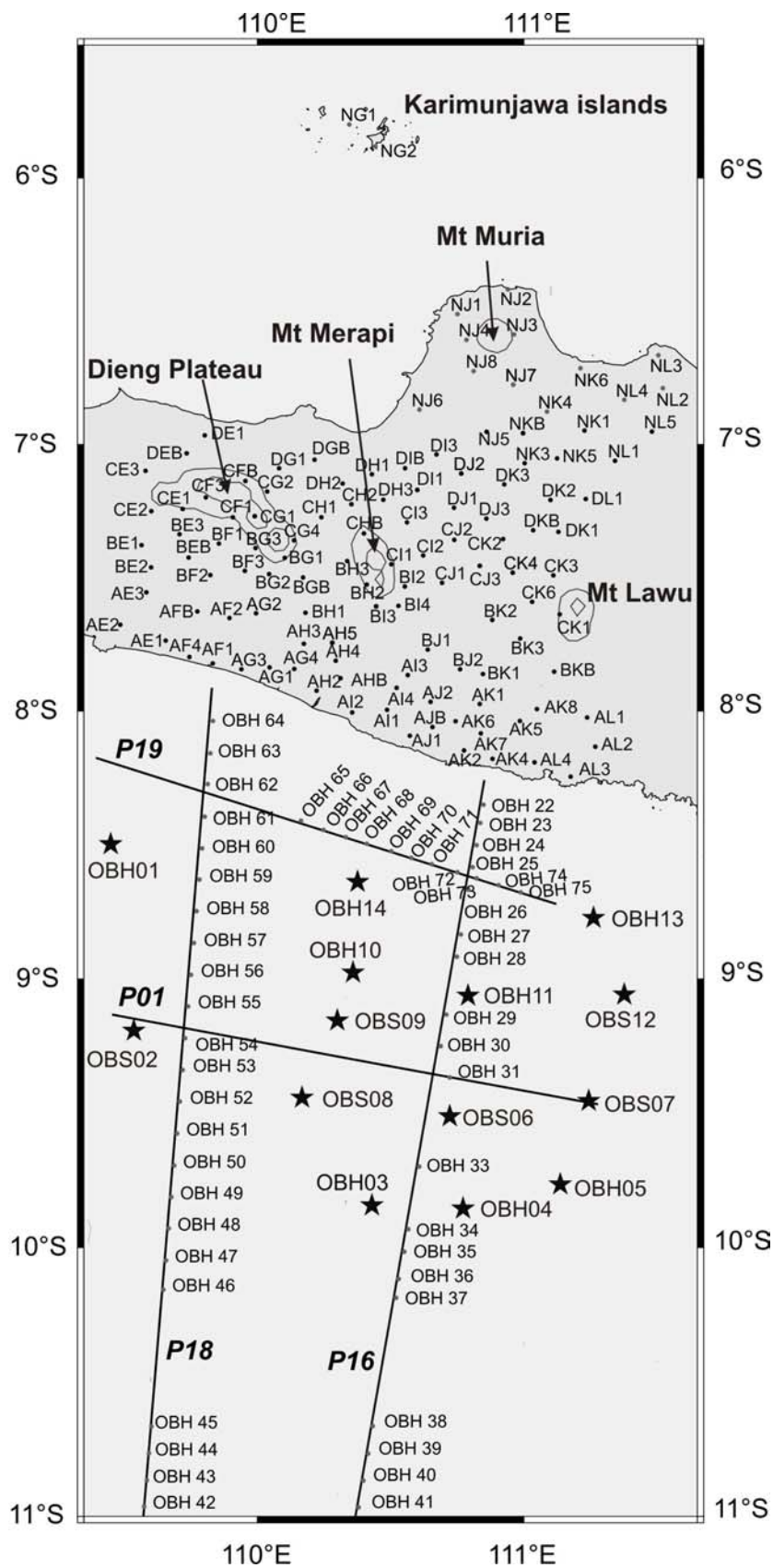


**Figure 3.1:** The MERAEMX project: the seismological network consists of onshore receivers (dots onshore Central Java and on the Karimunjawa islands) and of OBH and OBS stations marked by stars. Along the wide-angle seismic profiles, OBH stations were deployed.

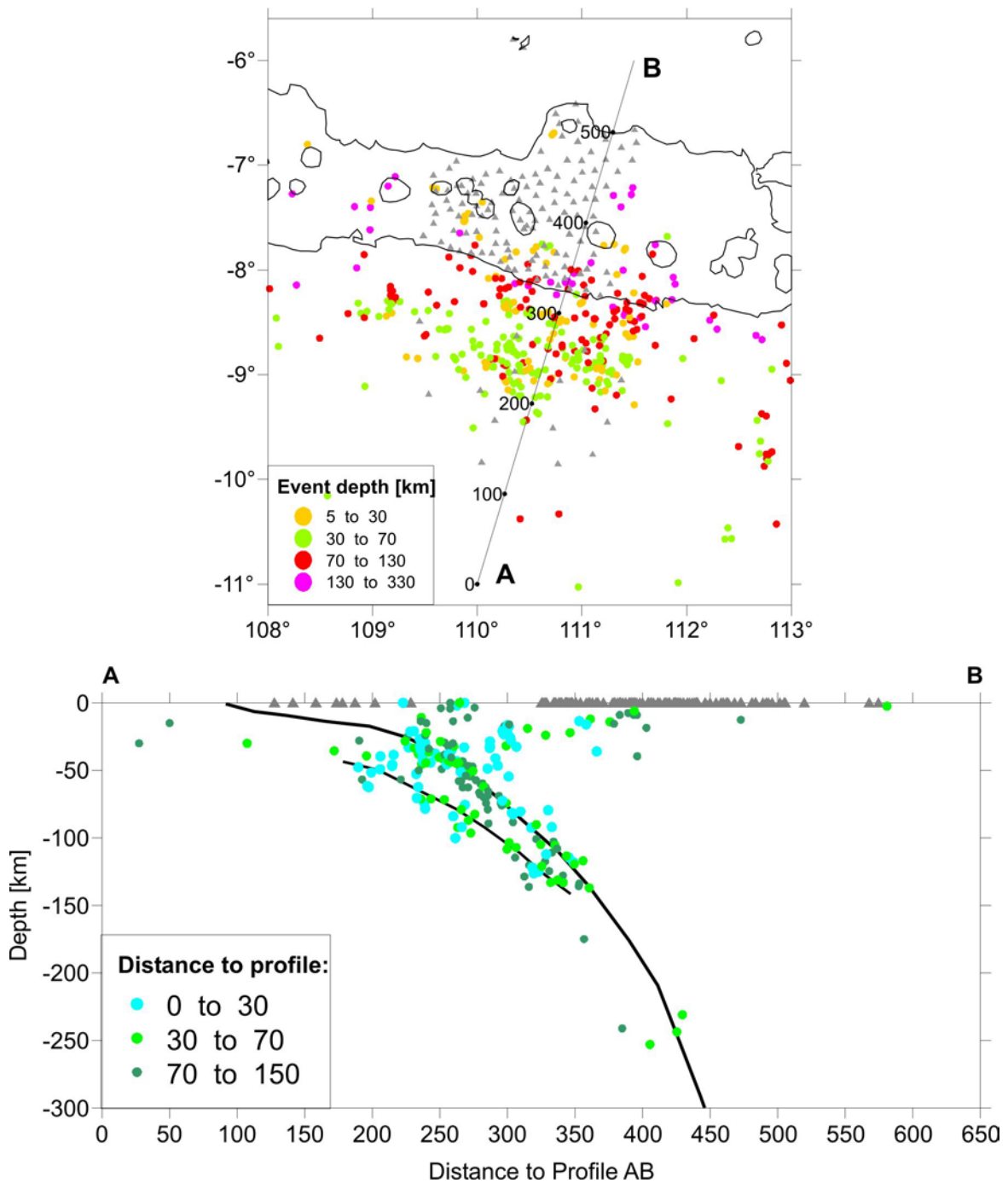


**Figure 3.2:** Map view (upper image) and cross section (lower image) along profile AB showing the earthquake distribution of the events recorded within the MERAMEX network. Different colours indicate the event depths. The receivers are marked by grey triangles. The black lines show the supposed shape of the slab and the double seismic zone. These lines are based on the event distribution of the MERAMEX catalogue for the upper 250 km depth. For deeper depth sections, deep events of the ISC catalogue (2001) were used to determine the shape of the slab.

In September/October 2004 RV Sonne set out to acquire seismic refraction and reflection profiles including mini-streamer, bathymetric, gravimetric and magnetic data. Two of the seismic profiles, the two dip lines P16 and P18, are oriented perpendicular to the plate boundary and reach from close to the southern coast, across the trench, up to the oceanic plate (Figure 3.1). The third profile P19 is oriented parallel to the coast and crosses the two other profiles. The main objective of the profiles was to reveal the tectonic setting of the subduction zone on- and offshore Central Java. The seismic profiles were shot with an array of three 32-l (2000 inch<sup>3</sup>) BOLT airguns (Model 800 CT Bolt), towed 60 m behind the vessel at a depth of 7 - 8 m. The airgun array operated at 145 bar, at a shot interval of 60 s and at a speed of approximately 4.9 knots. The airgun shots generated signals with a main frequency centred around 6 to 8 Hz including higher harmonics. The seismic signals emitted from the marine airgun source array were recorded offshore on 75 OBH (Ocean Bottom Hydrophone) stations deployed along the seismic profiles and onshore within the temporary seismological network (Figure 3.3). Simultaneously to the acquisition of the refraction data, a four- channel mini-streamer was in operation. The streamer consisted of four 12.5 m long active sections with 25 hydrophones spaced at 0.5 m. The lead-in cable was 150 m long and the streamer wig was placed midships about 8 m away from the aft of the vessel.

The land receivers stored the raw data of the airgun profiles P16, P18 and P19 in MiniSEED data format, which subsequently was converted to SEG-Y and sorted to receiver gathers. Spectral analyses of each receiver gather helped to determine the ideal filter section. The first arrival travel times were picked after applying a bandpass butterworth filter with filter corners of 3-12 Hz, a notch filter dependent on the individual receiver gather to eliminate spikes and a linear moveout (reducing velocity) of 6 km/s to the raw data. All traces were individually normalized. Picking was facilitated by the small trace spacing of about 150 m, which provided excellent correlation between traces. A principal difficulty was the correct identification of first arrivals across an entire section. Figure 3.3c shows a seismic section of station AH3, located in the south west of Mt. Merapi (see Figure 3.1 for exact position). The section shows the receiver gather of the airgun shots of the coast parallel profile P19. The picking accuracy of the first arrivals was high, typically about 100 ms. Maximum offsets of about 150 km between shots and onshore receivers were common. Further seismic sections of onshore receiver stations are presented in Appendix A.

Due to the good data quality, the receiver gathers of all available D and N stations were produced and processed. Unfortunately, the air gun signals of profile P16, P18 and P19 couldn't be identified on these stations. In addition, another coast parallel profile P01 was performed south of profile P19 (Figure 3.1). However, along this profile an airgun array consisting of at most two 32 l airguns was used to generate the signals, resulting in any recorded signals at the land receivers. Anyway, not only the weaker signal but also the large offsets were the reason that no signals emitted along profile P01 were recorded onshore.

Therefore, the three-dimensional active seismic data consist of the shot data of profile P16, P18 and P19 recorded within the onshore array. Airgun signals of profile P16 could be picked at 26, of profile P18 at 28 and of profile P19 at 32 land receivers, resulting in 50060 first break travel time observations onshore (see also Table C4, Appendix C). These receivers cover southern Central Java up to the volcanic arc (see Chapter 4).

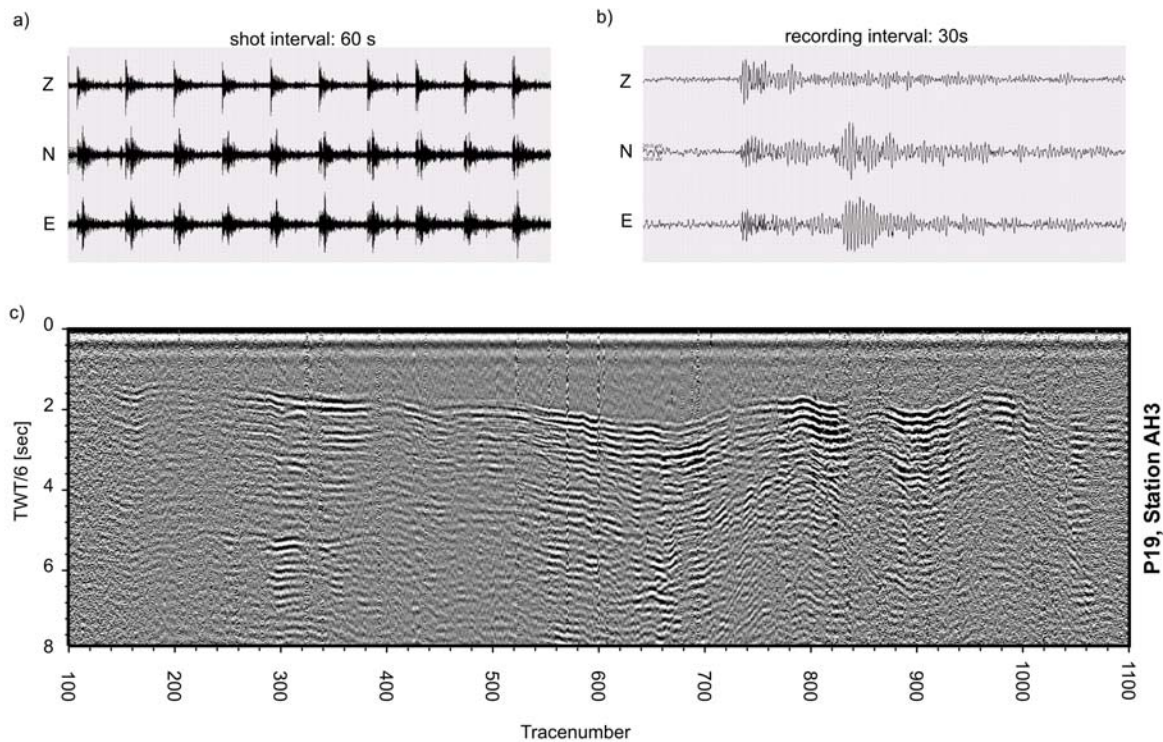


**Figure 3.3:** a) Z, N and E components of airgun signals having a shot interval of 60 s recorded onshore. b) Zoomed-in seismogram of one single airgun shot. The shown recording interval is 30 s. c) Example of a seismic section of an onshore station (AH3) located southwest of Merapi volcano in Central Java. It shows the good data quality of the airgun profile P19 recorded onshore. The first onset of each trace of the coast-parallel profile can be picked at this onshore station.



## 4. CRUSTAL STRUCTURE SOUTH OF CENTRAL JAVA

### 4.1 Forward Modeling of OBH Data

The seismic reflection and refraction data acquired along the wide-angle profiles P16, P18 and P19 during RV Sonne cruise SO179 were modeled using the MacRay software (Luetgert 1992) to obtain a velocity-depth model of the subduction zone offshore Central Java. MacRay is a two-dimensional seismic ray-tracer for Macintosh. The theoretical rays and their corresponding travel times are calculated from a laterally heterogeneous model and are subsequently compared to the acquired wide-angle-data. The model is defined using P- and S-velocities as well as densities. The first break travel times, reflection and later refraction arrivals were identified and picked on all seismic OBH/S-sections. Initially, the bathymetric data was loaded and then each layer was modeled by adapting the velocity gradient and the layer thickness. The model was built from top (the upper sedimentary layer) to bottom iteratively and updated until calculated and measured travel times correspond. The model quality depends on the picking accuracy of the phases. The first arrivals in the near offset have uncertainties of less than  $\pm 50$  ms; at greater offsets the uncertainties are approximately  $\pm 100$  ms.

Profile 19 is located approximately 200 km landward of the deformation front on the shelf area and approximately 50 km off the south coast of Central Java (Figure 3.2). The seismic reflection data recorded along this profile (Figure 4.1) were included in the forward modeling process of the OBH data. The structures detectable in the streamer section exhibit some topographic undulations, with troughs formed by river deposits located at profile km 15 and 175 (trace number 50 and 1100). A basement high is located at the intersection of profile P18 and P19. Adjacent to this structure between profile km 60 and 70 (trace number 350 to 450), a land slide can be recognized. Several faults are detectable further east. In total, eleven OBH stations were deployed between profile km 90 and 190 (Figure 4.1). Ten of the eleven stations could be forward modeled (OBH stations 65-70 and 72-75). Due to the coast parallel location of this profile, the travel time pattern along this profile is not very complex. Nevertheless, the modeling of this profile was complicated because the OBH stations were only deployed along the eastern part of the profile resulting in a large gap of recording instruments on the western profile segment. Unfortunately, the interesting structure, the basement high, is located in the western segment of the profile along which no OBH stations were deployed. Therefore, the

rays with large offsets detected at OBH stations 65, 66, 67 and 68 (Figure 4.2 and Appendix B) located close to this structure were used to verify the layer thickness and velocity gradients of the upper layers in this region. Since the data quality of OBH station 73 and 74 (Figure 4.3 and Appendix B) was very good, yielding in refraction phases along the complete profile length of 200 km, these phases could be used to adapt the layer thickness and velocity pattern of the deeper structures along the western profile segment.

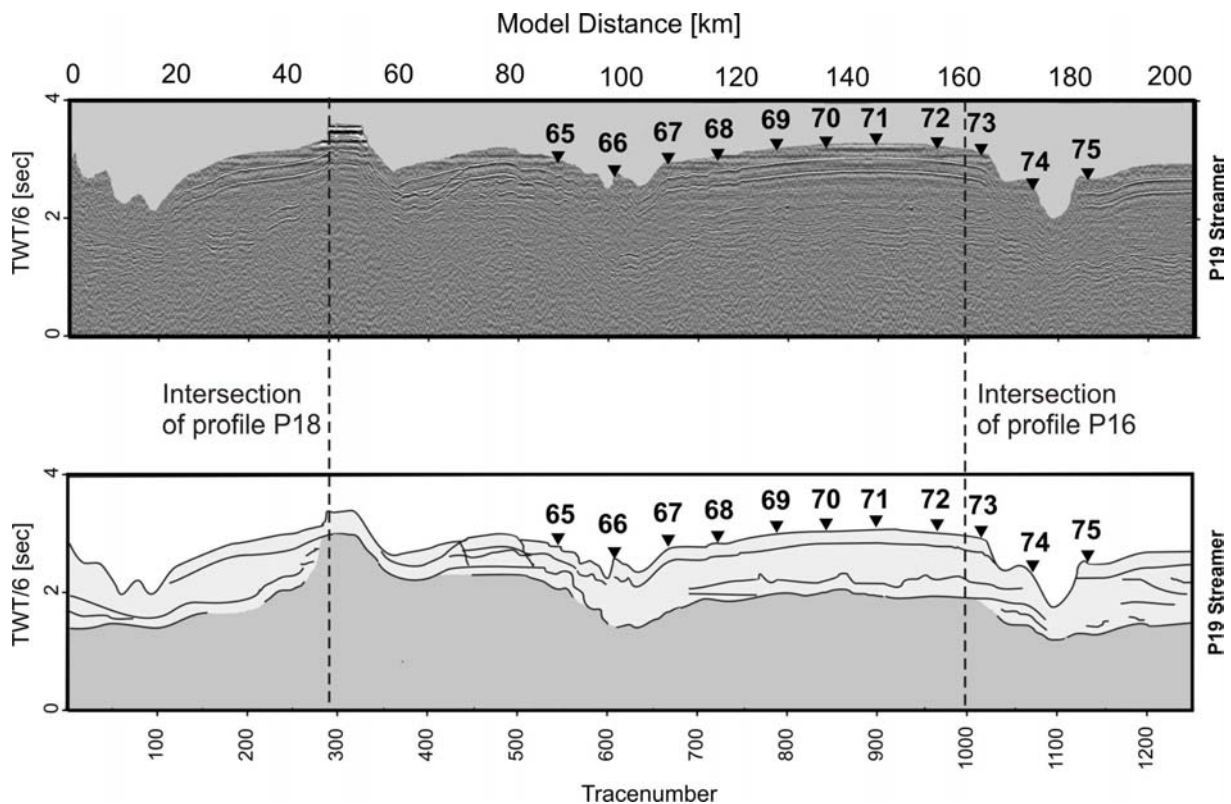


**Figure 4.1:** Record section from streamer profile P19 water migrated (top) and detected layers and faults (bottom). The triangles and the corresponding numbers indicate the position of the OBH stations deployed along profile P19. The dashed lines mark the intersection of the dip lines P16 and P18 with profile P19.

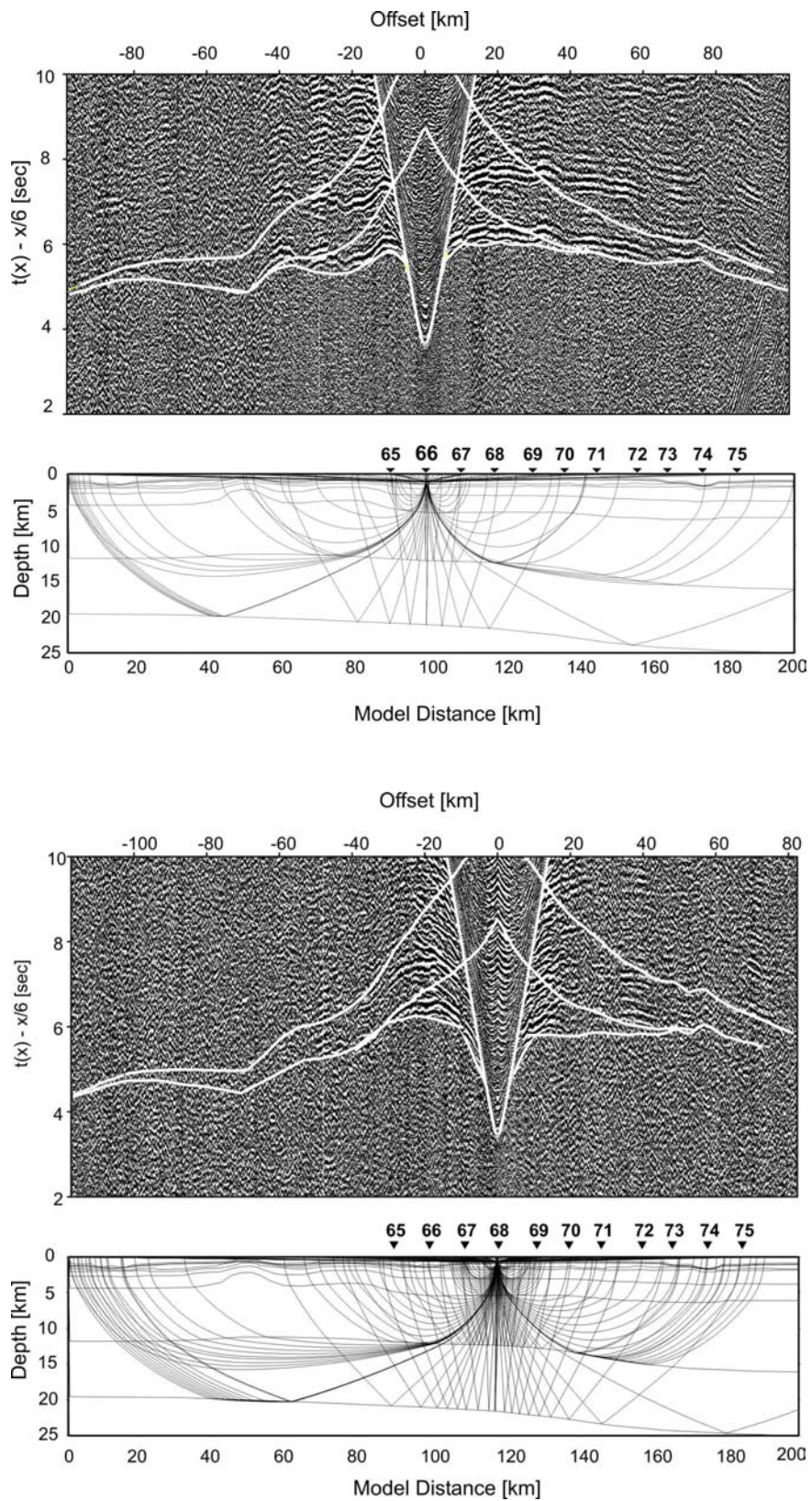


**Figure 4.2:** OBH 66 (the upper two diagrams) and OBH 68 (the lower two diagrams) are located in the center of the coast parallel profile P19. The diagrams show the processed data and the model with the modeled ray paths respectively.

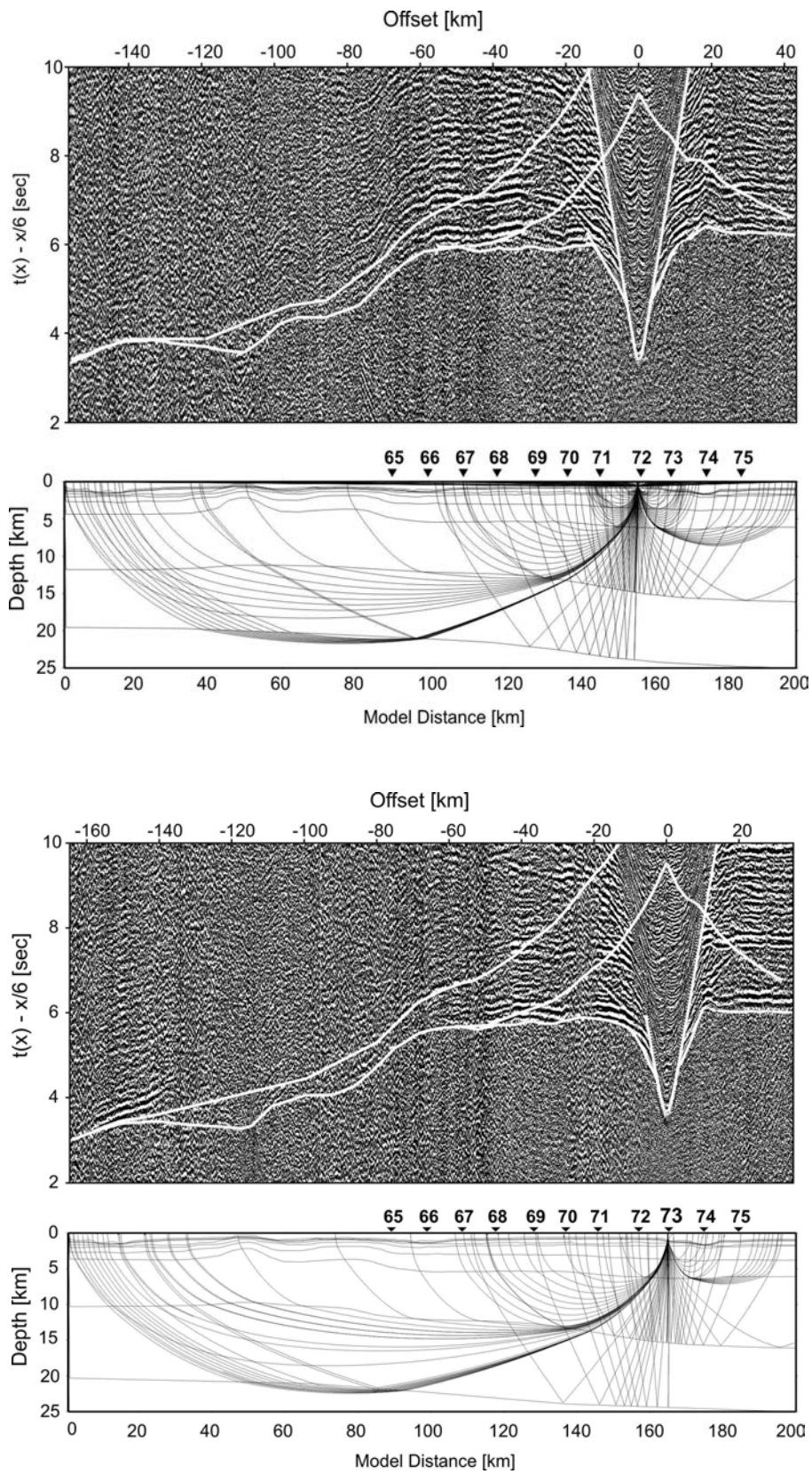


**Figure 4.3:** OBH 72 and OBH 73 are located in the eastern part of profile P19. The diagrams show the processed data and the model with the modeled ray paths respectively.

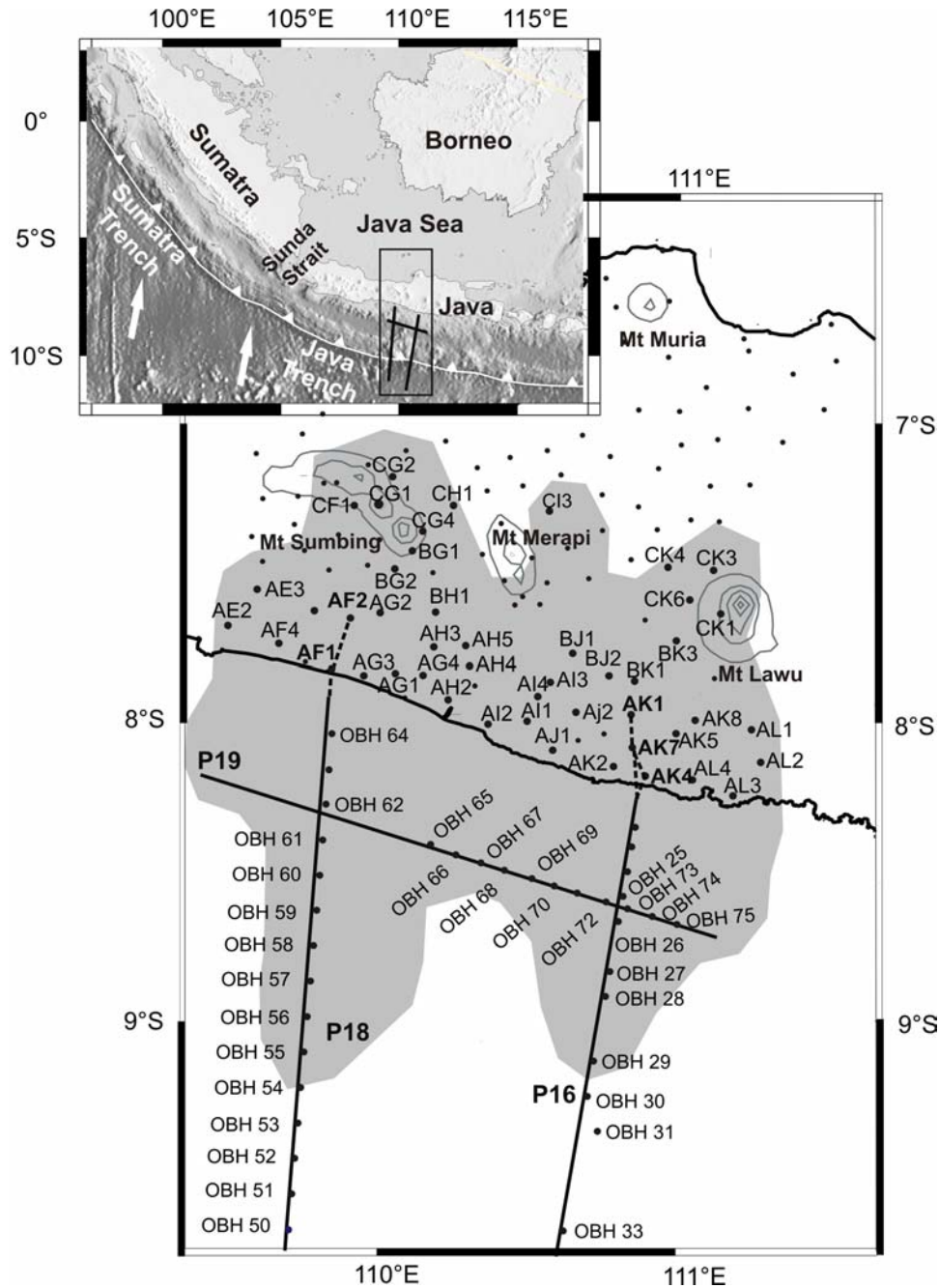


**Figure 4.4:** Map of the study area. The dots located in Central Java mark the receiver distribution of the temporary seismological network. The stations plotted with receiver names are the ones having recorded airgun signals of at least one of the three seismic profiles P16, P18 and P19. The shaded area marks the area of high resolution of the active seismic data (checkerboard tests). The black lines represent the airgun profiles, whereas the dashed section corresponds to the elongation of the profiles onshore Central Java. The dots along the profiles show the OBH (ocean bottom hydrophone) locations. OBH stations with station names were used in the forward modeling process.

The final forward model of profile P19 shows a mainly flat layering except for the basement high, a 30 km long section located at the intersection of profile P19 with the western profile P18 (Figures 4.4 and 4.5). The basement high at profile-km 50 could be clearly resolved with 0.6 km/s higher velocities compared to the surrounding area. The crustal thickness of the upper plate, as indicated by the low upper crustal velocities, increases from west to east. The Moho along this profile, however, could not be resolved as no mantle phases were observed. This profile was then used to constrain the structural geometry in three dimensions between the two dip lines P16 and P18.

The 20 OBH/S stations deployed along profile P16 and the 23 OBH/S stations deployed along profile P18 were picked and forward modeled by A. Wittwer (IFM-GEOMAR). The airgun shots released along the three profiles P16, P18 and P19 were also recorded within the onshore MEARMEX network. This enabled to elongate the two-dimensional forward models of profile P16 and P18 onshore Central Java using onshore seismometer stations (Figure 4.4). The onshore receivers recorded not only refracted but also direct waves with seismic velocities of 4.7-4.8 km/s. To elongate profile P18 onshore Central Java, the land receivers called AF1 and AF2 were used (Figure 4.4). Station AF1 had an offset of 10.3 km and station AF2 an offset of 30.2 km to the northernmost airgun shot of profile P18. The additional travel time information helped to model the basement high at the cross point of profile P18 and P19 and significantly improved the adaptation of modeled and measured rays at the OBH stations close to the coast, especially OBH stations 60-64. Hence, the thickness of the layers up to a depth of 10 km decreases north of OBH64 (Figure 4.6). This decrease could only be manifested due to the joint modeling of OBH and land data.

To elongate the eastern profile P16 three stations were used: station AK1 had an offset of 31.6 km, station AK7 19.3 km and station AK4 9.3 km to the northernmost shot point (Figure 4.4). However, the additional information affected the final result (Figure 4.6) only in the northernmost ten profile km. The layer thickness also decreases along profile P16 in the onshore section, but not as strong as along profile P18.

The final models of the two dip lines P16 and P18 and of profile P19 were merged together to constrain the velocity distribution and the layer thickness at the cross points of the profiles. At the intersections of the coast parallel profile P19 with the western and eastern profile, the crustal models (Figure 4.7) tie in reasonably well.

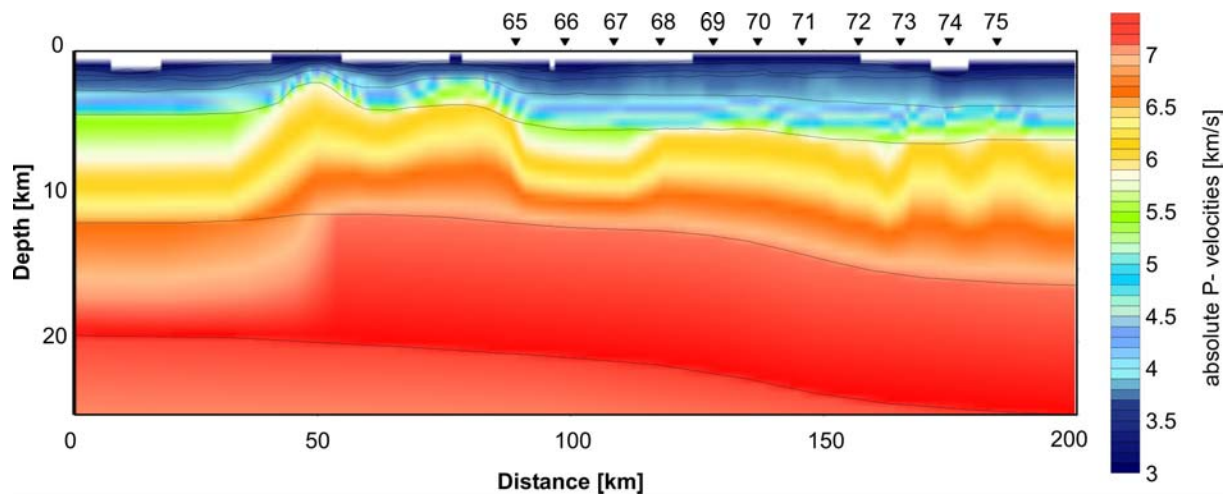


**Figure 4.5:** Forward model of profile P19 showing absolute P-velocities. The OBH locations are marked by the black triangles.

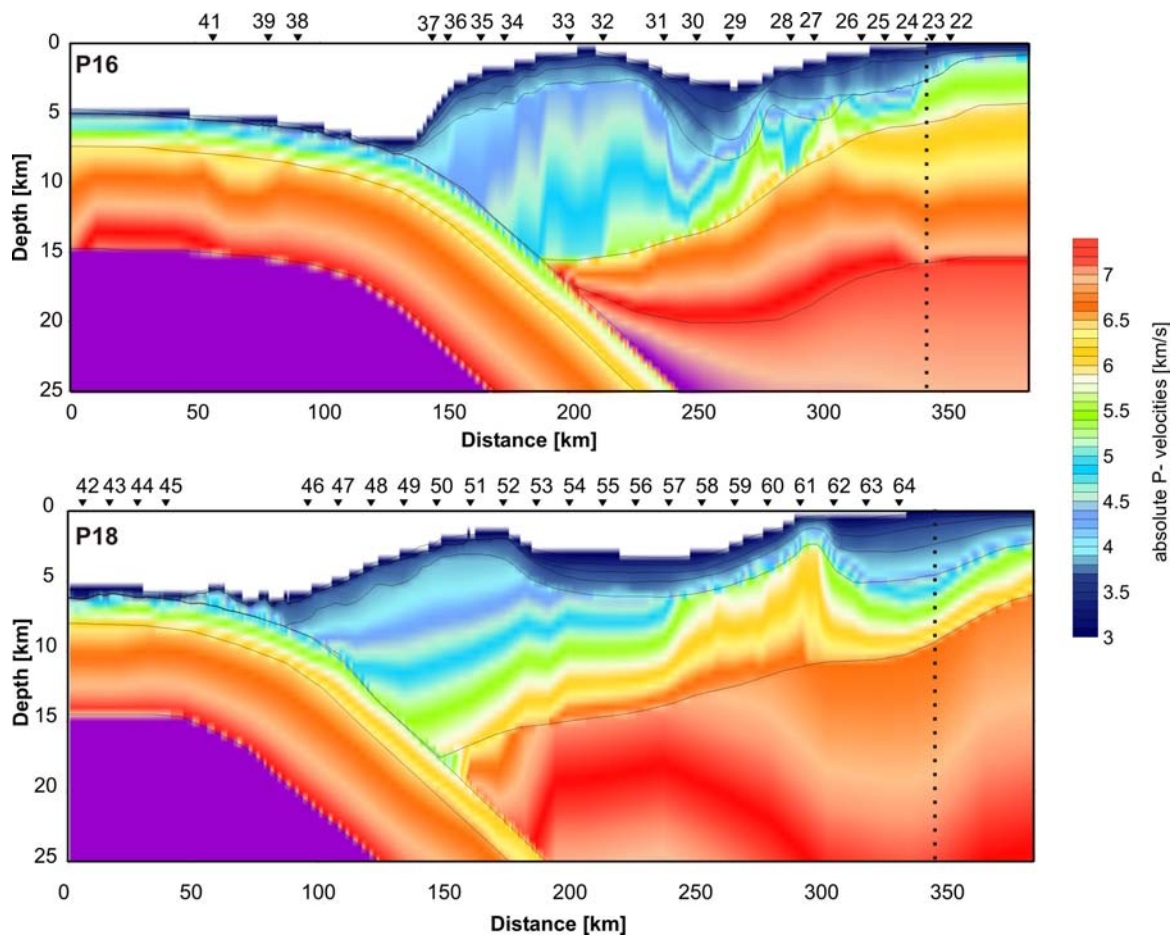


**Figure 4.6:** Forward model of profile P16 (upper diagram) and P18 (lower diagram) showing absolute P-velocities. The OBH locations are marked by the black triangles on top. The dotted lines indicate the northern end of the model if no land receivers are used for an elongation of the profile onshore Java.

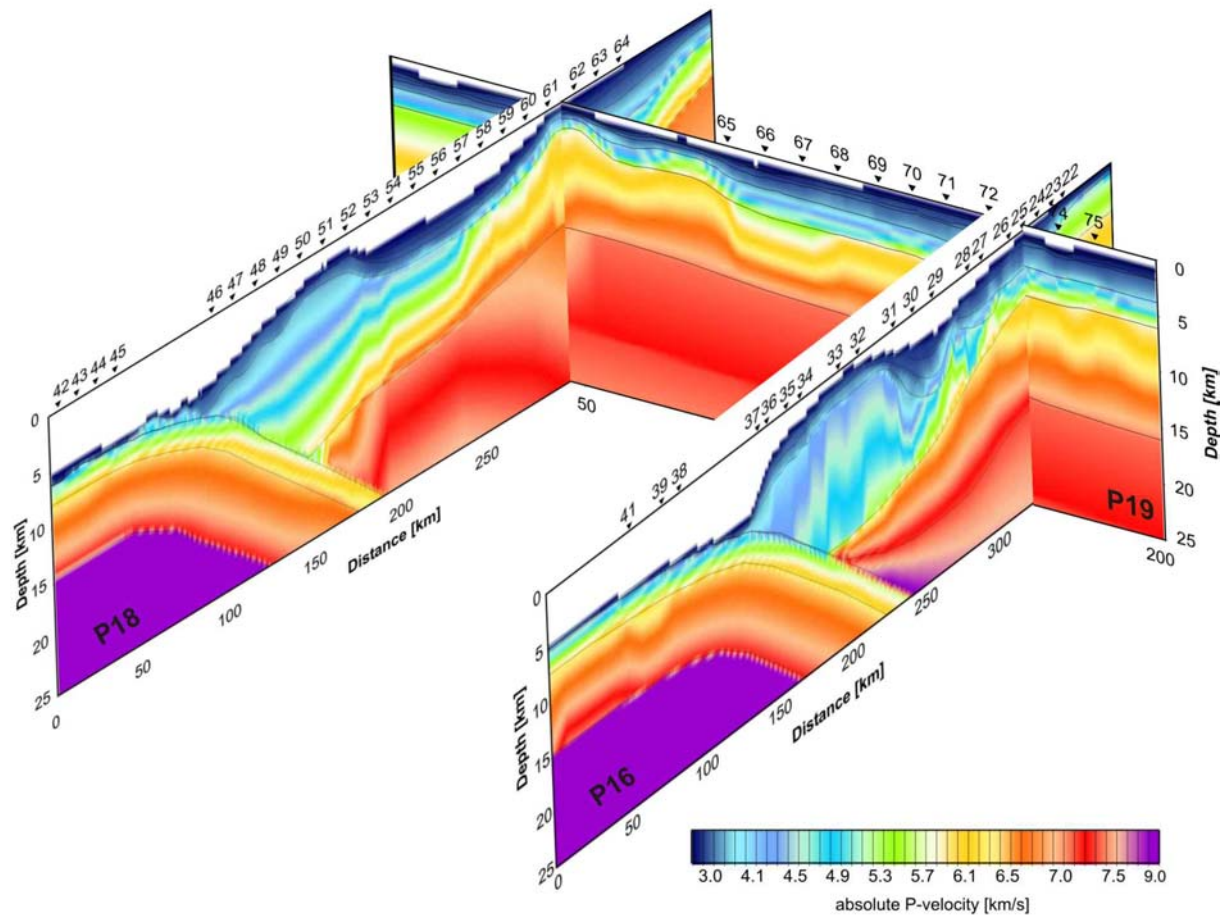


**Figure 4.7:** The forward models of the three seismic profiles were merged together. The oceanic plate subducts with a dip angle of  $10^\circ$ . The crustal thickness increases from 8.5 km (P18) to 9.5 km (P16). The sedimentary basin on the western profile is undisturbed compared to the basin along profile P16.

In summary, the top of the subducting oceanic plate is well identified on both dipping lines. Both dipping profiles indicate a dip angle of  $10^\circ$  in the upper 25 km depth and a crustal thickness of 8.5 km along profile P18 increasing to 9.5 km along the eastern profile P16, which is thicker than the global average.

However, in regard of the tomographic studies presented in the following chapters, mainly the Java basin and the shelf area up to the coast line and onshore Central Java is of interest. Therefore, only this section of the forward models of profile P16 and P18 are described in the following. The sediment in the forearc basin of the western profile P18 is approximately 3 km thick and shows mainly undeformed layers. The basin is about 100 km long and extends from profile km 180 to the shelf at profile km 300. The basement high, which was already mentioned in the description of the coast parallel profile P19, is located at profile km 300 of profile P18. The basement high with its higher velocities than in the surrounding area, could also be identified in the seismic reflection data, and furthermore in the gravity and magnetic data.

In contrary, the forearc basin along the eastern profile P16 is strongly disturbed. The basin strata onlap at the outer forearc high and are tilted landward. P-wave velocities of 4.5 km/s on the base of the sediments were defined whereas the P-wave velocities on the western profile P18 are only 4.0 km/s.

## **4.2 Gravity Modeling**

To constrain the seismic velocity depth model of profile P19, the two-dimensional gravity response of the model was calculated using the MacRay software. Basis of the gravity model are the structures obtained in the seismic model to which standard constant density values were assigned (Figure 4.8). The calculated gravity values are compared to the measured gravity data acquired by the BGR during cruise SO 179 (dotted line in Figure 4.8). The measured data show a positive gravity anomaly along the coast parallel profile, mainly around 10 mGal. Higher gravity values can be observed in the area of the basement high (~ profile km 50) with values of about 170 mGal. The modeled data fits the measured gravimetric data to within  $\pm 20$  mGal and thus the two-dimensional modeling corresponds well to the observed gravity values along the coast parallel profile P19.

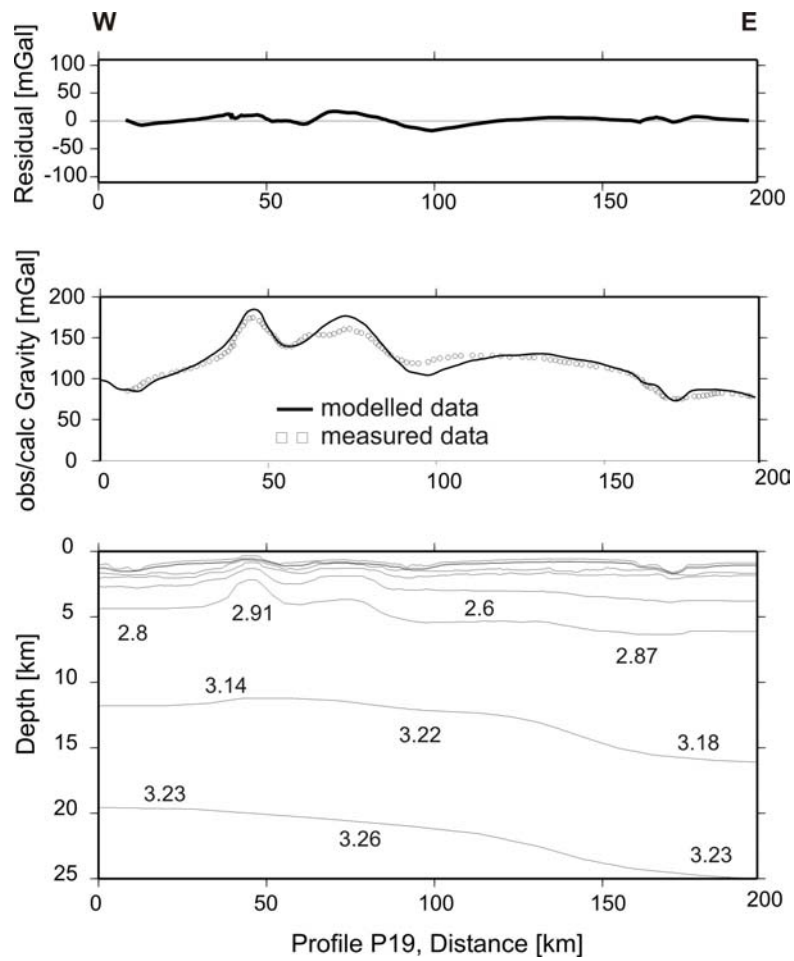


**Figure 4.8:** Forward modeling result of the gravity response of profile P19. Increased gravity values are detected at the cross point of profile P19 and P18 (here at profile km 50). This anomaly is conform with higher P- wave velocities and indicates a high density body in the shelf area.

## 5. TOMOGRAPHIC COMPARISON STUDY

### 5.1 Introduction

In the framework of the MERAMEX- MERapi AMphibious Experiments, Koulakov et al. (2007) performed local earthquake tomographic studies and I conducted tomographic studies of the active and passive seismic data. In both tomographic studies code LOTOS-06 was used, which was initially designed to process passive seismic data. Although code LOTOS-06 is newly developed, several data sets including ISC data and other local earthquake data sets were successfully inverted using this code or previous versions of it (e.g. Koulakov et al. 2006 a, b & c). Code LOTOS-06 is actually applied to different study areas: Central Java, Sunda Strait (Mt Krakatau), Sumatra (Mt Toba), Costa Rica, Southern Andes etc. To analyse the three-dimensional active seismic data, which consist of the recorded airgun signals within the onshore array (Figure 4.4), code LOTOS-06 had to be adapted and tested. Hence, to get an impression of the quality and accuracy of the obtained results, I also performed the tomographic studies of the active seismic data using the well tested and often applied three-dimensional travel time tomography code developed by J. Hole (1992) (later called 3DTH) (Hole 1992; Hole et al. 1992; Hole et al. 1993).

In this study, I present the results of the tomographic inversion using the active seismic data recorded within the onshore MERAMEX network which was performed with these two codes. The obtained models of both codes are discussed in detail. Additionally, the tomographic results are compared with the forward models of the wide-angle seismic data (see Chapter 4).

Although both tomographic codes were successfully applied and tested, several questions remain open when comparing their results, such as:

- the influence of the grid spacing,
- the influence of the used routine to trace the rays through the volume,
- the influence of the applied method for matrix inversion,
- the influence of the used background velocity model and
- the influence of the used travel time information as for first breaks, near vertical reflections, later reflections and refractions.

Comparing the forward models with the tomographic models, one has to bear in mind that the tomographic studies comprise only first arrival travel times. However, in the forward modeling process of the OBH data not only first break travel time information but also near vertical reflections of the surface layers from the reflection seismic data and later reflections and refractions detectable in the OBH sections were included.

The ray coverage of the active seismic data recorded onshore was plotted and several synthetic tests were performed. Both codes obtain similar results in checkerboard tests. Nevertheless, differences in the accuracy can be detected with regard to the calculated RMS travel time residuals.

The forward models were performed in two dimensions and gravity data was included to constrain the seismic model additionally. Although the modeling process comprised several data sets, three-dimensional effects play a role in the two-dimensional modeling. This is especially evident during the modeling of the basement high at the cross point of the two seismic profiles P18 and P19 and during the elongation of the seismic profiles onshore Central Java, if stations located not in a straight line in continuation of the seismic profiles were used.

## **5.2 The Techniques**

### **5.2.1 Code LOTOS-06**

Code LOTOS-06 was developed by I. Koulakov (2006, 2007) to perform local earthquake tomographic studies. An updated version of this algorithm allows to perform tomographic studies of active, three-dimensional seismic data (Wagner et al. 2007). The following description of the algorithm is only valid for active seismic data, in case of passive seismic data the localization of the sources has to be included (see also Figure 5.1 presenting a flow chart for code LOTOS-06 valid for both active and passive seismic data).

The first step was a travel time correction equivalent to a virtual shift of the shot points from the water surface to the bottom of the sea. The tomographic inversion was performed by several iterative steps, in which the travel times were computed for the velocity model derived from the previous iteration. The bending method of ray tracing based on an algorithm proposed by Um and Thurber (1987) is applied. The parameterisation was based on an adaptive node density, and was configured according to the ray density in the study volume.

The nodes were placed in vertical planes and a fixed 5 km minimum spacing between the nodes prevented extreme node concentrations in areas of high ray density. To reduce effects and artifacts caused by a predefined grid orientation, four differently oriented grids ( $0^\circ$ ,  $45^\circ$ ,  $90^\circ$  and  $135^\circ$ ) were used in the inversion procedure and then stacked. The velocity values were calculated at nodes forming tetrahedral blocks and the velocity distribution in these blocks was interpolated linearly. The matrix of the first derivatives of travel time versus model parameter was computed numerically along rays using the approach proposed by Koulakov and Sobolev (2006). An additional matrix block controlled the smoothing of the three-dimensional velocity models. Inversion of the matrix was performed using a least square method (Van der Sluis & Van der Vorst 1987) and resulted in velocity values distributed in a three-dimensional irregular grid. This irregular grid was subsequently recomputed to a regular grid and smoothed.

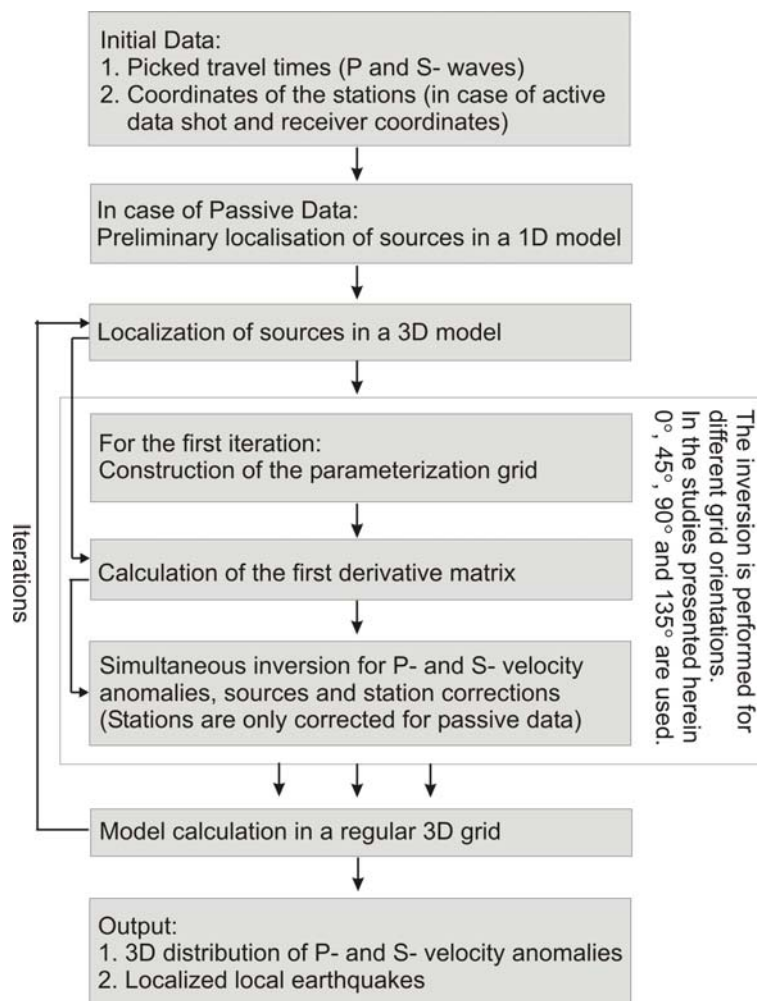


**Figure 5.1:** Flow chart for code LOTOS-06 valid for both active and passive seismic data.

### 5.2.2 Code 3DTH

The tomography code developed by J. A. Hole (1992) is designed to perform three-dimensional tomographic studies of refraction data. The code encompasses of two steps: the forward modeling of the ray paths and the inversion procedure. The first arrival travel times were forward modeled in three dimensions following the finite difference travel time algorithm described by Vidale (1990). Finite difference operators based on the Eikonal equation were used to propagate first arrivals from direct, refracted, diffracted, or head waves through a grid of velocity nodes. The first arrival travel times were calculated to all grid points in the model, which were uniformly spaced in three dimensions. The finite difference operator used the average slowness across a grid cell. In the inversion procedure, the linear relationship between the travel time residuals and the slowness perturbations was used. This resulted in a matrix consisting of the lengths of each ray in each grid. The linearized inversion problem was solved using a backward projection algorithm. The inversion results were gridded by a process that interpolates the model between the rays and also smoothed the model. For additional smoothing, a 3D moving average filter was applied. As soon as all rays were traced through the model, the information about number and length of rays and the number of rays penetrating through each cell was used to compute the slowness perturbations at the grid points. The model perturbations were added to the slowness model and then used as new reference model for the next iteration.

The initial model in our study was 250 by 300 km in area, extended from 2 to -30 km in depth and was coarsely sampled at a 1 km grid spacing. This resulted in 251x301x23 nodes for which the velocities and travel times were defined. Prior to the tomographic studies, the travel times were corrected equivalent to a virtual shift of the shot points from the water surface to the bottom of the sea.

In the following, the tomographic results obtained with the two codes are compared with the forward models of the OBH data. To facilitate the comparison, the main differences between code LOTOS-06, code 3DTH and the forward modeling routine are summarized in Table 5.1.

*Table 5.1: Comparison of the used methods: interactive (forward) model, code LOTOS-06 and code 3DTH.*

	<b>Interactive Model</b>	<b>LOTOS-06</b>	<b>3DTH</b>
<b>Type of used travel times</b>	<ul style="list-style-type: none"> <li>- First break travel times</li> <li>- Near vertical reflections of surface layers</li> <li>- Later reflections &amp; refractions</li> </ul>	Only first break travel times	Only first break travel times
<b>Type of constraints</b>	<ul style="list-style-type: none"> <li>- Not only first break travel times included.</li> <li>- Reflection data constrains the upper sedimentary layers</li> <li>- Bathymetry data for exact position of the sea floor.</li> <li>- Acquired gravity data included in the modeling of the seismic data .</li> <li>- Onshore receivers used to elongate the 2D model and to constrain the OBH stations located close to the coast.</li> </ul>	Onshore receiver array	Onshore receiver array
<b>Initial model</b>	Two layers: the water column ( $v_p=1.5$ km/s) and a sedimentary layer divided by the sea floor	1D or 3D	1D or 3D
<b>Forward modeling technique to calculate travel times</b>	Stepwise integration of first order differential equations: $d/dt x(t)=V(x,z) \sin\theta$ , $d/dt z(t)= V(x,z) \cos\theta$ , $d/dt \theta(t)=dV/dx \cos\theta - dV/dz \sin\theta$ ( $\theta =$ incident angle from the vertical)	Bending method of ray tracing.	Finite difference travel time algorithm providing a solution to the Eikonal equation.
<b>Inversion problem</b>		Matrix is solved using a least square method.	Matrix is solved using a backward projection algorithm.
<b>Grid spacing algorithm</b>		Variable grid spacing, adaptive node density configured after ray density	uniformly spaced grid in three dimensions
<b>Smoothing process</b>		<ul style="list-style-type: none"> <li>-Matrix block controls smoothing of 3D velocity models</li> <li>-Smoothing of 2D sections in the visualisation routine</li> </ul>	<ul style="list-style-type: none"> <li>- Interpolation of rays after each iteration</li> <li>- 3D moving average filter</li> </ul>

### 5.3 Resolution Tests of the Active Data set

Prior to the comparison of the results of the two codes, the quality and accuracy of the active data had to be checked. A number of synthetic tests were performed, of which herein only the results of the checkerboard tests are presented. The shown tests were obtained with code LOTOS-06, which provided the faster and more elegant and comfortable way to perform synthetic testing. Checkerboard tests were also conducted with code 3DTH resulting in comparable images. However, LOTOS-06 provided several options to construct checkerboards with and without space in between the boards or the construction of realistic anomalies whereas in case of code 3DTH different routines had to be written or adapted to obtain comparable test layouts. In addition, LOTOS-06 had the advantage to add random noise to the data, which was not included in the routines for 3DTH.

Due to the small shot spacing which was significantly smaller than the size of the retrieved anomalies, only 10 % of the active data was used in the synthetic testing to save computer time. The difference in applying the complete data set or just a subset results in comparable images with small differences in the amplitudes of the anomalies regarding small scale images. Two different initial synthetic models were defined in the whole area as periodical anomalies of 50 km and 30 km in size (Figure 5.2 & 5.3). The amplitude of the velocity contrast was set to  $\pm 7\%$ . In the presented synthetic tests, 0.2 s of RMS random noise was added to the travel times. The diagrams in Figures 5.2 and 5.3 show the results of two different checkerboard layouts with identical anomaly sizes next to each other. The upper diagrams present checkerboard anomalies in between which a 10 km space was added and the lower diagrams display checkerboard anomalies without any space in between. Comparing the results of the checkerboard tests reveals that the ones with space in between the boards result in a much higher accuracy of the resolved anomalies after the inversion. Another important advantage of adding space in between the anomalies is that the resolved anomalies correspond in amplitude better to the initial anomalies, whereas without space too high amplitudes are obtained (see lower diagrams in Figure 5.2 & 5.3). For checkerboard anomalies of 50 km in size the anomalies are resolved. Even at a depth of 20 km, the anomalies are well defined in the center of the study area. In case of the 30 km size anomalies, smearing starts at a depth of about 15 km whereas the center of the research area is still resolved well.

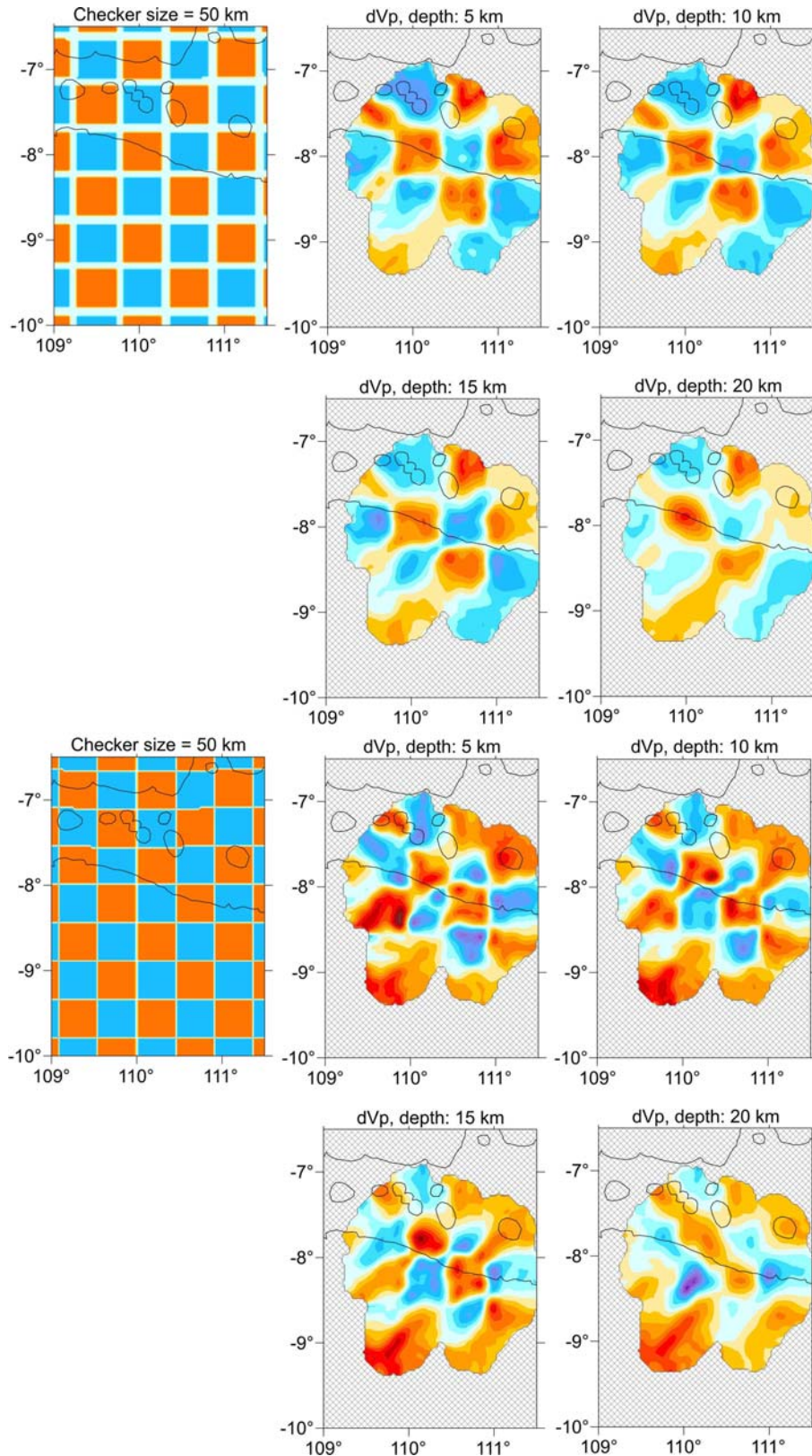


**Figure 5.2:** The left images show the initial shape of the checkerboard anomalies of 50 km in size with amplitudes of  $\pm 7\%$  and 0.2 s RMS random noise. In the upper diagrams, 10 km space in between the anomalies was added.

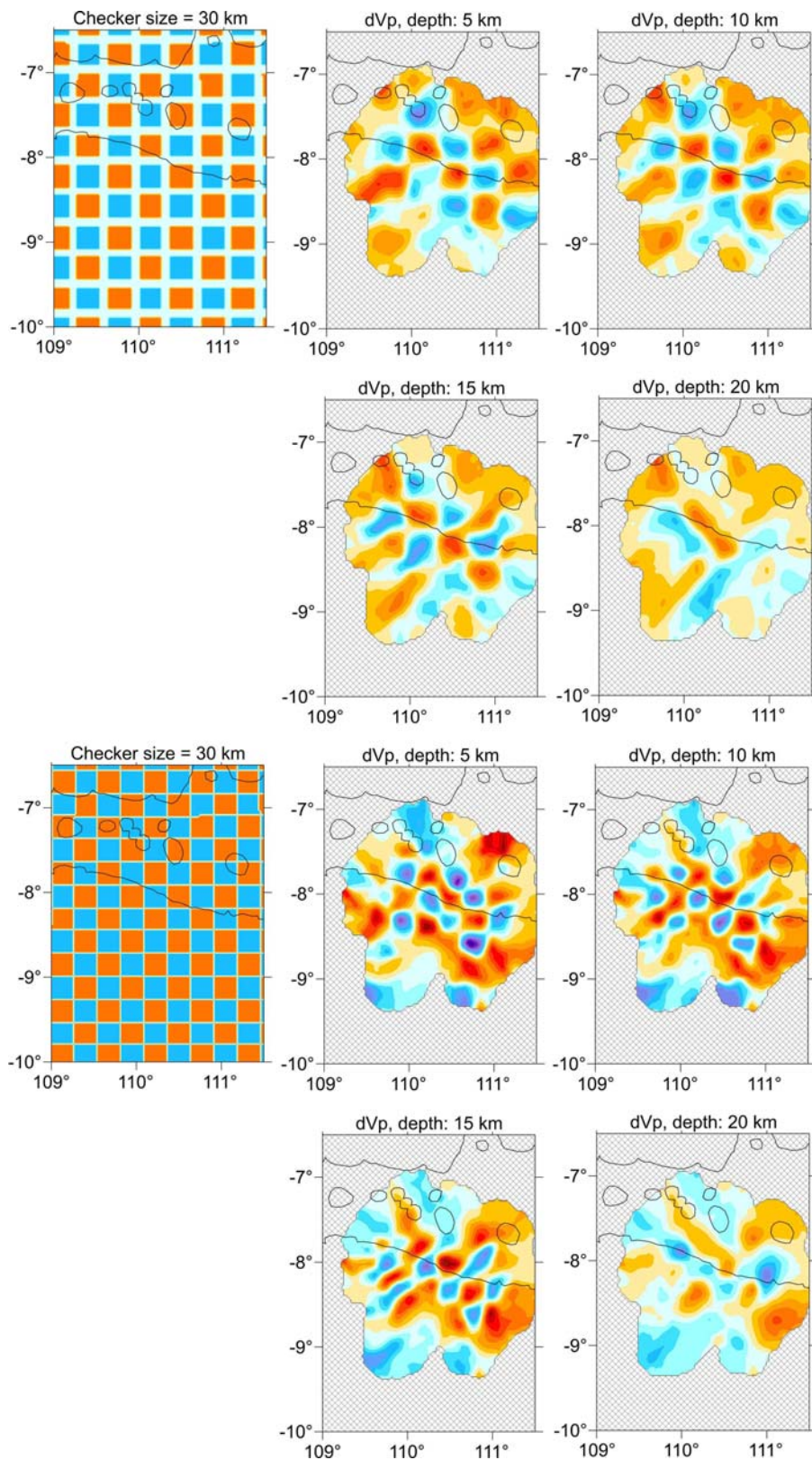


**Figure 5.3:** The left images show the initial shape of the checkerboard anomalies of 30 km in size with amplitudes of  $\pm 7\%$  and 0.2 s RMS random noise. In the upper diagrams, 10 km space in between the anomalies was added.

## 5.4 Results

Both software packages were run with the following identical features:

1. The complete data set was used for the inversion.
2. To improve the travel time calculations, all shots were moved on top of the sea bottom. This corresponds to a shift in three-dimensions in position and time. In case of LOTOS-06 the corrections were performed in the first step of the code, whereas in case of 3DTH, this information had to be included in the loaded travel time data.
3. Due to the reciprocity of the travel times, the shot data were modeled by shooting at the onshore receivers and calculating the travel times to the offshore shots positions.

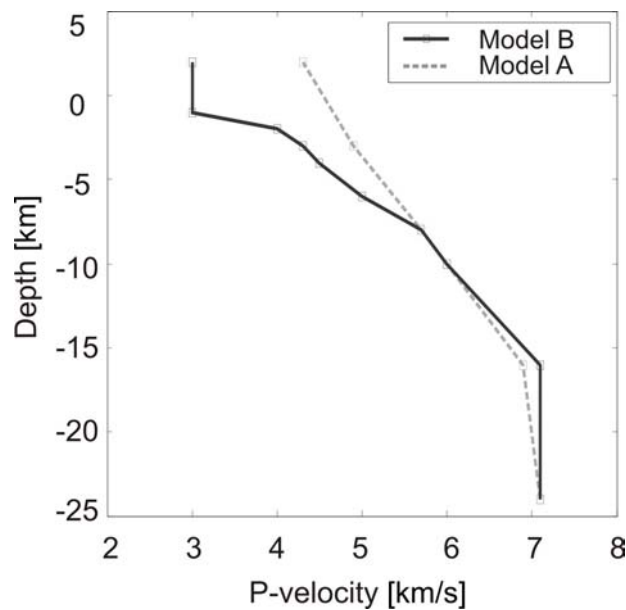


**Figure 5.4:** One-dimensional initial model A (dashed gray line) and B (black line) used for the tomographic calculations.

The used initial models are based on the forward modeling results of the OBH data. For the one-dimensional models A and B (Figure 5.4) an average velocity distribution was chosen. The reason for presenting results of two one-dimensional models (A and B) was that the codes handled the velocity gradients differently. In addition, 3DTH needed lower velocities in the upper crust as background velocity than LOTOS-06 to calculate corresponding values for the sedimentary layers in the upper 5 km depth. A three-dimensional background model (C) (see Figures 5.7 – 5.11) was applied because the results obtained with the one-dimensional models were not satisfying in the offshore part south of profile P19 along profile P16 and P18.

To construct model C, the velocity distribution of the forward models (Figures 4.5, 4.6 and 4.7) along the seismic profiles P16, P18 and P19 was converted to a regular 1 km grid using inter- and extrapolating routines and then smoothed. Vertical slices along the profiles in Figures 5.7 – 5.11 show the smoothed three-dimensional background velocity model.

The comparison of the tomographic results is presented along six vertical profiles: four of them are oriented parallel to the coast: P1, P2, P3 and P19 and the two profiles P16 and P18 are oriented coast perpendicular (Figure 5.5). To get an impression of the quality of the active data recorded in the onshore array, the ray coverage along each of the six profiles is presented in Figure 5.6. Only 10 % of the rays detected within a 20 km wide band are plotted in these sections. The ray coverage is highest in the area between profile P2 and profile P19.

By comparing the results of code LOTOS-06 and 3DTH, it is obvious that the retrieved structures are almost identical whereas the absolute P velocities vary depending on the used code and background velocity model. Both codes were additionally applied with the three-dimensional initial model C, which includes information about the water column of the sea and the coast line. This information is very important to achieve an appropriate depth image of the ocean bottom and the sedimentary layers of the offshore seismic profiles P16 and P18. Both codes yield higher seismic velocities using initial model C instead of A and B in the corresponding depth sections.

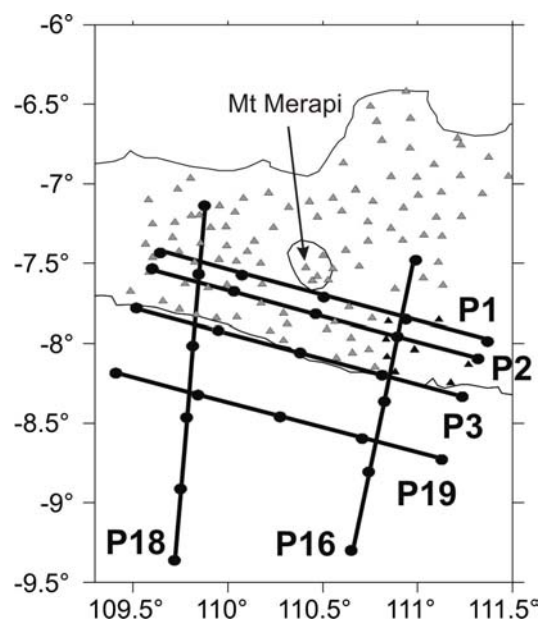


**Figure 5.5:** Profile locations of the vertical sections shown in Figures 5.7- 5.11. The dots along the profiles refer to the marks for 0, 50, 100, 150 and 200 profile km.

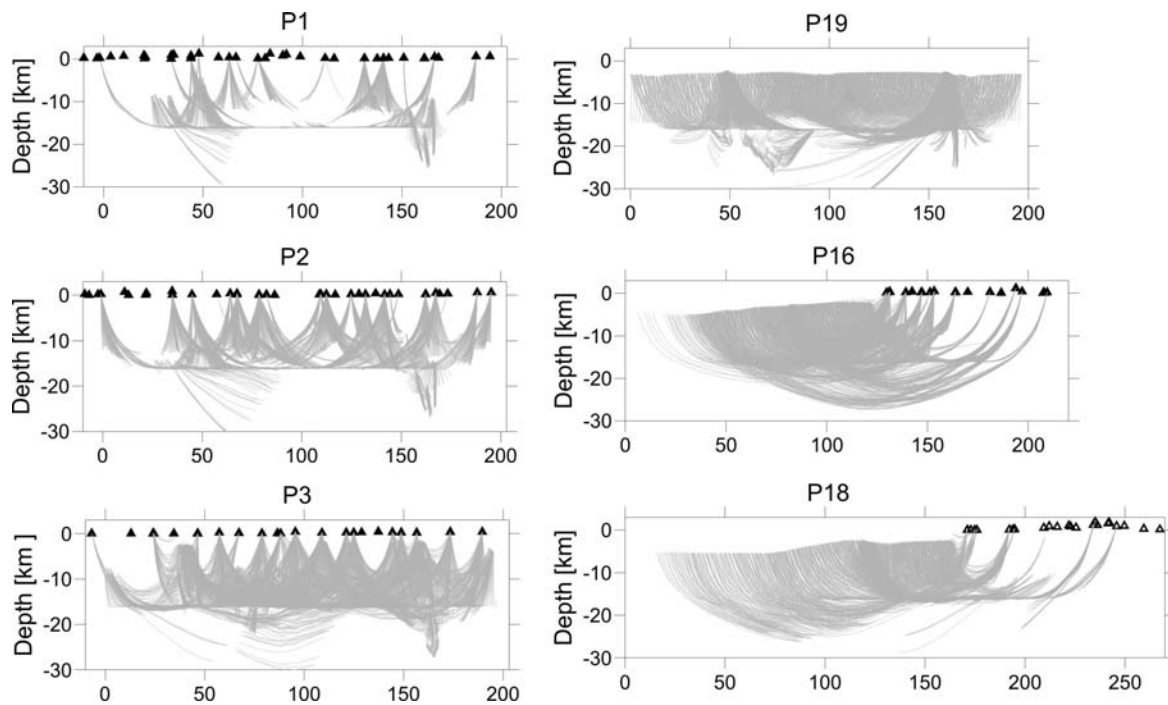


**Figure 5.6:** Rays paths in a 20 km broad band along the profiles marked in Figure 5.5. Only one of ten rays is plotted. The triangles correspond to the onshore receiver stations located within this area.

In the following, each profile is discussed in detail. The three onshore profiles P1, P2 and P3 located parallel to the seismic profile P19 agree well comparing the tomographic results obtained with the two codes and different initial models.

Profile 1 shows a strong P-wave velocity reduction (15- 20 %) between profile km 50 and 150 independent on the used code and initial model. This anomaly belongs to the southern edge of a larger low-velocity anomaly extending WNW-ESE along the footprint of the volcanic arc (see Chapter 7). The tomographic calculations with background model A obtain the low-velocity anomaly between profile km 60 and 135. Using model B, the anomaly shrinks to a diameter of 60 km in case of LOTOS-06, whereas 3DTH doesn't show this change. Initial model C provides the velocity reduction in an area slightly shifted to the east, whereas this shift is more distinct in case of code 3DTH. In general, the velocity reduction in this area is about 5 % stronger in case of code 3DTH compared to code LOTOS-06.

Profile 2 marks a low-velocity anomaly dividing the forearc into two blocks at profile km 100. This negative anomaly is elongated in NNE-SSW direction and extends from the strong low-velocity anomaly located in the area of Merapi volcano along profile P1 and the southern coastline. The division of the forearc into two blocks is very distinct in all models. In case of initial models A and B, LOTOS-06 resolves overall higher seismic velocities than code 3DTH. All models obtained with 3DTH show a slightly shifted low-velocity anomaly to the east compared to the model of code LOTOS-06.

Profile P3 is located approximately on top of the coastline. This profile still shows some disturbances in the velocity model between profile km 50 and 150, but along this profile the tomographic models show strong discrepancies. LOTOS-06 yields a heterogeneous velocity distribution around profile km 100. These heterogeneities are not detectable in code 3DTH using model A, B and C. In case of code LOTOS-06, all models show reduced seismic velocities between profile km 20 and 100 up to 10 km depth, whereas the velocity reduction in this area is not that strong in the model obtained with initial model C. Code 3DTH provides comparable images for the one-dimensional initial models with lower seismic velocities between profile km 20 and 100 but the seismic velocities are reduced up to ~ 13 km depth.

Profile P19 is located approximately 50 km further south of profile P3. The significant structure along this profile is a basement high with elevated seismic velocities located between profile km 40 and 90, which could be modeled using the OBH data (see Chapter 4 and Figure 5.9). The velocity increase is evident in all tomographic results independent on the initial model. One main difference in the results of the two codes is that code LOTOS-06 resolves higher seismic velocities in 0 to 5 km depth in case of the one-dimensional models A and B compared to the models of code 3DTH. This difference is especially evident in the area of the basement high, along which LOTOS-06 resolves in 2 km depth seismic velocities of ~ 5.8 km/s and code 3DTH obtains seismic velocities of ~ 5 - 5.3 km/s. Compared to the interactive model of the OBH data, LOTOS-06 yields slightly too high velocities whereas 3DTH obtains too low velocities in the appropriate depth sections. In case of initial model C, both tomographic models correspond well to the interactive model. Conferring all tomographic results with the interactive model of profile P19, then the models with initial model C resemble in the velocity distribution at corresponding depth sections better to the forward model than the results of the codes with initial model A and B.

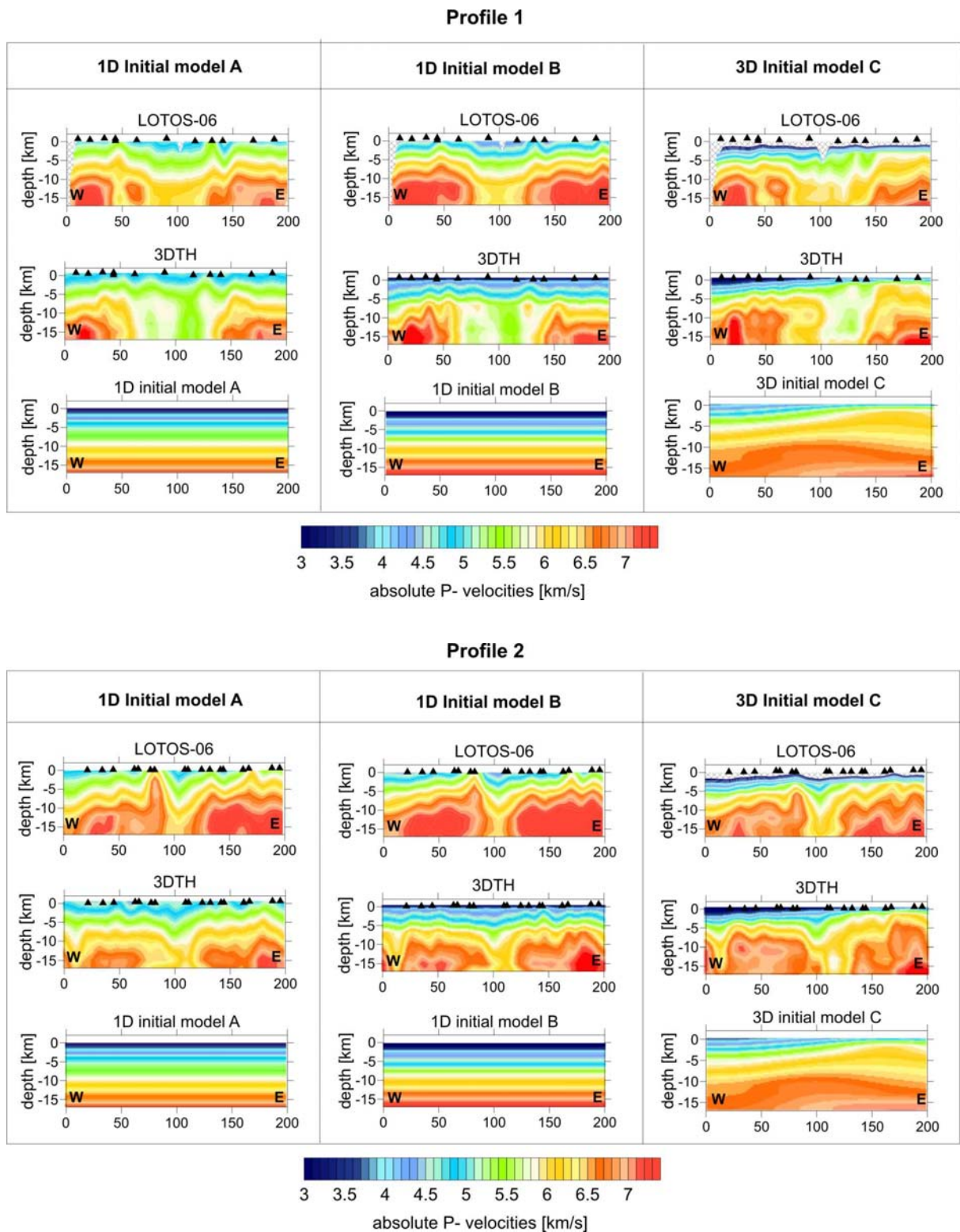


**Figure 5.7:** Comparison of the tomographic models along the onshore profiles 1 and 2. The upper diagrams in the rectangles refer to the result of code LOTOS-06, the middle diagrams to the results of code 3DTH and the lower diagrams show the used initial model. For each profile, two 1D and a 3D initial model was applied.

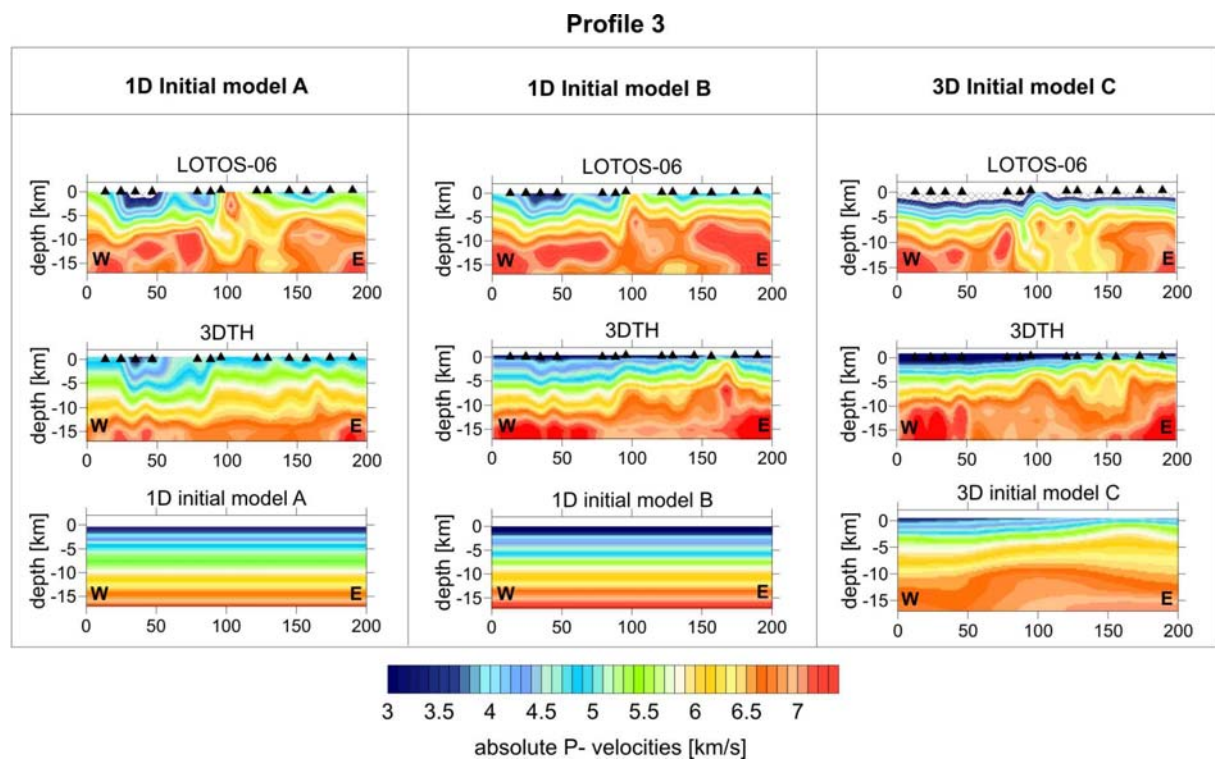


**Figure 5.8:** Comparison of the tomographic models along the coast line (Profile 3). The upper diagrams in the rectangles refer to the result of code LOTOS-06, the middle diagrams to the results of code 3DTH and the lower diagrams show the used initial model. For each profile, two 1D and a 3D initial model was applied.

However, code 3DTH shows a low-velocity anomaly at profile km 110 along profile P19, which is very pronounced using the one-dimensional models. LOTOS-06 achieves only in case of the three-dimensional model C a velocity reduction in this region which is not evident if not knowing of the anomaly. This anomaly was not detected during the forward modeling of the OBH data. If this anomaly is real and not a smearing effect, it could be the connection to the low-velocity anomaly dividing the forearc into two blocks. Recapitulating, the low-velocity anomaly extends from Merapi volcano in the north further south up to profile P19 always approximately located around profile km 100. The anomaly is strongest along profile P1 and P2 and gets weaker at the coastline and in the offshore part. In the onshore area, this low-velocity anomaly coincides with the location of one of the most prominent fault zones in the area, the Opak River fault, which trends N40°E.

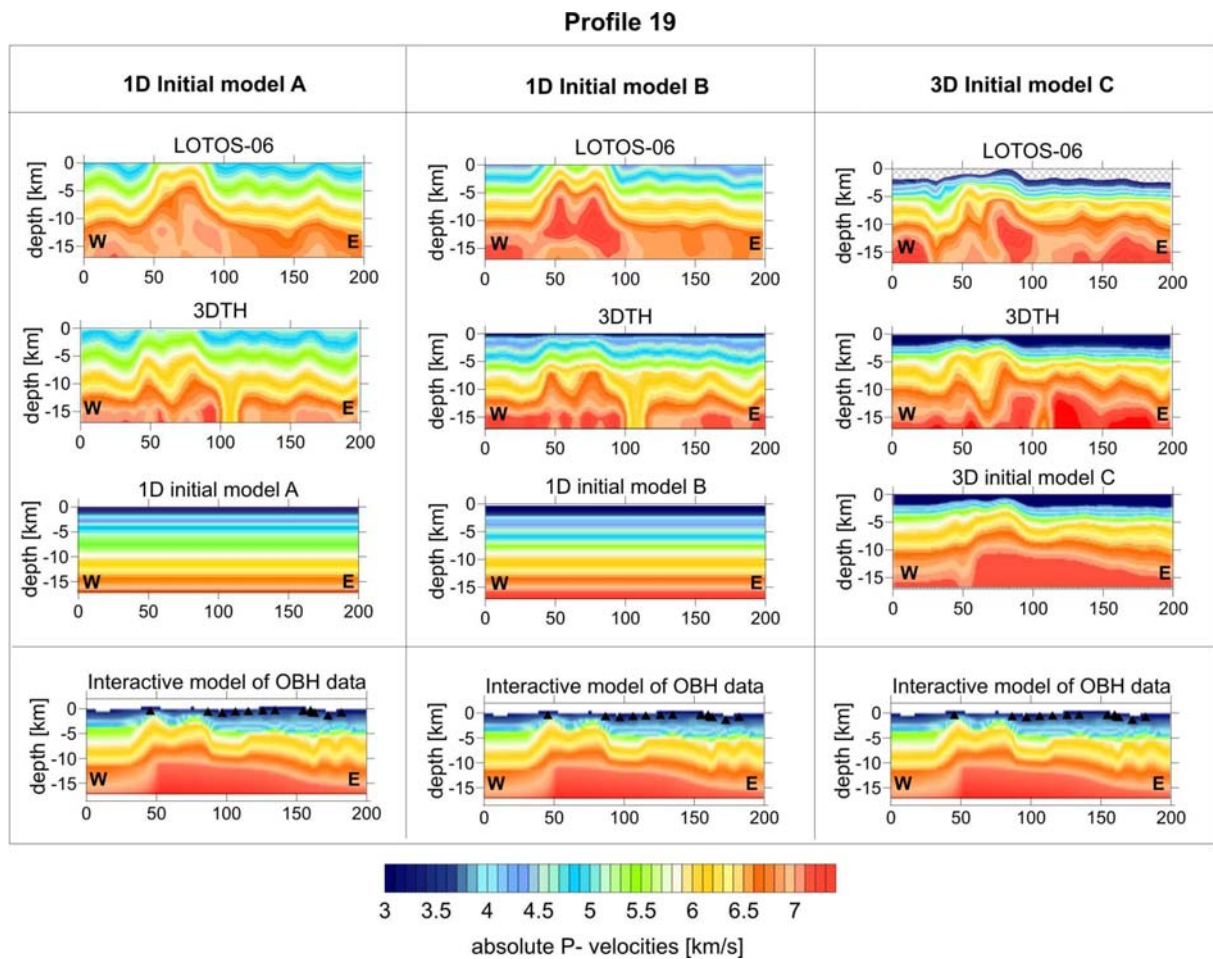


**Figure 5.9:** Comparison of the tomographic models along the coast parallel profile P19 . The upper diagrams in the rectangles refer to the result of code LOTOS-06, the middle diagrams to the results of code 3DTH and the lower diagrams show the used initial model. For each profile, two 1D and a 3D initial model was applied. For comparison the interactive model of the OBH data is presented in the lower box.

The quality of the tomographic models of the two dip lines differs from that of the coast parallel models discussed above. The ray coverage in the central part of the study area, which coincides with the locations of the coast parallel profiles P1, P2, P3 and P19, is much higher than along profiles P16 and P18 (Figures 5.10 and 5.11). Along the dip lines, rays travel mainly in south-north direction, and reverse shots are missing. Furthermore, crossing rays exist only north of airgun profile P19. The two dip lines are approximately 150 km apart from another, resulting in a too large distance that rays emitted along profile P16 could cross rays emitted along profile P18 south of the coast parallel profile P19. Therefore, mainly the region located between the cross points of the two dip lines with profile P19 and the onshore area should be used to quantify the codes in comparing them with the forward models.

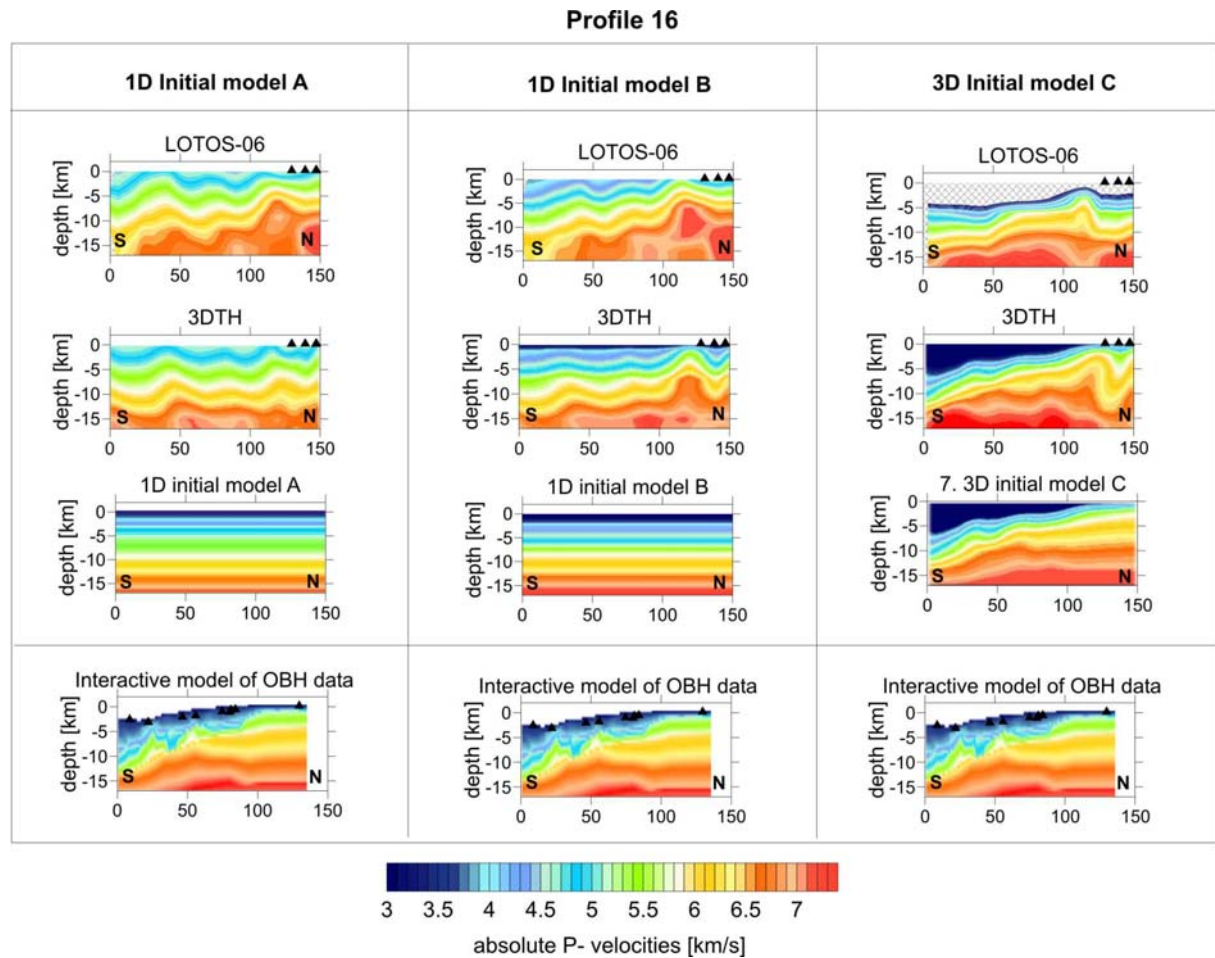


**Figure 5.10:** Comparison of the tomographic models along the eastern lip line P16. The upper diagrams in the rectangles refer to the result of code LOTOS-06, the middle diagrams to the results of code 3DTH and the lower diagrams show the used initial model. For each profile, two 1D and a 3D initial model was applied. For comparison the interactive model of the OBH data is presented in the lower box.

Taking the forward model as reference model for these two profiles, the models obtained with initial model C match best. This is not astonishing because a-priori information like the thickness of the water column and the sedimentary layers was already included in the background model. Such kind of information is necessary to achieve a reliable model if crossing rays and reverse shots are missing. Thus, code 3DTH requires a-priori information to achieve the dip of the sedimentary layers close to the coast along profile P16. This fails completely in case of 3DTH using initial model A (see Figure 5.10).

The tomographic models of profile P18 obtained by both codes using initial one-dimensional models show an almost horizontal layering between profile km 0 and 100 (Figure 5.11). Only with initial model C, both codes achieve the correct dip of these layers and the thickness of the water column.

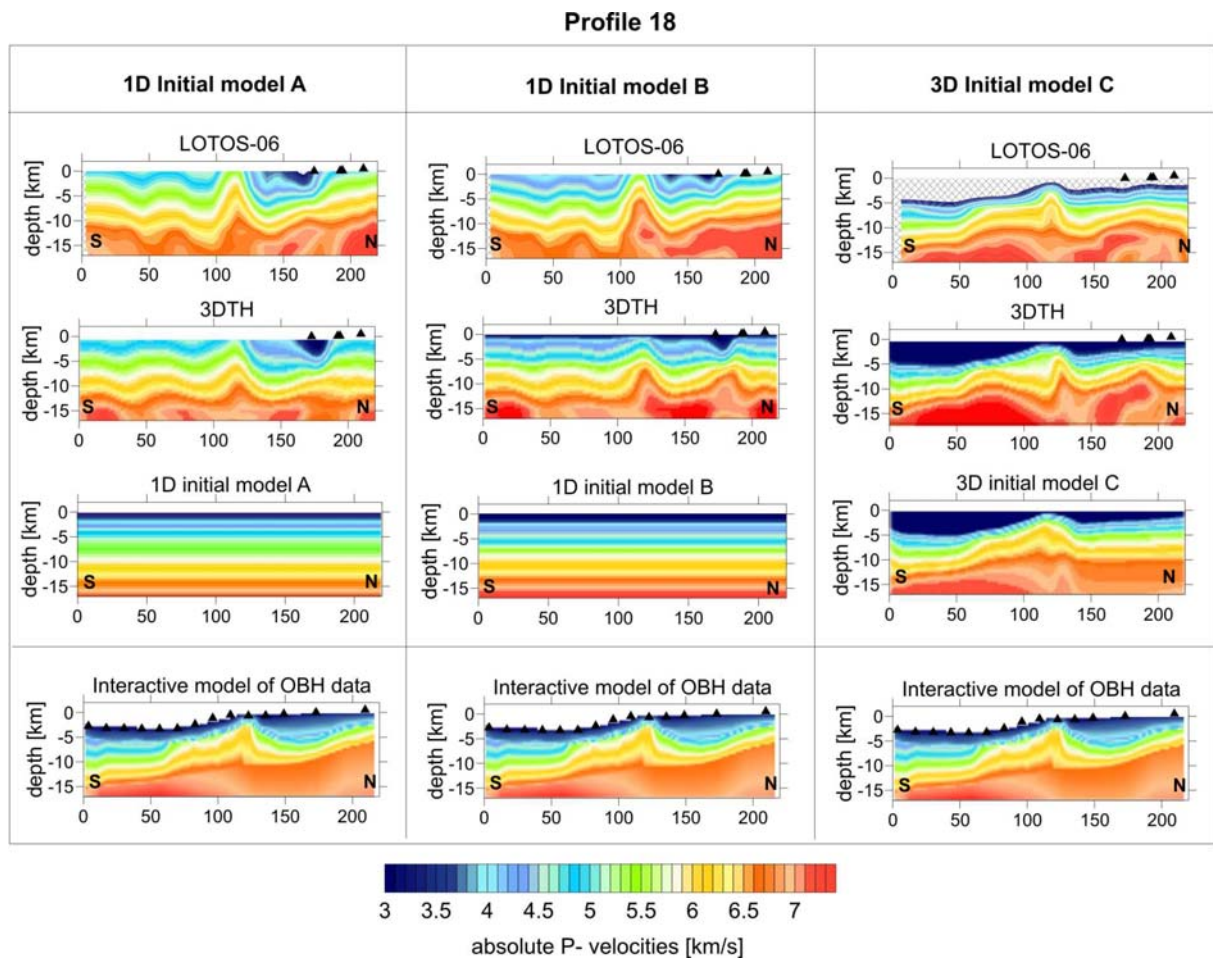


**Figure 5.11:** Comparison of the tomographic models along western dip line P18. The upper diagrams in the rectangles refer to the result of code LOTOS-06, the middle diagrams to the results of code 3DTH and the lower diagrams show the used initial model. For each profile, two 1D and a 3D initial model was applied. For comparison the interactive model of the OBH data is presented in the lower box.

Profile P18 crosses profile P19 exactly at the basement high at profile km 115. All tomographic models resolved the velocity increase in this region whereas code LOTOS-06 resolves again too high and code 3DTH too low seismic velocities compared to the interactive model. The basement high is limited in the north by a sedimentary basin extending to the coast line located at profile km 190. Both structures, the basement high and the sedimentary basin correspond well in the tomographic models using one-dimensional models. However, LOTOS-06 resolves a higher velocity gradient in the onshore area between 0 and 10 km depth compared to the models of code 3DTH. Again, the results of the codes using the three-dimensional initial model C match best to the forward model of the OBH data.

Recapitulating, using one-dimensional models, LOTOS-06 yields reliable results which also correspond well to the forward models, whereas the overall velocities are slightly too high. Code 3DTH obtains also reliable results in well covered areas like the area located between profile P2 and P19 with overall lower seismic velocities compared to the interactive model and the tomographic models of code LOTOS-06. However, the dip lines P16 and P18 show some discrepancies, especially in areas with low ray coverage (e.g. south of profile P19). Including a three-dimensional initial model, both codes resolve results which are very similar to the forward models even in areas with low ray coverage.

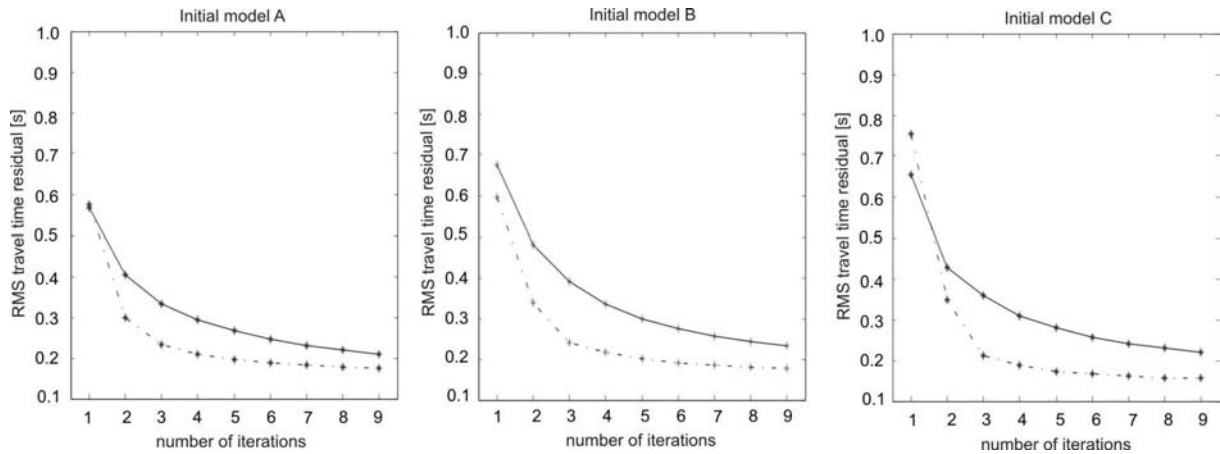
### 5.5 RMS Travel Time Residuals

The two codes were compared in consideration of RMS travel time residuals which were recalculated in both cases because the residuals are computed differently in the codes. Therefore, I used the travel time difference  $dt = dt_{pick} - dt_{cal}$  provided by the programs. The RMS residuals were calculated using the following equation:  $RMS\ dt = (\sum dt^2 / nshots)^{1/2}$  with  $nshots$  representing the number of shots.

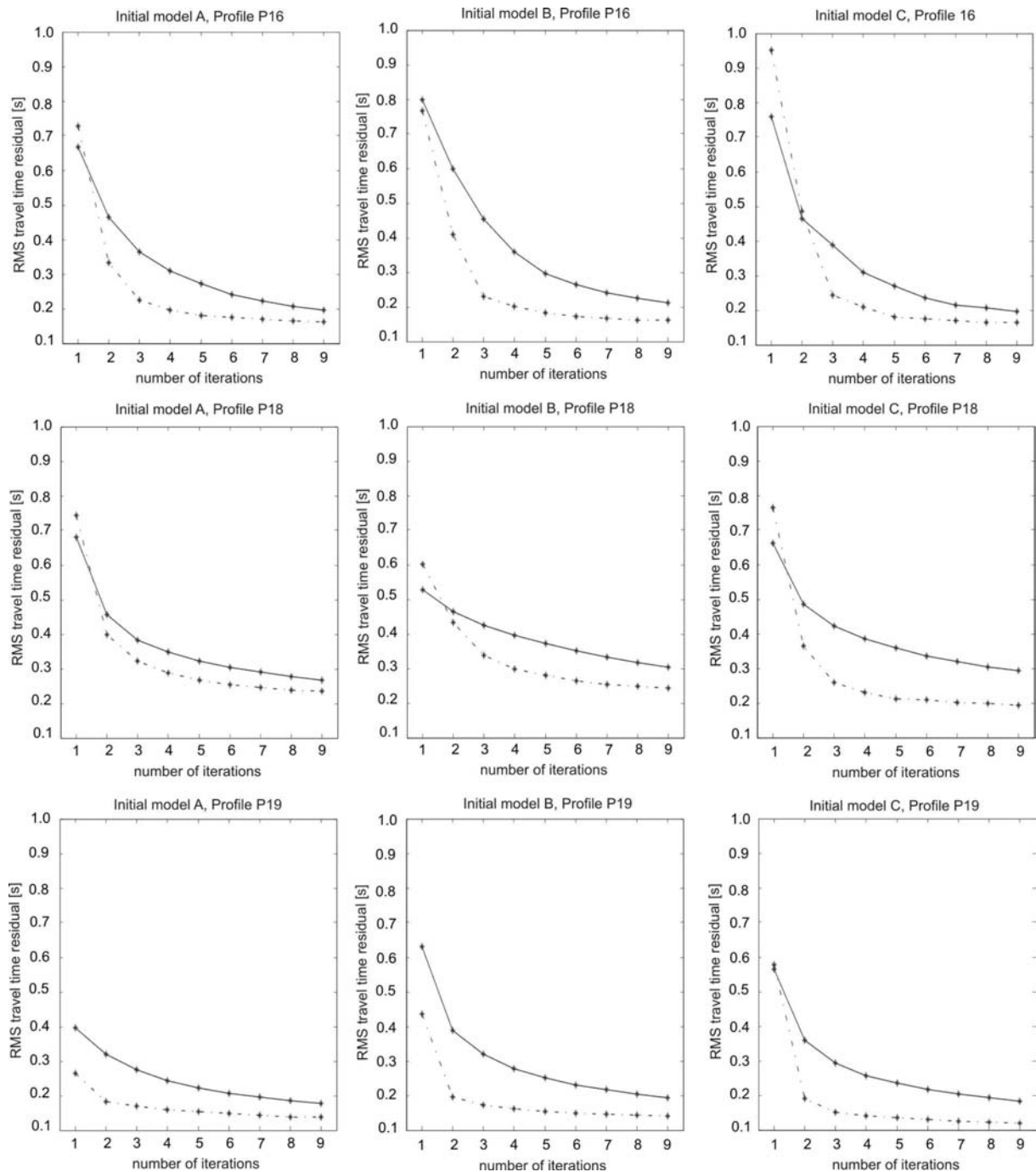
The initial shot and receiver array used in this study was identical in both codes but due to different criteria for the quality of the shots, the data amount resulted in different numbers of rays in the two codes. To calculate the residuals, only rays accepted by both codes were taken into account for comparison reasons.

Figure 5.12 presents the RMS travel time residuals for nine iterations for both codes and the used initial models. The smallest residuals were obtained using code LOTOS-06 with initial model A and C, followed by 3DTH with initial model A. Code 3DTH with initial model C obtained slightly higher residuals than with initial model A. Regarding increasing iteration numbers, it is obvious that the residuals obtained using code LOTOS-06 are stable after five iterations, whereas 3DTH still reduced the RMS values with increasing iteration number. Whereas for code LOTOS-06 five iterations were sufficient, for code 3DTH more iterations were necessary. However, I performed up to 20 iterations using code 3DTH and compared the resulting images and RMS travel time residuals. Finally, I decided that the results obtained after nine iterations were reliable because only minor changes occurred with increasing iteration number.

Due to the different data quality of the signals emitted along the three seismic profiles, a differentiation of the RMS travel time residuals for each profile was interesting. Figure 5.13 illustrates the RMS travel time residuals for the rays emitted along each single profile separately. Comparing these values for nine iterations, one realizes that for profile P16 all tomographic calculations aim in RMS travel time residual values between 0.16 s and 0.21 s, for profile P18 between 0.19 s and 0.30 s and for profile P19 between 0.12 s and 0.19 s. Apparently, the data quality of profile P19 is highest, followed by profile P16. This was already evident while picking the first onsets at the onshore receiver stations: the first onsets were clearly to identify at receiver gathers of profile P19, but were sometimes very hard to identify at receiver gathers of profile P18. This had mainly two reasons: first of all, the offsets between shots fired along the coast parallel profile P19 and onshore receivers was much smaller and always in the same range compared to the offsets between emitted shots along the dip lines P16 and P18 and onshore receivers. Second, parts of profile P18 were shot with an airgun array consisting of only two 32 liter airguns, whereas profile P16 and P19 were shot with an array of three 32 liter airguns.



**Figure 5.12:** RMS travel time residuals of code 3DTH (solid line) and LOTOS-06 (dashed line) plotted against iteration number. All rays emitted along profile P16, P18 and P19 are taken into account. The left diagram shows the travel time residuals obtained with initial model A, the middle diagram with initial model B and diagram on the right residuals obtained with initial model C.



**Figure 5.13:** RMS travel time residuals of code 3DTH (solid line) and LOTOS-06 (dashed line) plotted against iteration number. The upper row shows the travel time residuals obtained from rays emitted along profile P16, the middle row from rays emitted along profile P18 and lower row residuals obtained from rays emitted along the coast parallel profile P19. The left diagram shows the travel time residuals obtained with initial model A, the middle diagram with initial model B and diagram on the right residuals obtained with initial model C.

## 5.6 Discussion and Conclusions

Acquiring active seismic, three-dimensional data is very useful to study crustal structures as we did within the MERAMEX- project. The used data set had a very high ray coverage in the central part of the study area and therefore provided reliable images of the crustal structures south of the volcanic arc in Central Java. Working with tomographic codes does not only require synthetic tests showing the resolution of the used seismic data set but also the used software packages have to be tested, especially if newly developed codes as code LOTOS-06 are used.

Summarizing, forward modelling of the OBH data in two-dimensions allows to construct the structure of the subducting oceanic and overriding plate. Unfortunately, 2D effects play a major role in modelling structures like the basement high at the intersection of profile P18 and P19. Another problem is the modeling of structures close to the coast along profile P16 and P18. The OBH data close to the coast can only be constraint by OBH stations located further south and leads to a lack in model control at profile ends. Hence, it is very important to use land receivers to model the northernmost OBH stations to constrain the layer thickness and seismic velocities close to the coast line if these stations are available and also recorded the shot data. In case of the MERAMEX project, the land receivers were not installed in a straight line continuing the offshore profiles. Hence, only few receivers could be used to elongate the profiles onshore Central Java because 2D effects had to be considered while modelling 3D structures. However, the two-dimensional forward models were very useful to construct the background models for the tomographic studies because if there are no information of seismic velocities in the study area available, global models have to be used as initial models resulting in more testing, higher iteration numbers and a higher computer time. Anyway, the forward models were also very useful in controlling the tomographic results.

Recapitulating, both tomographic codes resolve the same features (Figures 5.7 - 5.11), whereas code LOTOS-06 seems to provide slightly too high and code 3DTH too low velocities. Nevertheless, code LOTOS-06 has several advantages compared to 3DTH:

1. The file structure to be loaded prior to run the software package is in case of code LOTOS-06 relatively easy and fast to organize. This is much more complicated and time consuming in case of code 3DTH.

2. Code LOTOS-06 needs less iterations resulting in a much shorter computing time. Due to the used bending method of ray tracing and the LSQR method to solve the matrix, each iteration needs less computer time than in case of 3DTH.
3. Both codes need to be tested in regard of smoothing. One main difference in the smoothing algorithm is that 3DTH smoothes the three-dimensional cube whereas LOTOS-06 smoothes two-dimensional sections during the visualisation routines.
4. Unlike code 3DTH which applies a coarse 1 km grid, code LOTOS-06 uses a variable grid spacing dependent on the ray density. The used grid size is very important for the smoothing processes implemented in the codes. In case of code 3DTH the complete area is smoothed in an analogous manner, i.e. it is smoothed about a special number of grids. Whereas code LOTOS-06 uses a dense and much smaller grid spacing in areas with high ray density and larger grids in areas with low ray density. This incorporates the advantages that the smoothing algorithm is much more adjusted on the resolution of the data set and that highly resolved areas are less smoothed compared to areas with low ray coverage. This difference can explain discrepancies in the resulting images of the two codes.
5. Even with a rough one-dimensional model, code LOTOS-06 provides reliable results. Code 3DTH is more dependent on the structure of the initial model and therefore, the better the initial model the better the final tomographic model.
6. Code LOTOS-06 offers to process both active and passive seismic data and provides handy routines for synthetic testing.
7. In comparison with the forward models of the OBH data, which included not only first break travel time information, it is obvious that code LOTOS-06 manages better with the applied bending method to trace rays through the medium, the variable grid sizes and the onshore receiver array to construct the dip in the upper layers of the seismic profiles P16 and P18 if just rough one-dimensional initial models are used. In contrast, code 3DTH doesn't achieve the dip of the upper layers using one-dimensional initial models and hence needs detailed preliminary information included in a three-dimensional initial model.

Based on these results, the application of code LOTOS-06 is recommend, if a huge data set consisting of active and passive seismic data is available. Even if only active data were acquired, the faster option to obtain first results will be code LOTOS-06 instead of code 3DTH.

## 6. SEISMIC STRUCTURE OF CENTRAL JAVA

### 6.1 Introduction

The oceanic Indo-Australian plate subducts at a rate of 6-7 cm/yr beneath the Sunda plate (Tregoning et al. 1994). This convergent plate boundary dominates the tectonic, volcanic and mass transfer processes of Java, Indonesia, which is part of the active Sunda Arc (Figure 6.1). As is common for subduction zones, most earthquakes occur along the interface between the subducting and overriding plates and have thrust fault mechanisms. Occasionally, a ‘seismic gap’ may form, where there is comparatively little seismicity. Such a seismic gap exists in Central Java, as shown in Figure 6.2. The May 26, 2006 magnitude  $M_w=6.4$  earthquake (22:53:59 UTC) (Global CMT catalogue 2007) was not typical for subduction earthquakes in that it had a strike-slip mechanism, was located just on the border of a “seismic gap” zone (Figure 6.2), and had a shallow 10-to-20 km deep hypocenter (as shown in Figure 6.2, at this distance from the trench the typical depth of hypocenters is between a 100 and 200 km).

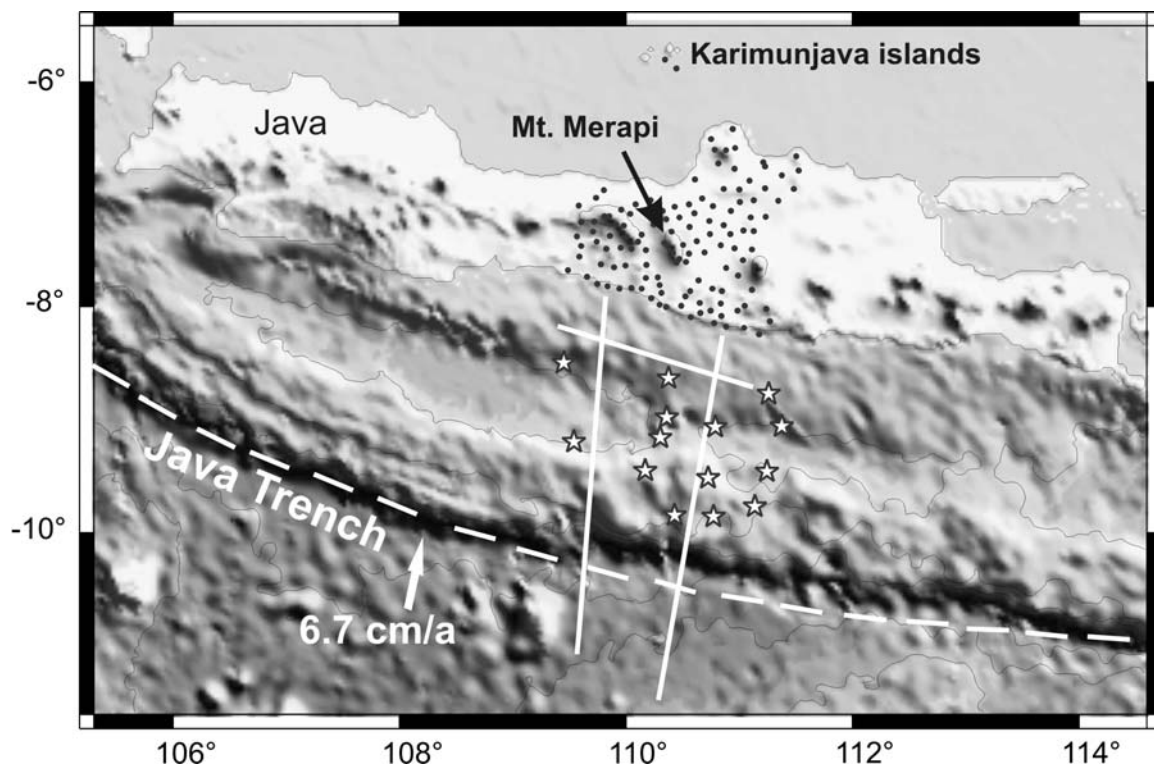


**Figure 6.1:** Shaded relief map of Java, Indonesia. The Indo-Australian plate subducts beneath the Sunda plate along the Java trench (dashed white line). Mt. Merapi is indicated. Black dots illustrate the temporary seismological network of the MERAMEX experiment. The network also included Ocean Bottom Hydrophones and Seismometers, marked by stars. The three white lines mark the wide-angle seismic profiles.

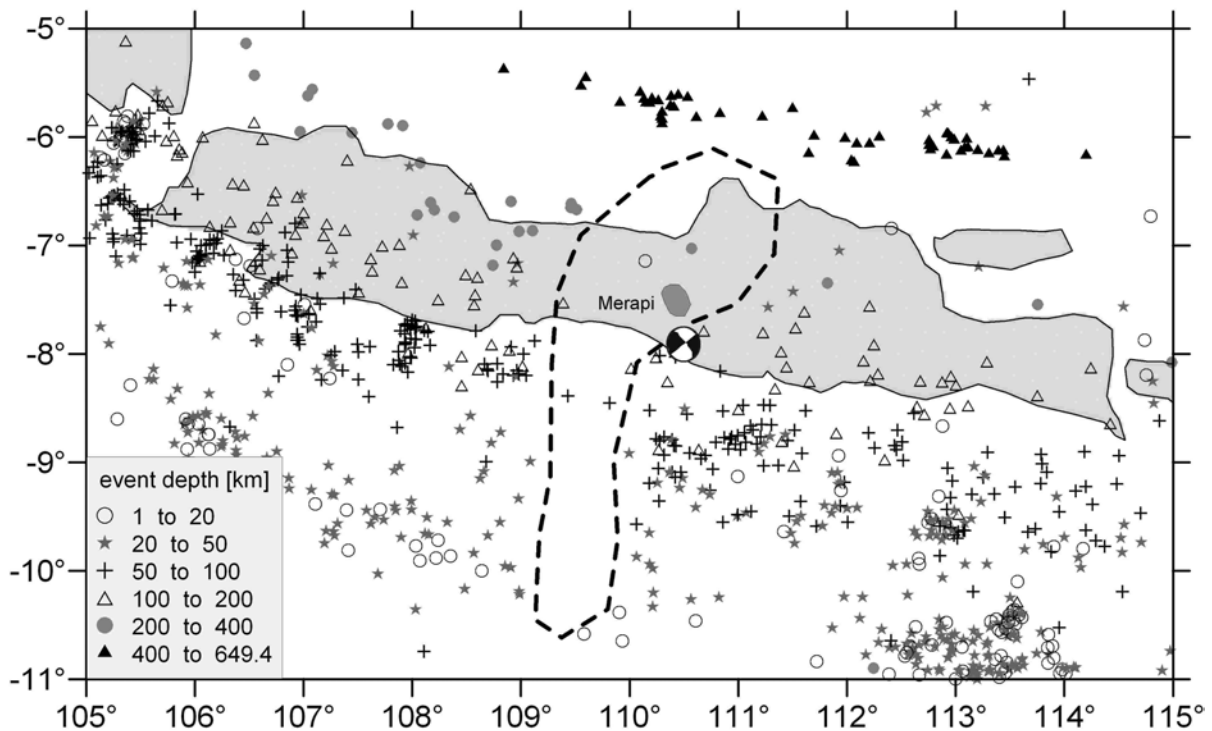


**Figure 6.2:** Epicenter distribution of earthquakes with  $M_w > 4$  recorded in Java between 1964 and 2001 (from ISC earthquake catalogue). Different symbols indicate the event depths. The moment tensor solution marks the Java event of May 26, 2006. The dashed line surrounds a zone in Central Java of relatively low seismic activity.

The May 26, 2006 earthquake caused extensive damages in the Bantul Valley, 20 to 50 km west of the epicenter, where there were more than 5,800 fatalities and 30,000 injuries, and where over 200,000 people were left homeless. The damage was largest in a strip between the coastline, close to the village of Parangtritis, and the village of Klaten located east of the city of Yogyakarta. The damage became less pronounced toward the Gunung Kidul mountain region, toward the epicenter, and was mainly due to the poor fabric of the newer buildings (remarkably, traditional houses endured the forces of the earthquake, whereas ‘modern’ brick houses were destroyed). The apparent lack of direct correlation between distance to the epicenter and intensity of damage can be explained by amplification of the seismic waves as they entered the alluvium-filled Bantul Valley (Figure 6.7), where Yogyakarta is located.

## 6.2 3D Tomographic Studies of Active Seismic Data

The active three-dimensional seismic data recorded with the onshore MERAMEX network resulted in 50060 first break travel time observations onshore. This data set was used for a tomographic determination of the seismic structure of the crust of Central Java. The forward modeling of the OBH data provided P-velocity information on the study region, which was used to generate a one-dimensional background velocity model for the tomographic studies (see Table 6.1) using the LOTOS-06 code (see Chapter 5). The results presented here were obtained after five iterative steps. The velocity perturbations shown in Figure 6.4 and 6.5 represent the differences between the calculated velocity model and the background velocity model in percent.

Thanks to the dense network of receiver stations, and the tight 150 m spacing of shot points, our results yielded a high ray coverage (Figure 5.6 and 6.3). Therefore, it was possible to image the earth's crust in the Central Java area up to a depth of about 20 km in high resolution using only the active seismic data (see synthetic tests in Chapter 5.3). The covered area extends 200 km in an east-west direction and 150 km in a north-south direction. To the north it is framed by the volcanic arc. Signal attenuation north of the volcanic arc- and at Merapi volcano itself- is very high: This results in reduced data quality and low ray coverage north of the arc regarding only active seismic data because the signal energy of the airguns was limited (Figure 4.4). Nevertheless, the data quality of the active seismic data is very high, given the maximum offsets of about 150 km between airgun shots and onshore receivers. In case of passive data, the area north of the volcanic arc is well-resolved because the local earthquakes provide signals with higher energy (Koulakov et al. 2007). The main features detected in the tomographic study are one high-velocity anomaly and three low-velocity anomalies (Figure 6.4a).

**Table 6.1:** 1D velocity model used as background velocity model for the tomographic studies.

Depth [km]	Vp [km/s]
-3	4.3
3	4.9
8	5.7
16	6.9
24	7.1

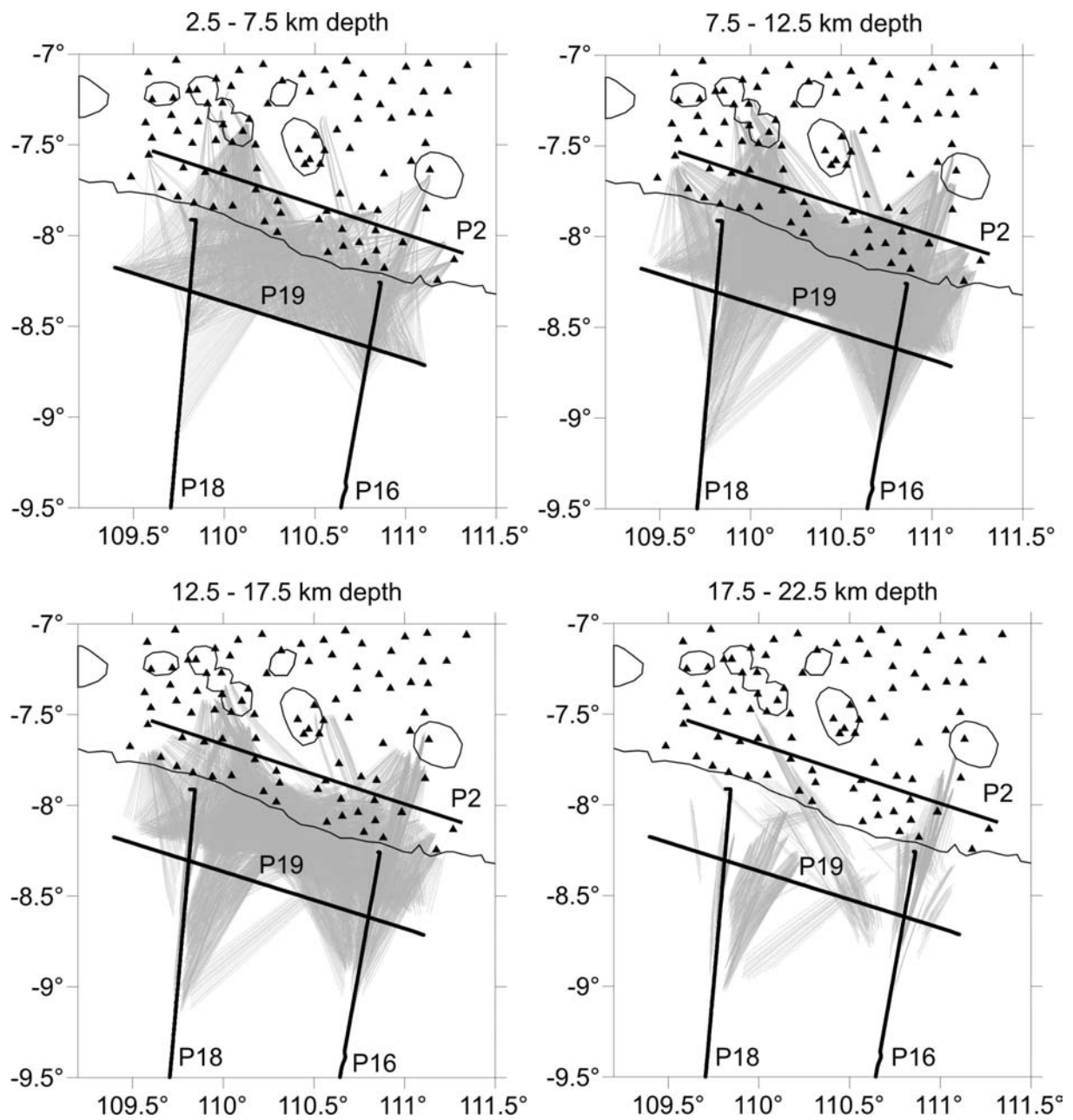


**Figure 6.3:** Rays paths of the active seismic data recorded in the onshore MERAMEX network presented in four horizontal sections at 5, 10, 15 and 20 km depth. One of ten ray paths traveling through a 5 km thick volume in whose center the shown horizontal section is located are plotted. The triangles correspond to the onshore receiver stations located within this area. The black lines mark the seismic profiles P16, P18 and P19.

1. High-velocity anomaly along the coast-parallel profile (HVZ-1, number 1 in Figure 6.4a and 6.5).

An east-west elongated, high-velocity anomaly (Figure 6.4, horizontal sections at 5, 7.5 and 10 km depth) is located around  $8.3^{\circ}$  S and  $109.9^{\circ}$  E at the intersection of the coast-parallel and the western profiles. Figure 4, profile 6, shows a vertical section through the center of this anomaly. The increased seismic velocities in this area- compared to the surrounding materials- are clearly visible in the side-by-side images that show velocity perturbations and absolute P-velocities. The positive anomaly, which is only visible in the upper crust up to 12.5 km depth, can be interpreted as a basement high. This feature is also clearly visible in the seismic wide-angle forward models of the OBH data.

2. Low-velocity anomaly along the western dip line (LVZ-2, number 2 in Figure 6.4a and 6.5).

The horizontal sections at 5 km depth (Figure 6.4a) shows a low-velocity anomaly, slightly elliptical in the north-south direction, located around  $8^{\circ}$  S and  $109.8^{\circ}$  E. This anomaly straddles the western profile, between the coastline and the coast-parallel profile. In the 7.5 to 12.5 km depth profiles the anomaly “rotates” and merges into a linear anomaly that parallels the coast. This is a shallow crustal feature, because size and amplitude of the negative anomaly decrease with increasing depth. The negative anomaly vanishes completely at 15 km depth (see also Figure 6.5, vertical sections 4 and 5).

3. Low-velocity anomaly along the footprint of the volcanic arc (LVZ-3, number 3 in Figure 6.4a and 6.5).

This is the largest anomaly detected in this study. The anomaly follows the band formed by the active volcanoes Sumbing, Merapi and Lawu, which are aligned WNW-ESE. As manifested by local earthquake tomographic studies of the MERAMEX network performed by Koulakov et al. (2007), the active seismic data described in this paper show just the southern edge of a larger low-velocity anomaly in the backarc crust. Additionally, a joint inversion of active and passive seismic data was performed using the advantages of both data sets (see Chapter 7). The joint inversion resulted in a detailed image of the low-velocity zone in the crust and upper mantle up to a depth of 50 km (Figure 6.4b). The volcanoes hence are located above the transition between a high-velocity forearc and a low-velocity backarc anomaly. The latter anomaly is exceptional as it shows a velocity

decrease of more than  $-30\%$  at 5 km depth. Below a depth of 15 km the negative anomaly increases in size and decreases in amplitude. Koulakov and coworkers ran a number of synthetic tests that verify our interpretation. This shows that the detected low-velocity anomaly in the tomographic studies of only active, only passive, and active and passive seismic data is reliable.

4. Low-velocity anomaly between the southern coastline and the volcanoes (LVZ-4, number 4 in Figure 6.4a and 6.5).

A narrow low-velocity zone is apparent south of the volcanic arc at  $7.9^\circ$  S and  $110.4^\circ$  E. This anomaly is up to 50 km elongated in NNE-SSW direction, and only few kilometers thick in E-W direction (horizontal section at 10 km depth in Figure 4a). To the west and to the east zones of a higher velocity can be found. The low-velocity anomaly therefore divides the rigid forearc into two blocks. The division can be seen in horizontal sections up to 15 km depth (Figure 6.4). Vertical sections crossing the low-velocity zone are illustrated in Figure 6.5. Profiles 1 and 2, located just south of Merapi volcano, most clearly illustrate the division of the forearc into two blocks. Profile 3 shows a gap in the low-velocity zone at a depth of about 7.5 km (see also Figure 6.4a, horizontal section at 7.5 km depth). Below 10 km depth (Profile 3 in Figure 6.5), the negative anomaly is very distinct, being in the order of  $\sim 5$ -10 km thick only. Profile 4 is located approximately on top of the coastline. This profile still shows some disturbances in the velocity model, but from this profile further south the low-velocity anomaly does not form a straight line any more and vanishes completely at profile 5. This anomaly, which separates two rigid blocks, is the location of one of the most prominent fault zones in the area (the Opak River fault, which trends  $N40^\circ$ E).

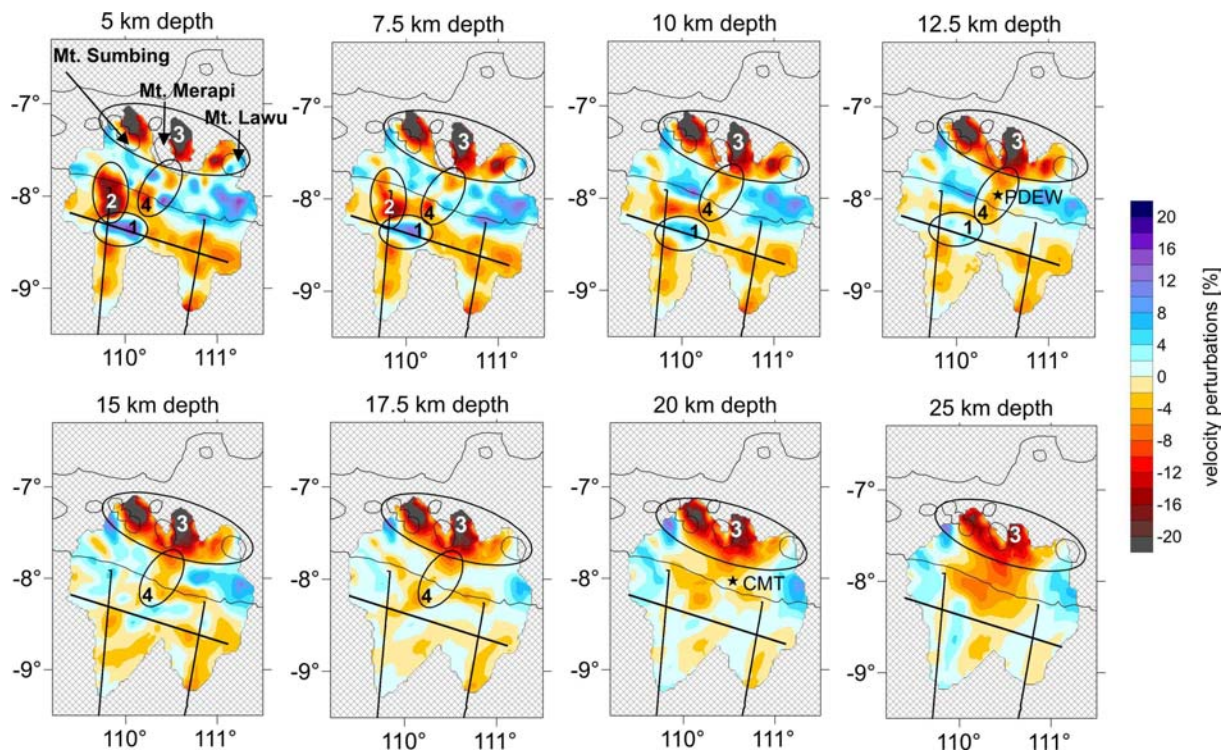


**Figure 6.4a:** Tomographic results of the active seismic data in horizontal sections showing velocity perturbations in percent with respect to the background velocity model. The three offshore lines mark the locations of the airgun profiles. The stars mark the epicenter locations of the event on May 26, 2006 (see Table 6.2).

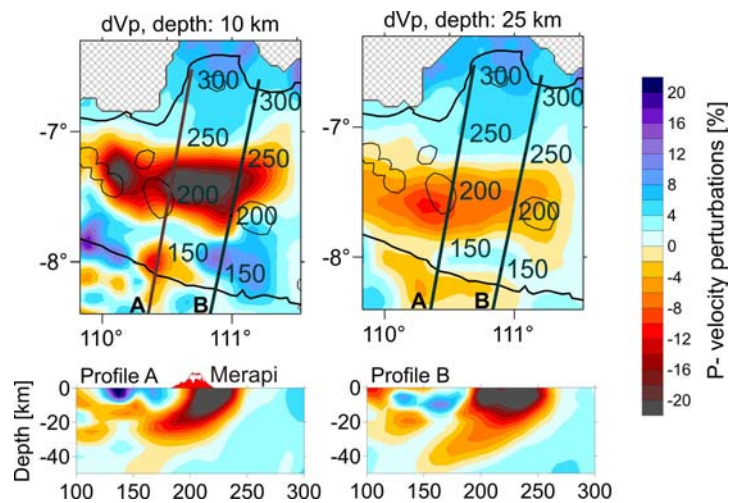


**Figure 6.4b:** Tomographic results obtained after the joint inversion of active and passive seismic data in two horizontal and two vertical sections showing velocity perturbations in percent.



### 6.3 The Java Earthquake and its Aftershocks

The 26<sup>th</sup> of May 2006 Mw=6.4 Java earthquake occurred in exactly the region of the MERAMEX study area, where the tomographic images of only active data show the highest ray coverage and accuracy. The Java earthquake was a disaster because it was shallow and the epicenter was located near a densely populated area of the district of Yogyakarta (3.5 million inhabitants). Estimates of the hypocenter location (Table 6.2) fall at the edge of the relatively narrow low-velocity zone LVZ-4, which is oriented in northeast-southwest direction as described above (Figures 6.4 and 6.5).

**Table 6.2:** Hypocenter definitions of the Java event of May 26, 2006 (Global CMT catalogue, 2007).

Solution	Date [YR:MO: DA]	Time [UTC] [HR:MN: SEC]	Latitude [deg]	Longitude [deg]	Depth [km]	Magnitude
PDEW- Preliminary Determination of Epicenter	2006/05/26	22:53:58.90	7.96°S	110.45°E	12.5 km	Ms=6.3
CMT- Centroid Moment Tensor solution	2006/05/26	22:54: 05.29	8.03°S	110.54°E	21.7	Mw=6.4

Three days after the event occurred in Central Java, four members of the German Task Force (TF) for Earthquakes arrived in Indonesia. The main aim of the German Task Force, which is coordinated by the GFZ Potsdam, is the acquisition of post-seismic data after large earthquakes to study the geologic and tectonic causes for the earthquake and its impact on the earth's surface and buildings. These records are used to determine precise aftershock hypocenters, and to try to determine the structure of the fault system and the orientation of the fault plane on which the main shock occurred. The Task Force installed a network consisting of 12 temporary seismological stations in the epicentral area of Bantul (Figures 6.6 and 6.7) and recorded the aftershock activity following the main shock for three months (between 5/31/2006 and 8/30/2006). Within the three month campaign, approximately 3000 earthquakes were recorded during the operation of the network. As is common for aftershocks, the maximum aftershock magnitude was Mw=5.0, slightly less than an order of magnitude less than the main shock. The locations of 282 aftershocks are shown in Figure 6.6 and 6.7. The standard deviation of the plotted events is 0.3° in longitude, 0.4° in latitude and

1 km in depth. The aftershock distribution shown in Figure 6.6 correlates well with the northeast-southwest oriented low-velocity zone LVZ-4 (described in the previous section), which is located between the southern coastline and the volcanoes. At 5 km depth, 10 % of the aftershocks accumulate in the gap and at the eastern edge of the low-velocity zone. Most aftershock events (61 %) are located between 7.5 km and 12.5 km depth, at the eastern boundary of the low-velocity zone. Hypocenter locations between 12.5 km and 17.5 km depth (27%) form a straight line in northeast-southwest direction. Figure 6.5 suggests that the main shock occurred most likely around 12.5 km depth (PDEW solution, Table 6.2).

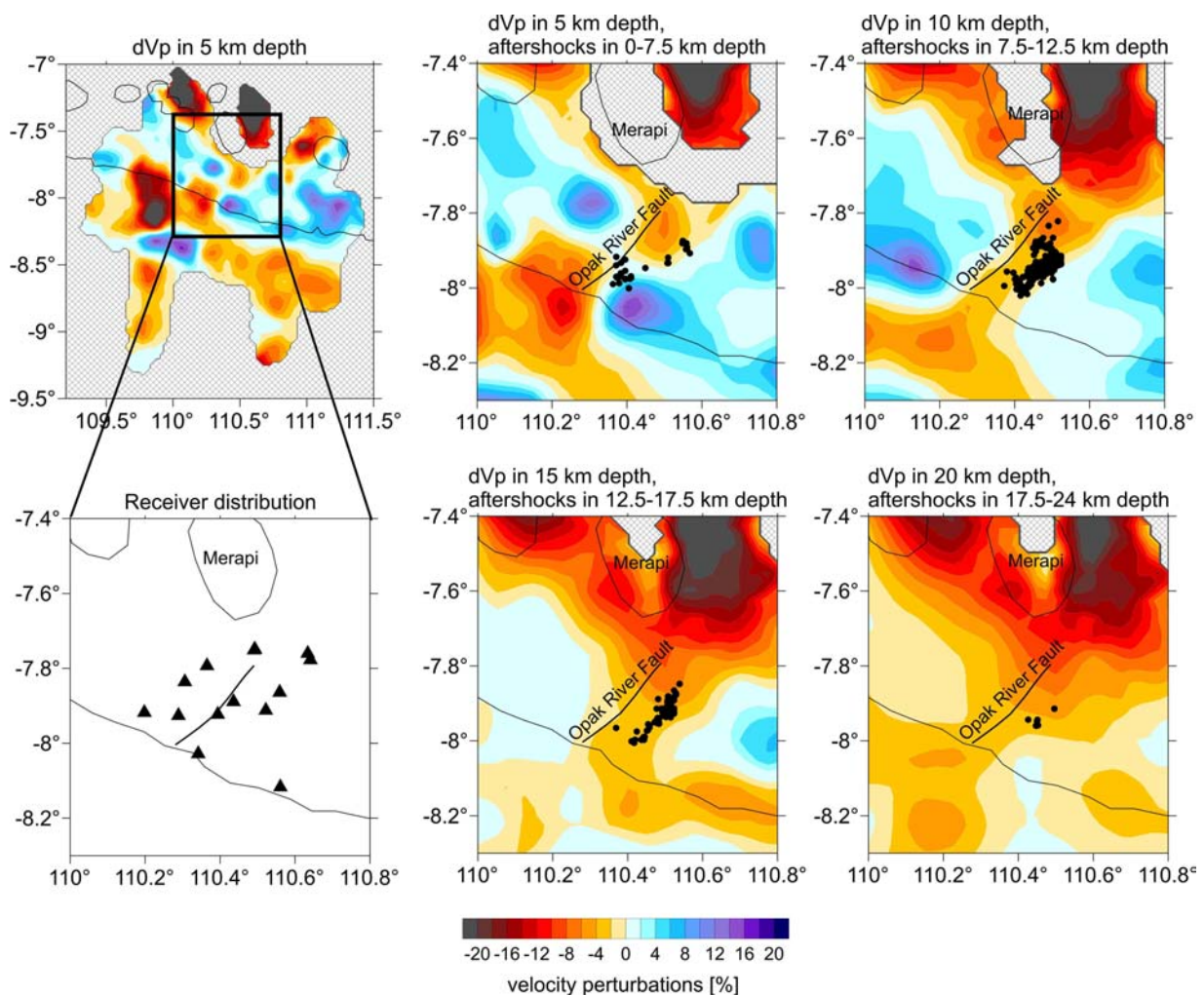


**Figure 6.6:** Zoomed tomographic images of the Bantul area. Triangles mark the network, black dots the aftershocks recorded in the given depth sections.

First assumptions made by many scientists had been that the Opak River fault was the source of the earthquake, because it is located parallel and close to the area of greater damage. However, the comparison of the aftershock distribution with the geological map (Figure 6.7) shows that the events are arranged semi-parallel to the Opak River fault, but trend N40°E (in contrast to the N30°E trend of the fault), and are located about 10-15 km to the east in the Gunung Kidul Mountains. This implies that the Opak River fault was not the main source of the May 26 earthquake. A fault trending closer to the northeast direction, and located further east than the Opak River fault, correlates much better with the moment tensor solutions.

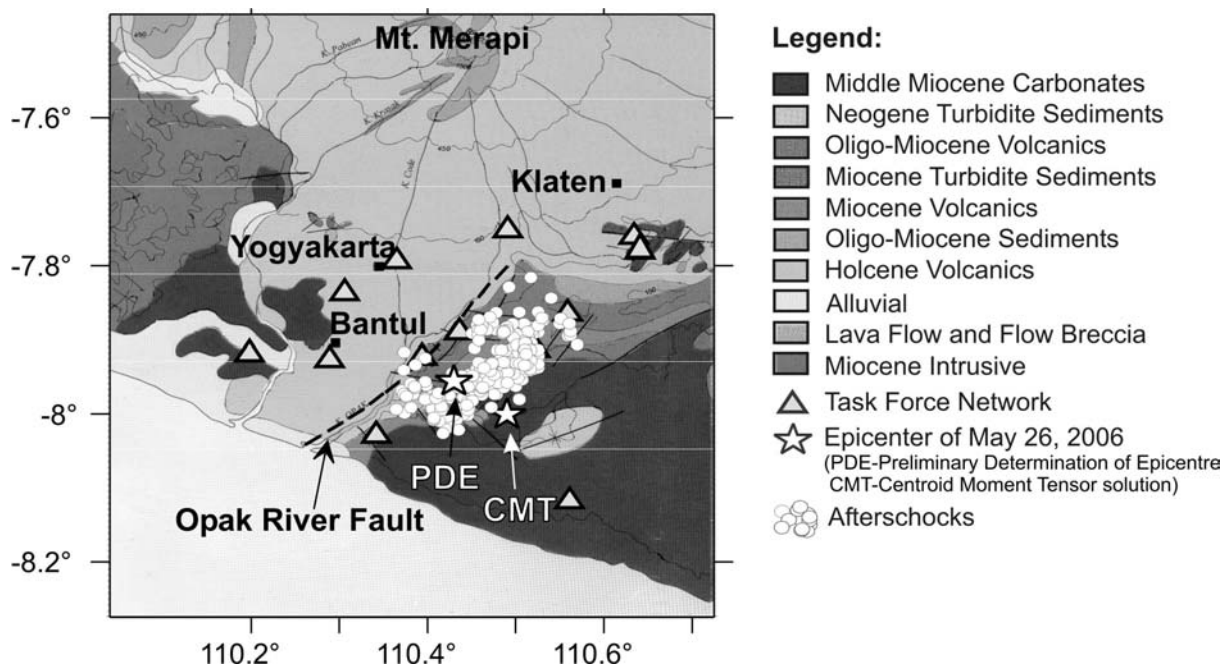


**Figure 6.7:** Geologic map showing the Bantul area in detail. (Geologic map is modified after *Peta Geologi Lembar Jawa Bagian Tengah, Geologic Map of Middle Part of Jawa*, by T.C. Amn, N. Ratman, Dan (and) S. Gafoer (1999).

## 6.4 Summary and Discussion

Seismic tomography is a powerful tool for imaging the earth's crust. The three-dimensional active seismic data recorded in the onshore MERAMEX network provide detailed images of the crust up to a depth of about 25 km. In comparison with passive data recorded in the same network, the active seismic data provide images of much greater detail, crucial to determine smaller features in the uppermost 20 km of the crust

Three main low-velocity zones and one high velocity zone were detected. One of the low-velocity zones (LVZ-3) is located just beneath the volcanoes Sumbing, Merapi and Lawu with a reduction in seismic velocities of over 30 % in the upper crust. This low-velocity anomaly coincides with a gravity low and extends to depths of more than 50 km to the upper mantle. The anomaly is interpreted to be the result of partially molten material in the crust beneath the volcanic systems of Central Java.

Another low-velocity zone (LVZ-4) has a northeast-southwest elongated geometry and divides the forearc into two blocks, a rigid block to the east and a rigid block to the west. The low-velocity zone dividing the forearc shows an accumulation of aftershocks and can be described as a weakened zone of the seismogenic crust. Zhao (2000) determined that most crustal earthquakes in Japan occur along the edges of low-velocity zones revealed by seismic tomography. Large crustal earthquakes occur in the edge portions of a low-velocity zone, instead of within them, because mechanical strength is higher in the edge portions than in the central part of a low-velocity zone, but the rocks are still weaker than in the undisturbed, rigid blocks surrounding a low-velocity zone. The event of May 26, 2006, and its aftershocks, occurred within the eastern edge portions of low-velocity zone LVZ-4, in close resemblance to the relationships documented by Zhao (2000) in Japan. We note that the May 26 earthquake had two distinctive characteristics: (1) devastation in the region of Bantul, 15 km distant from the fault plane, probably because of site-specific amplification effects, and (2) increased volcanic activity at Merapi volcano, where magma extrusion rates increased three-fold. The latter could be a coincidental effect, since the volcano had shown increased volcanic activity throughout May, and the earthquake did not take place until May 26.

Regarding the earthquake distribution of the ISC catalogue (Figure 6.2) it appears that there had not been any large seismic events in the area of Bantul within the last 40 years. This might explain why the local population in the district of Yogyakarta were not prepared for and were surprised by an event of magnitude  $M_w=6.4$  and its associated destruction. The aftershock distribution recorded in the network installed by the German Task Force has helped to understand the local tectonic framework, and may assist in future risk assessment. For one thing, the aftershocks were not located along the Opak River fault, as could be expected, but were located in the Gunung Kidul Mountains along a previously unrecognized fault zone.



## 7. JOINT INVERSION OF ACTIVE AND PASSIVE SEISMIC DATA

### 7.1 Introduction

Most of the damaging seismic and volcanic activity on the Earth is related to subduction zones. The recent destructive earthquake in Central Java (26.05.2006 UTC), which coincided with increased activity of Merapi volcano, is a dramatic illustration of close links between the subduction and surface tectonic activity. To understand the mechanisms which link the process of the sinking oceanic lithosphere to concurrent tectonic activity, seismicity and volcanism, it is important to obtain reliable information about the structure of the plate boundary volume involved: the shape of the slab, the 3D structure of the crust and mantle wedge, and the distribution of seismicity. Seismic tomography is one of the most powerful tools to obtain these constraints.

The focus of this study is on the investigation of Central Java, a 200 km wide segment of the Sunda Arc, which extends from the Bay of Bengal and the Andaman Sea, along Sumatra and Java eastwards to Sumba Island (Figure 7.1). The deep-sea trench marks the boundary between the Indo-Australian plate and Eurasia where oceanic lithosphere is subducted beneath the Sunda Arc with a convergence rate of  $6.7 \pm 0.7$  cm/yr in front of Java being approximately orthogonal to the trench (Tregoning et al. 1994) (Figure 7.1). Along the Sunda Arc, the plate margin system and the subduction style vary significantly. The margin changes from oceanic–continental off Sumatra, to transitional off Java and intra-oceanic off Bali and Flores (Hamilton 1988). Kopp et al. (2005) determined that the subduction style is dominated by an accretionary regime along the western Sunda margin whereas along the Central Java margin an erosive regime exists. The subduction of oceanic basement relief including the RooRise, an oceanic plateau, causes a retreat of the Java deformation front between  $109^{\circ}\text{E}$  and  $115^{\circ}\text{E}$  northward by approximately 50–60 km from its normal curvature trend (Figure 7.1). Off Central Java a continuous accretionary wedge, an outer forearc high and forearc basin are not developed as recognized along the Sunda margin off Sumatra and West Java (Figure 7.1). Off western Java and southern Sumatra 96 Ma old oceanic crust subducts, while crustal ages increase to 135 Ma off eastern Java (Moore et al. 1980; Masson 1991). The subduction process along the active Sunda Arc is characterized by strong volcanism and high earthquake activity (Kennett et al. 2005; Mignan et al. 2006). More than one hundred active volcanoes are located along the Sunda Arc, including Tambora and Krakatau. Their eruptions in 1815

and 1883 are known as two of the strongest and most destructive volcanic events in historical time. The distribution of seismicity from the worldwide catalogue (*ISC 2001*) illustrates that off the south coast of Java, the dipping angle of the slab increases gradually from almost horizontal to very steep ( $70^{\circ}$ - $80^{\circ}$ ) north of Java. Beneath the Karimunjawa island group in the Java Sea, some moderate seismicity at a depth of around 600 km is observed.

Our study region includes Merapi volcano, which is the most active volcano in Java and represents a tremendous hazard to the local population. Mt. Merapi is a strato volcano showing evidence of explosive eruptions over the last 7000 years (Newhall et al. 2000). However, the volcanism at Mt. Merapi began much earlier (Berthommier 1990; Camus et al. 2000). Most previous geophysical studies in Central Java focused on the internal structure of Mt. Merapi (Müller & Haak 2004; Müller et al. 2002; Wegler & Lühr 2001; Maercklin et al. 2000). Seismological studies carried out by Ratdomopurbo & Poupinet (2000) show an aseismic zone situated between two seismic zones at a depth between 1.5 km and 2.5 km below the summit. They postulate that this aseismic zone is caused by a small shallow magma reservoir temporarily storing injected magma from a deeper reservoir located below 5 km depth. Based on GPS and tilt data modeling, Beauducel & Cornet (1999) suggest a deep magma reservoir located some 6 km below sea level. The upper magma reservoir proposed by Ratdomopurbo & Poupinet (2000) could not be detected by Beauducel & Cornet (1999), but their results do not preclude the “two reservoir” idea because the studies were carried out at different times. High resolution gravity modeling conducted by Tiede et al. (2005) shows high-density bodies beneath the volcanic summits of Mt. Merapi, Mt. Merbabu and Mt. Telemoyo, which may be interpreted as magma reservoirs.

On May 26, 2006 at 22:54:01 UTC a strong magnitude  $M_w=6.3$  earthquake (source: NEIC & Harvard) occurred in Central Java, Indonesia about 25 km SSE of Yogyakarta (May 27 at 5:54 AM local time in Java, Indonesia) and caused more than 6000 fatalities. BGR (Federal Institute for Geosciences and Natural Resources) placed the hypocenter at a depth of 17 km, which implies that the earthquake occurred in the overriding Sunda plate well above the dipping Australian plate. Moment tensor solutions show a strike slip regime. However, it is not clear why this event displays a strike-slip mechanism, while the effect of the slab pushing should primarily cause compression in the forearc crust. Based on the results obtained in this study, an explanation for this fact will be proposed.

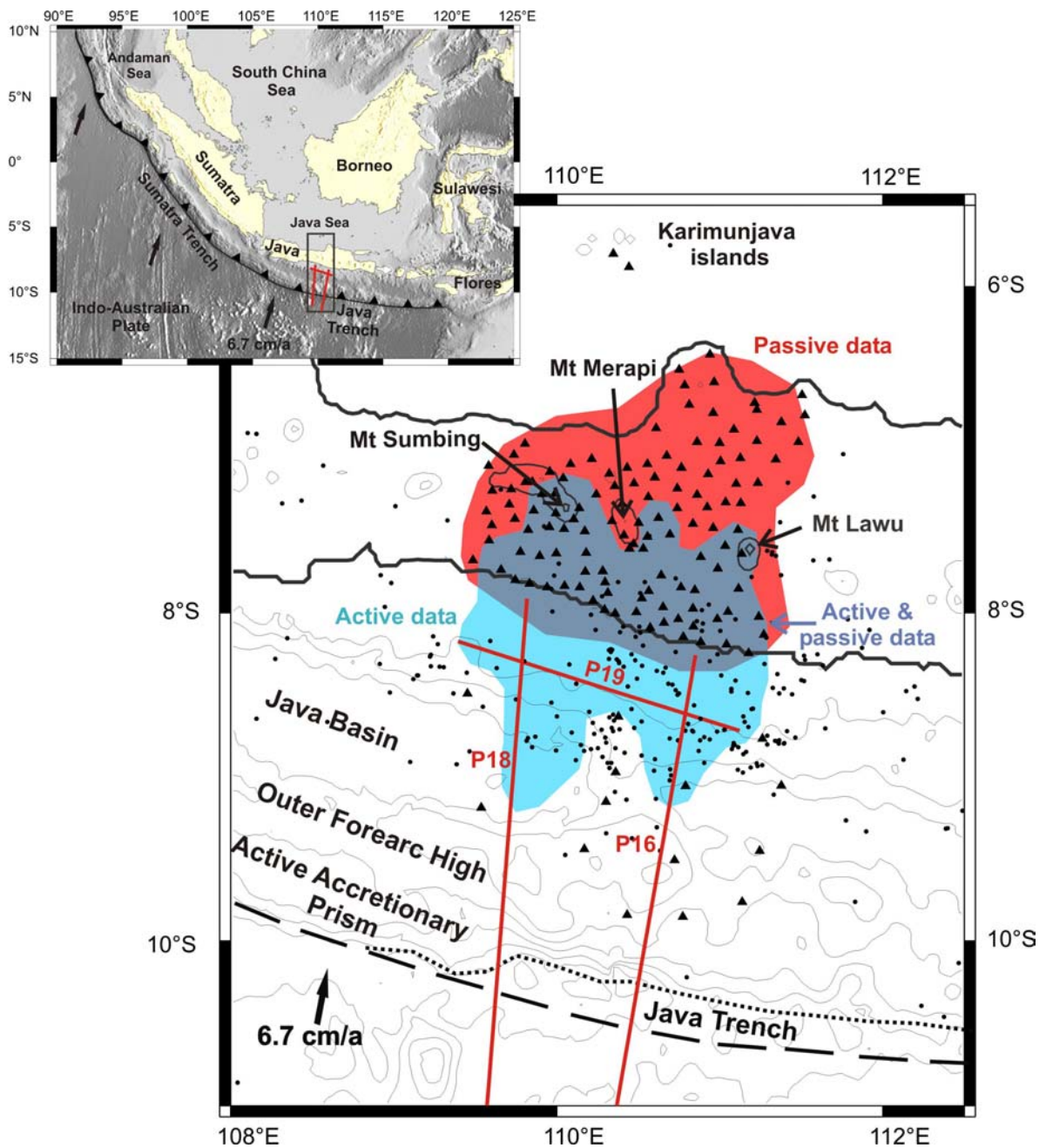


**Figure 7.1:** Upper diagram: Bathymetric map of the Sunda Arc. The Indo-Australian plate is subducted beneath the Eurasian plate along the Sumatra and Java trench. The location of our study area is marked by the box. Lower diagram: Study area including the tectonic regime of the region. The triangles mark the temporary seismological network. Dots are recorded earthquakes collected in the MERAMEX catalogue. Red lines indicate the seismic airgun profiles. The red coloured area in Central Java marks the area which is covered by the passive data, the light blue area is covered by active seismic data, while the grey area is covered by both data sets, respectively in the uppermost 10 km depth layer. They are identified as areas with satisfactory recovery of 30 km size checkerboard anomalies at a depth of 5 km (Section Synthetic Tests, Figure 6.5). The dotted line marks the current track of the trench, which is retreating northward from the normal curvature trend (dashed line) in front of Central Java.

In 2004, combined amphibious seismological investigations at 110°E were performed in the framework of the MERAMEX (MERapi AMphibious EXperiment) project to study a volcanic arc system as part of an active continental margin. More than 100 seismic stations operated continuously for more than 150 days (see details in the data section). The local seismicity data recorded at these stations were used to perform a local tomographic inversion (Koulakov et al. 2007c). This study provided important information:

- the presence of a large low-velocity anomaly in the crust northward of the active volcanoes showing a high  $V_p/V_s$  ratio of 1.9.
- a low-velocity anomaly in the upper mantle, which is inclined towards the slab.
- the existence of a double seismic zone in the slab at 40-130 km depth with a dipping angle of about 45°.
- the shape of the slab in the Benioff zone, which is almost horizontal for the first 150 km away from the trench and then gradually increases to about 70° at 250 km depth.

Based on the results mentioned above, a mechanism of feeding the volcanoes in Central Java was proposed. Koulakov et al. (2007) checked successfully the reliability of the most important features retrieved from the inversion of only passive data in the crust and upper mantle in a number of synthetic tests. In one test they defined a strong shallow anomaly (more than 30% of amplitude and 0-5 km of depth interval) representing the Merapi-Lawu-anomaly, northward of the active volcanoes, to understand whether the observed low-velocity anomaly in the crust is an artifact due to some near-surface factors or whether it may be attributed to deep crustal structure. The results of this test showed that although the effect of downward smearing of a shallow anomaly is quite important, the images of the real data inversion cannot be obtained merely due to an effect of near surface anomalies. It shows that the crust in the Merapi-Lawu anomaly area consists of low-velocity material in all depth intervals, not only near the surface.

During the operation of the MERAMEX network, three-dimensional active seismic experiments were carried out offshore south of Central Java during RV Sonne cruise SO179. Airgun shots were fired along three profiles and recorded by ocean bottom stations. The seismic reflection and refraction data acquired along these profiles were forward modeled in two dimensions using a ray-tracing method to obtain the deep structure of the main interfaces in the offshore part and the P- wave velocity field (Chapter 4). Simultaneously, the signals from the airgun shots were recorded at onshore MERAMEX stations providing the unique

opportunity to combine passive and active data for the same network. In this study, the passive data set used in Koulakov et al. (2007) is updated with the active source data that gives us some important advantages compared to the previous study: e.g. the enlargement of the resolution area (Figure 7.1) and the improvement of the model reliability and resolution because of significantly higher accuracy of the active data. One shortcoming of the passive data is that due to the trade-off between velocity and source locations, absolute velocities cannot be retrieved reliably. The active data yields constraints to fix the P-velocity distribution in the uppermost 20 km onshore and offshore. In particular, it was crucial for obtaining reliable crustal structure information around the recent Java earthquake (26.05.2006) to provide an explanation of its mechanism.

## 7.2 The Algorithm

The data processing is performed using an updated version of code LOTOS-06 (Local Tomographic Software), which is described in detail in Koulakov et al. (2007) and allows processing for active and passive seismic data simultaneously. The reference 1D model (Table 7.1) was parameterized by points at fixed depths and interpolated linearly in between. Down to a depth of 20 km, the P-velocity distribution was estimated based on the forward modeling results of the OBH data acquired within the MERAMEX project. For deeper parts, the P-velocity distribution was defined based on the global AK135 model (Kennett et al. 1995). For the S-velocity distribution, a-priori information was not at hand and was determined using a fixed  $V_p/V_s$  ratio of 1.78, which provided the minimum RMS values after the first location step. Although this ratio is important for the source location, it has no significant effect on the relative velocity variations in the tomographic inversion, as shown in Koulakov et al. (2006b & c).

**Table 7.1:** 1D velocity model.

Depth [km]	$V_p$ [km/s]
-3	4.3
3	4.9
8	5.7
16	6.9
24	7.1

The iterative inversion algorithm consists of the following steps:

**Step 1.** Computation of the reference travel time table. Approximate locations of natural sources in a 1D velocity model are determined using a 3D grid searching algorithm, based on the determination of an absolute extreme of a goal function (Koulakov & Sobolev 2006b). The extreme of the goal function is determined by searching the station with the minimum residual.

**Step 2.** In case of passive data the coordinates and travel times and in case of active data only the travel times are corrected according to a location algorithm, which maximizes the goal function following the direction of maximum gradient, similar to Koulakov et al. (2006a). This algorithm is designed for an arbitrary 3D model and is based on the bending method of ray tracing (Um & Thurber 1987).

**Step 3.** A parameterization grid is defined according to ray density. The nodes are placed in vertical planes spaced at 10 km from each other. The ray density defines the distribution of the nodes in each vertical plane and hence, in areas containing a small amount of rays, the distance between nodes is larger. The minimum spacing between nodes is fixed at 5 km to prevent extreme node concentrations in areas of high ray density. Due to effects and artifacts caused by a predefined grid orientation, the inversion is conducted in four differently oriented grids ( $0^\circ$ ,  $45^\circ$ ,  $90^\circ$  and  $135^\circ$ ) and then stacked. The 3D velocity anomalies are computed at nodes distributed in the study volume. The nodes are joined together into tetrahedral blocks. Between nodes inside the tetrahedrons, the velocity distribution is interpolated linearly. The resolution of the model is controlled by smoothing and regularization parameters.

**Step 4.** The matrix construction is based on the computed ray paths. The residuals representing the effect of velocity variation in each node on the travel time of each ray ( $\partial t / \partial V$ ) are computed by integration along the ray paths (Koulakov et al. 2007). For the passive data, the matrix also includes the elements for source parameter corrections. To control the smoothing of the 3D velocity models, a specific matrix block is added to the calculated matrix. Each line in this block contains two non-zero elements with opposite signs, corresponding to neighboring parameterization nodes in the model. The corresponding data vector for this block is zero. Increasing weight of these elements have a smoothing effect upon the resulting anomalies. In this study, the estimation of the parameters for the inversion (smoothing, regularization and number of iterations) are based on results of synthetic tests with realistic anomalies and noise levels (Section Synthetic Tests).

**Step 5.** The matrix inversion using a LSQR method is performed simultaneously for P- and S-velocity values, parameters of natural sources (four parameters for each source) and P- and S- station corrections (Koulakov et al. 2007). As a result, the velocity anomalies are computed on a 3D irregular grid, which is subsequently interpolated to a regular grid. For the next iteration the velocity anomalies are added to the initial velocity model. Iterations are repeated until the contribution of the next cycle becomes negligible. In case of our study, five iterations were enough to achieve sufficient convergence.

## 7.3 Results

### 7.3.1 Active Data Inversion

Active data picks amounted to a total of 50060. However, since the shot spacing was significantly smaller than the size of retrieved anomalies, it makes no sense to use the entire data set. In this case, the rays from close shots would produce almost identical equations, which would not improve the resolution of the tomographic model. Therefore, only one of two picks is used for the final inversion. In the cases of the entire and reduced data sets, the inversion yielded very similar results. However, due to the lack of space, results of this comparison are not presented here.

The resulting distribution of P-velocity anomalies after the inversion of only active data is shown in Figure 7.2 in horizontal sections (upper row). The RMS values of the residuals in five iterations are presented in Table 7.2. The value in iteration 1 resulted from ray tracing in the 1D starting model. Velocity perturbations are only shown if the distance to the nearest parameterization node is less than 10 km. Since the nodes were placed according to the ray density and distributed only in areas with sufficient ray coverage, results are only plotted in well-resolved parts of the investigated volume.

**Table 7.2:** RMS values of the residuals after five inversion iterations for only active data.

Iteration	Active P RMS [s]
1	0.4047983
2	0.2229798
3	0.1697343
4	0.1509526
5	0.1404346

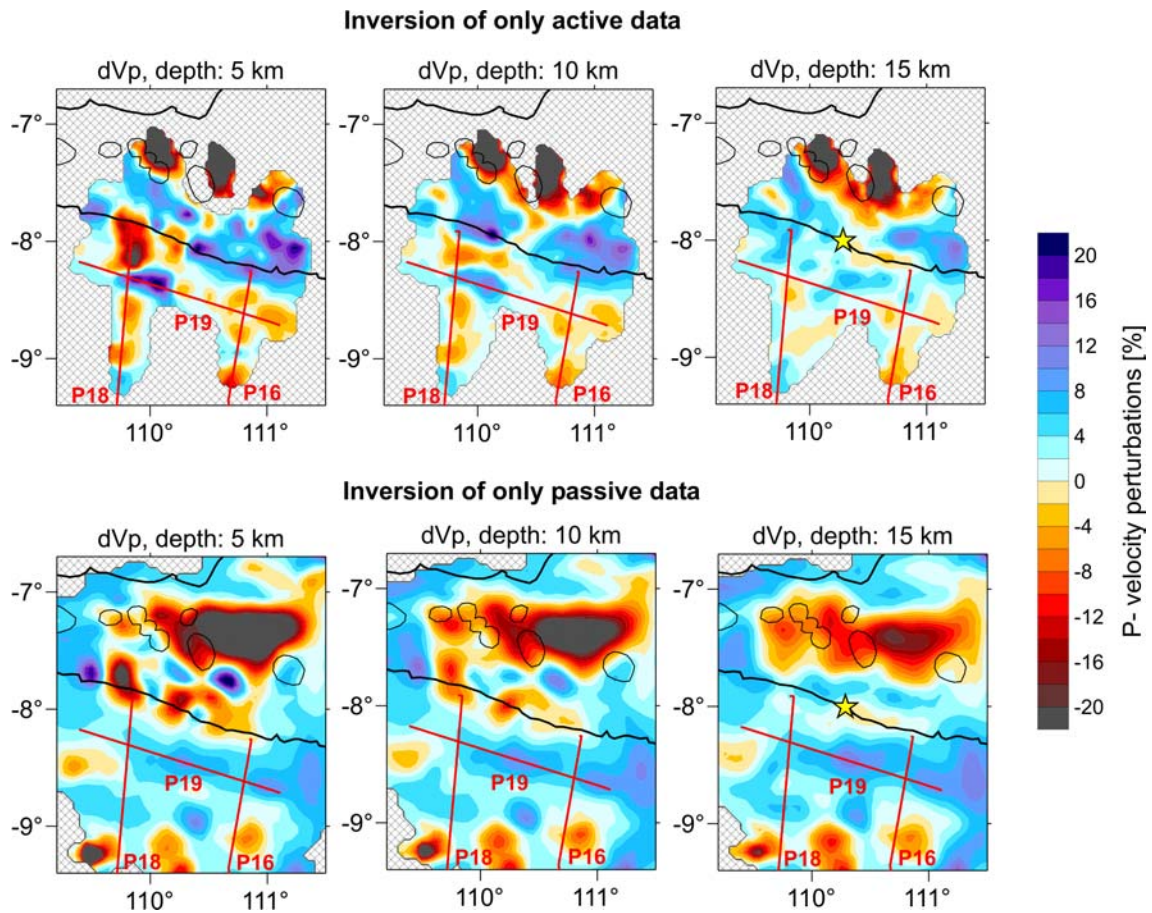


**Figure 7.2:** P-velocity anomalies after inversion of only active and only passive seismic data presented in horizontal sections at 5, 10 and 15 km depth. The black lines are the coastline and volcanoes located in Central Java. The airgun profiles are plotted with red lines.

Sumbing, Merapi and Lawu volcanoes are located above a very sharp boundary between a high-velocity forearc and a very strong negative anomaly northward of the volcanoes. This negative anomaly is called MLA- (Merapi-Lawu anomaly) hereafter. Although it occurs near the edge of the resolved area, this feature seems to be fairly robust. The forearc in these images appears to be strongly heterogeneous due to the complex geological structure of this area. South of Merapi, in the onshore part, an elongated zone of relatively low velocities is recognized. It is noteworthy that the hypocenter of the last strong earthquake event (26.05.2006 UTC), indicated by a yellow star in Figure 7.2, is located exactly in this zone. In the offshore part, the dominant feature is a high-velocity pattern at the intersection of seismic profiles P18 and P19 resolved at 5 km depth. It extends to the east along the coast parallel to profile P19, as is also clearly visible in the seismic wide-angle forward models of these profiles (Wittwer et. al., in prep.).

### 7.3.2 Passive Data Inversion

The passive data comprise the information from the 292 clearest local events detected during the operational period of the network. In total, 13800 phases (8000 P- and 5800 S-phases) were handpicked and used for the simultaneous location of sources and tomographic inversion. The lower row in Figure 7.2 shows the P-velocity perturbations obtained after the inversion of passive data (Koulakov et al. 2007c). The most prominent feature is the strong low-velocity anomaly MLA, with over 30 % amplitude for the P-velocity in the crust. The volcanoes (Sumbing, Merapi and Lawu) are located just above the edge of the contact zone between the MLA and the highly heterogeneous forearc. The RMS values of the residuals of the five inversion iterations are given in Table 7.3. It can be seen that the variance reduction after the final inversion is relatively small, about 35.4 % for P data. The remaining residuals could be caused by random noise in the data. Koulakov et al. (2007c) performed a test in which the data set was divided and inverted independently, obtaining the same image which shows that random noise does not play a significant role. Therefore, the explanation of the residuals may be related to some real features not taken into account by our model. For example, it might be that strong small velocity patterns, which cannot be resolved by our model, still have an effect on travel times. In the zone of active volcanism, there could be relatively small magma pockets (up to 1 km) in the crust and uppermost mantle. Another explanation might be related to anisotropy, which can be quite important but is not taken into account in our study.

In general, the results obtained using independent passive and active data correlate fairly well (Figure 7.2). The most prominent negative anomaly MLA just north of the volcanoes is clearly observable in both models. The shape of the interface between MLA and the forearc is similar. In the uppermost parts of the forearc (5 and 10 km depth), the difference in velocity structures appears to be quite significant. It might be due to the different resolution of the passive and active seismic data sets. Shifting the colour scale achieves a better resemblance of the images. At a depth of 15 km, the images of both models are very similar.

*Table 7.3: RMS values of the residuals after five inversion iterations for the passive data.*

<b>Iteration</b>	<b>Passive P RMS [s]</b>	<b>Passive S RMS [s]</b>
1	0.4464233	0.7856368
2	0.3447699	0.5819924
3	0.3133518	0.5314015
4	0.2977030	0.5073152
5	0.2883759	0.4923005

### 7.3.3 Inversion of the Combined Active and Passive Data Sets

The data used for the generation of the two models described in the previous sections were combined and inverted for a joint model. The weighting of corresponding rows in the general matrix controlled the contribution of the active data in the joint inversion. The same effect can be achieved by selecting a larger amount of active data, i.e. more than 50 %. However, this approach requires more computer time. In summary, the P-velocity model in the horizontal sections as shown in Figure 7.3 is essentially a mixture of active and passive models controlled by weighting of the active data set. In our case greater weight was given to the active data because they are less noisy and the offsets between source and receiver, as well as travel times of rays are well known compared to passive data.

It should be noted that although an inversion for P and S models with passive data was performed, only the P-velocity model is presented here. RMS values of the residuals are given in Table 7.4 separately for P rays in the active data, and P and S rays in the passive seismic data. The S model in this inversion remained almost unchanged both in images and RMS values. Theoretically, P and S models are linked through source parameters, which are inverted simultaneously. However, in practice, the effect of P-velocity variation on the S model is fairly small. The distribution of earthquake hypocenters recorded in the MERAMEX network relocated after five iterations in the joint inversion model remained unchanged with respect to the solely passive inversion model (Koulakov et al. 2007).

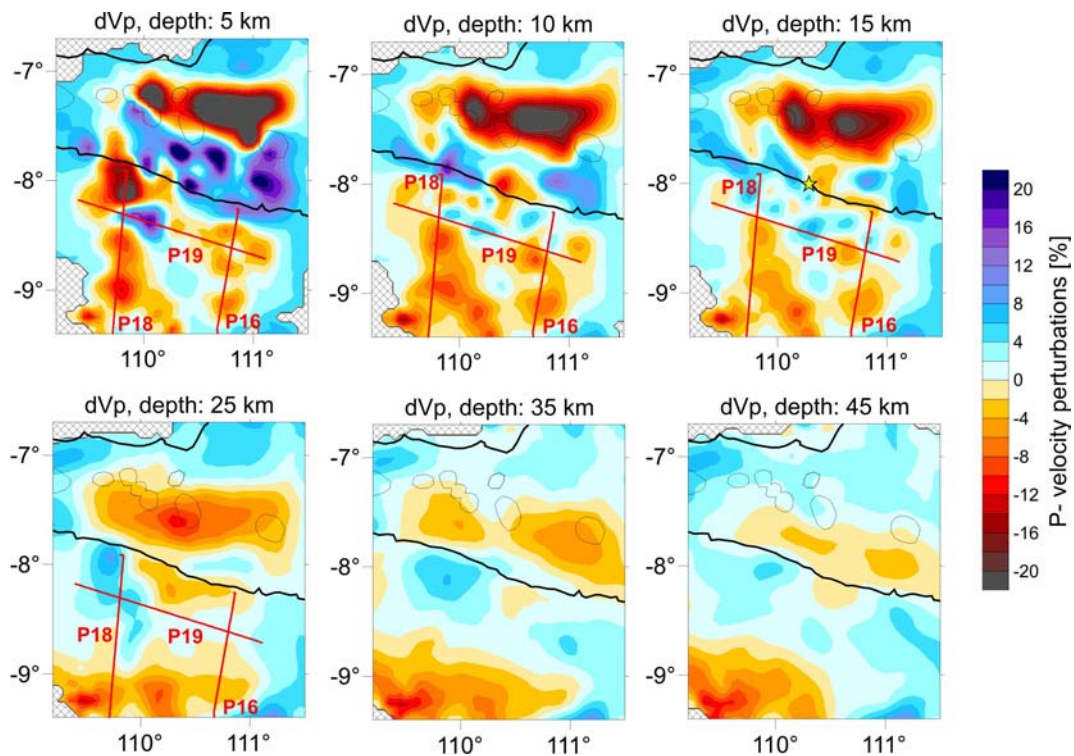


**Figure 7.3:** *P*-velocity anomalies after the joint inversion of the active and passive data sets presented in horizontal sections. Red lines indicate the airgun profiles. The star in the panel for 15 km represents the hypocenter location of the Java earthquake in May 2006.

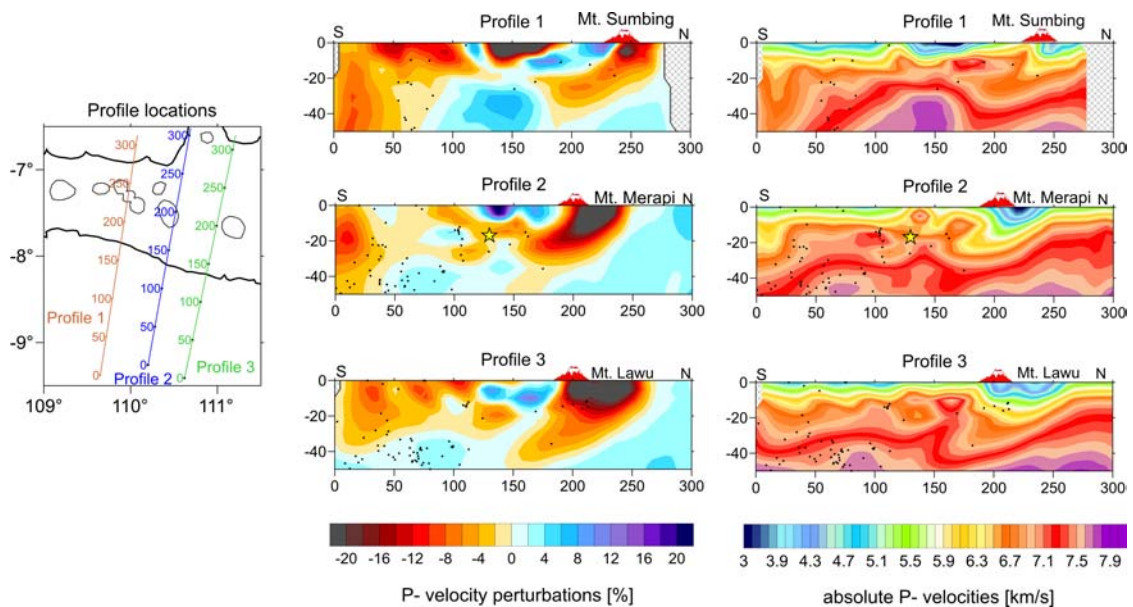


**Figure 7.4:** Result of the joint inversion for the *P*-velocity model presented in vertical sections. Profile locations are shown in the map on the left. The middle column presents relative perturbations of *P*-velocity; plots on the right show absolute velocities. Black dots mark hypocenters of the MERAMEX catalogue, the star in profile 2 marks the hypocenter of the Java earthquake in May 2006.

**Table 7.4:** RMS values of the residuals after five iterations for the joint inversion. RMS values for active and passive P- velocities and passive S- velocities are shown.

Iteration	Active P RMS [s]	Passive P RMS [s]	Passive S RMS [s]
1	0.4047983	0.4464233	0.7856368
2	0.2381959	0.3433573	0.5795938
3	0.1948432	0.3149615	0.5304253
4	0.1784572	0.3008182	0.5062090
5	0.1705896	0.2933580	0.4931750

The vertical sections in Figure 7.4 show that the MLA extends into the upper mantle and is inclined towards the slab. The amplitude of the MLA changes from east to west as can be seen in the vertical sections (Figure 7.4). Below Merapi and Lawu volcanoes (Profile 1 & 2, Figure 7.4) the amplitude of the anomaly is much larger than beneath Sumbing volcano (Profile 3, Figure 7.4). In the forearc, the crust shows inhomogeneous characteristics. Several low-velocity anomalies can be identified whose shapes are inclined towards the trench and coincide with the distribution of local seismicity. The correlation of seismicity and low-velocity anomaly is highest south of Merapi, Profile 2. The hypocenter of the Java earthquake, 26.05.2006, is located in the transition zone of these anomalies. A more detailed description of the anomalies and their interpretation are given below in the ‘Discussion and conclusions’ section.

## 7.4 Synthetic Tests

Synthetic testing is one of the most important steps in any tomographic investigation to verify the results. The non-uniqueness of the results of any seismic tomography, especially of one with natural sources with unknown coordinates, requires that the model is validated carefully. The solution appears to be uncertain with regards to absolute amplitudes and the shape of anomalies. In addition, the trade-off between the velocity structure and source parameters has to be taken into account. The most difficult problem of tomographic analyses is to prove that the resulting images have some relevance to the structures in the real earth. In case of correct application, synthetic testing is able to provide reliable estimates for true amplitudes of the retrieved anomalies (Koulakov et al. 2007) to give us an idea about true resolution provided by the observation system and to separate true features from artifacts.

Our algorithm for synthetic modeling allows the definition of various synthetic models either as periodical anomalies in a checkerboard test or manually by drawing various shapes

in vertical or horizontal sections. The travel times for the synthetic test are computed by 3D ray tracing in a synthetic velocity model using real source-receiver pairs. In addition, random noise  $\varepsilon$  is added to the travel times. Usually, the shape of the noise is defined according to a histogram of the residual distribution in the real data set. The synthetic times computed in this way are then used as input for the whole inversion procedure, including Step 1 (absolute source location) for the passive data. The values of all free parameters for the reconstruction of the synthetic model are the same as those used for the real data inversion.

To evaluate the resolving capabilities of the model in different parts of the study area, a checkerboard test is performed. The initial synthetic model was defined in the whole area as periodical anomalies of 30 km in size. The amplitude of velocity contrast was set to  $\pm 7\%$ . In this test, 0.15 s RMS random noise was added to the data set. The results of this test are presented in Figure 7.5 separately for the active, passive and combined data sets for the depths of 5 km and 15 km. For deeper sections, the resolution is controlled by passive data only, and the results are the same as those shown in Koulakov et al. (2007). Figure 7.5 shows that the passive data cannot provide any resolution in the offshore part of the investigated area above 5 km depth. Adding the active data significantly extends the resolved area southwards and improves the accuracy and quality of the retrieved model, due mainly to the known positions of sources.

## **7.5 Discussion and Conclusions**

The seismic reflection and refraction data acquired along the offshore profiles P16, P18 and P19 during RV Sonne cruise SO179 were forward modeled to obtain the P wave velocity field and trend of the main interfaces in the offshore area including the subduction zone. Three independent two-dimensional models of each seismic profile were developed and subsequently merged. It is possible to compare the offshore anomalies obtained by seismic tomography with the two-dimensional models of the forward modeling. The forward and tomography models show a high degree of correlation. In particular, the high-velocity anomaly in the west at the crossing point of profiles P18 and P19 (Figure 7.2 & 7.3) corresponds to a basement high, which can also be detected in the bathymetry data. It correlates with increased velocities in this area in the 2D models of the two modeled seismic profiles. The anomaly vanishes at a depth of about 10 km, which is apparent in both tomographic and forward modeling results.

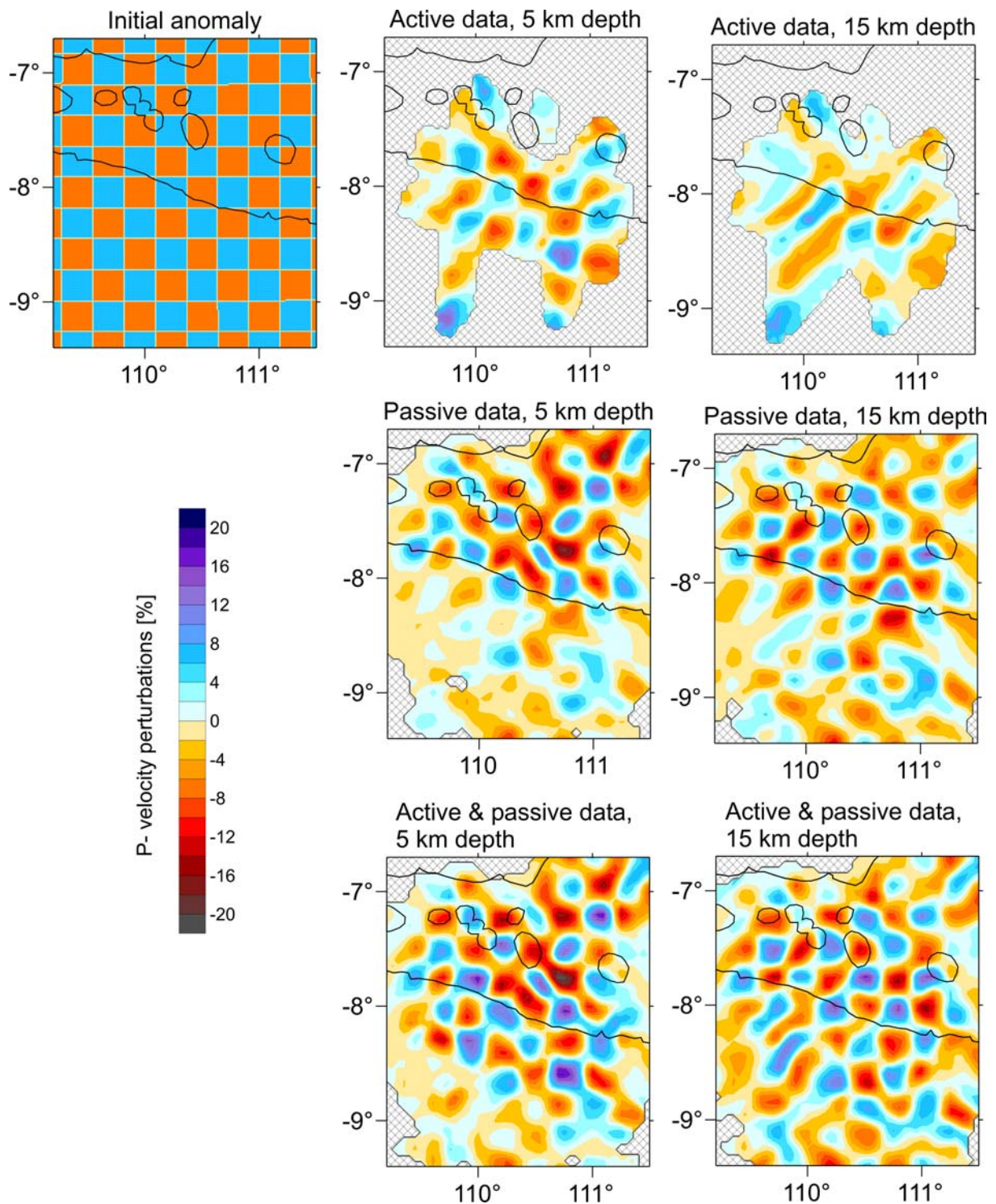


**Figure 7.5:** Comparison of the checkerboard tests for active, passive and combined data sets. The upper left image is the initial shape of anomalies with amplitudes of  $\pm 7\%$ . Noise of  $0.15\text{ s}$  RMS was added to the data in all cases. The 1<sup>st</sup>, 2<sup>nd</sup>, and 3<sup>rd</sup> rows show results of reconstruction for the active, passive and combined data sets. Here, the results at two depths are presented: 5 km and 15 km.

Thanks to the active three-dimensional data the reliability of the tomographic models in the uppermost 20 km depth in the forearc region was significantly improved. In particular, the uppermost crust in the new model in the onshore part consists of two high-velocity blocks. The contact zone is marked by an elongated low-velocity zone of slightly oblique orientation with respect to the southern coast (Figure 7.6). The epicenter of the Java earthquake (26.05.2006) is located just at the edge of this zone. This low-velocity zone is interpreted as a weakened area between two rigid forearc blocks (see horizontal section showing the active data in Figure 7.2). The decrease in velocity in this zone might be due to the fracturing of rocks in the uppermost crust. In the lower sections, at 15 km depth, this zone is almost invisible. The earthquake hypocenter is located just below this level (~17 km depth). This implies that it is located in the rigid crust, just below the weakened zone, that is the most probable location for stress accumulation and rupture (see Figure 7.6). The focal mechanism shows that the fault plane is oriented in the same direction as the weakened low-velocity zone. Figure 7.6 shows a zoomed-in horizontal section of the joint inversion at 15 km depth and two vertical cross sections through the earthquake epicenter. The epicenter in the vertical section CD (Figure 7.6) falls into a high-velocity layer, which is located just above the inclined contact zone between the high-velocity forearc and the low-velocity anomaly (MLA) northward of the volcanoes. The vertical section AB shows the epicenter well above the low-velocity anomaly.

An explanation for the origin of seismicity in the forearc on a larger scale is presented in Figure 7.7. The distribution of the seismicity in the Benioff zone indicates a variable dipping angle of the slab. For the first 150 km from the trench, the slab appears to be almost horizontal and then the dipping angle increases rather sharply to 45°. This change might cause a northward pushing and stress accumulation in the overriding plate. The observed local seismicity in the forearc including the Java event of 26.05.2006 can be due to this mechanism. The inclined linear anomalies in the forearc might reflect the distribution of weakened fracture zones, which are also observed in the active OBH data. The model in Figure 6.7 also relates the active volcanism in Central Java to the subduction processes. Earthquakes in the Benioff zone at a depth of about 100 km are related to a phase transition in the slab causing fluid release and partial melting of the oceanic crust. The melting temperature in the mantle wedge is reduced by the ascending fluids. Above 60 km depth an inclined low-velocity anomaly can be detected in the tomographic sections and it may be attributed to partial melt-

ing. The ascending fluids rise further upwards, get blocked by the rigid tectonic bodies of the forearc and move on northwards along the bottom of the forearc (see Figure 7.7). After the ascending fluids and melts have reached the northern boundary of the forearc, they form high concentrations of gases and magma and cause active volcanism.

Smyth et al. (2005) divide eastern Java into four east-west oriented zones 1) the southern Mountain zone, 2) the present-day volcanic arc, 3) the Kendeng zone and 4) the Rembang zone. The Kendeng zone represents a basin, which extends about 400 km in the east-west and about 100-120 km in the north-south direction and contains more than eight kilometers of sediments (Untung and Sato, 1978; Smyth et al. 2005). Bouguer gravity maps of Central Java (Untung & Sato 1978; Smith & Sandwell 1997; Smyth et al. 2005) show a strong negative Bouguer anomaly located in this zone, exceeding  $-580 \mu\text{ms}^{-2}$ . The gravity low presents a high correlation in size and location with the low-velocity anomaly MLA discussed above. While previous studies interpreted the basin as a rift, Smyth et al. (2005) propose no crustal thinning. They suggest that flexural loading of the crust by the volcanic chain contributed to the subsidence in this region. Waltham et al. (2006) forward modeled the gravity data. They needed a high density volcanic arc to model the gravity low accurately and propose that there are additional buried loads, which could be due to magmatic underplating.

The MLA has its maximum amplitude of over 30 % at 5 km depth and decreases with depth (see Figure 7.3 & 7.4). Hence, the exceptionally high amplitudes of the low-velocity anomaly in the uppermost 10 km is related to and partly caused by thick lava and sedimentary deposits in the Kendeng zone. But these deposits cannot explain why the MLA can also be detected in deeper depth sections and even in the mantle. In addition, these deposits alone cannot prevent magma penetrating to the surface and cannot explain the gravity anomaly completely. For the fact that any volcanism is observed above the MLA and the additional loads for the gravity modeling a possible explanation was suggested in a personal communication with V. Troll (2006). It was proposed that the material in the MLA is actually at a stage of cooling, which resulted in producing a rigid matrix filled with pockets of molten materials. As a result, this zone should be fairly rigid and of low-velocity. Thus, the fluids and melts from the mantle wedge cannot pass through and follow the bottom boundary of the MLA. The fluids and melts follow the shortest way towards the contact zone between the MLA and the forearc, where the active volcanoes are located. Only small amounts of fluids, which form mud volcanoes in the Kendeng zone pass through the matrix of sedimentary deposits and magma pockets.

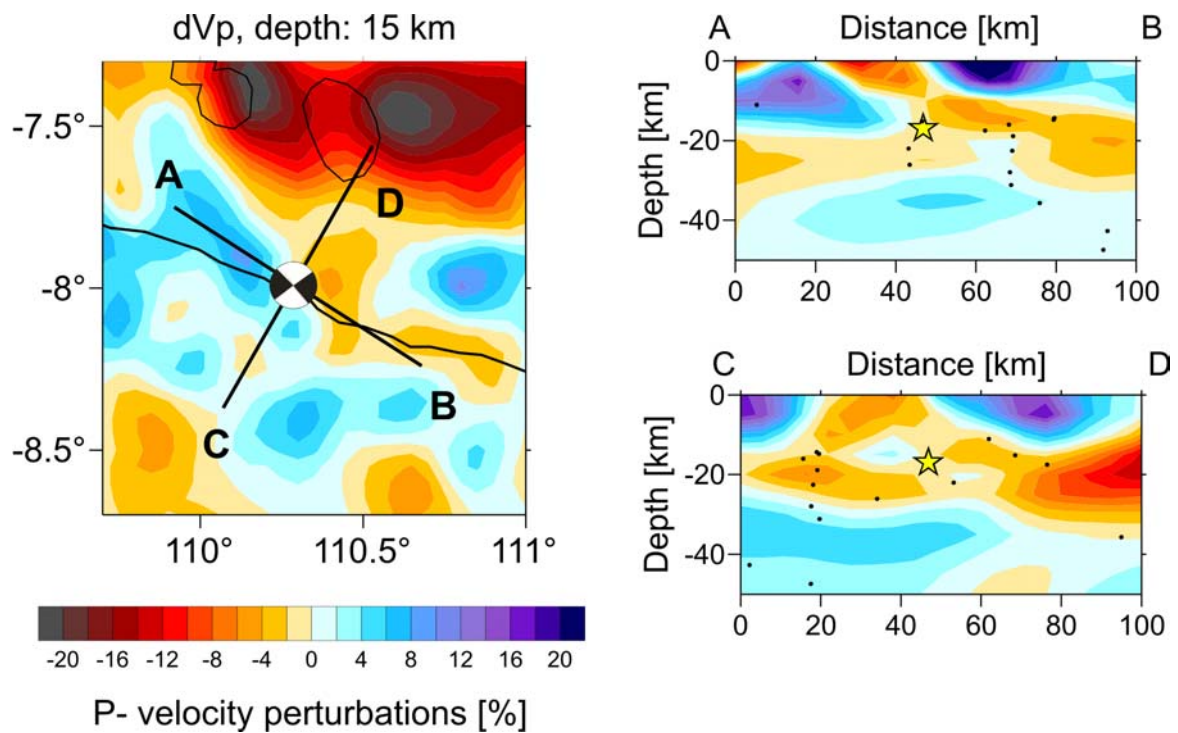


**Figure 7.6:** The left diagram shows a zoomed-in horizontal section of the joint inversion at 10 km depth. The two black lines indicate the positions of vertical sections crossing the BGR hypocenter of the Java earthquake in May 2006. Black dots mark earthquake hypocenters of the MERAMEX catalogue.

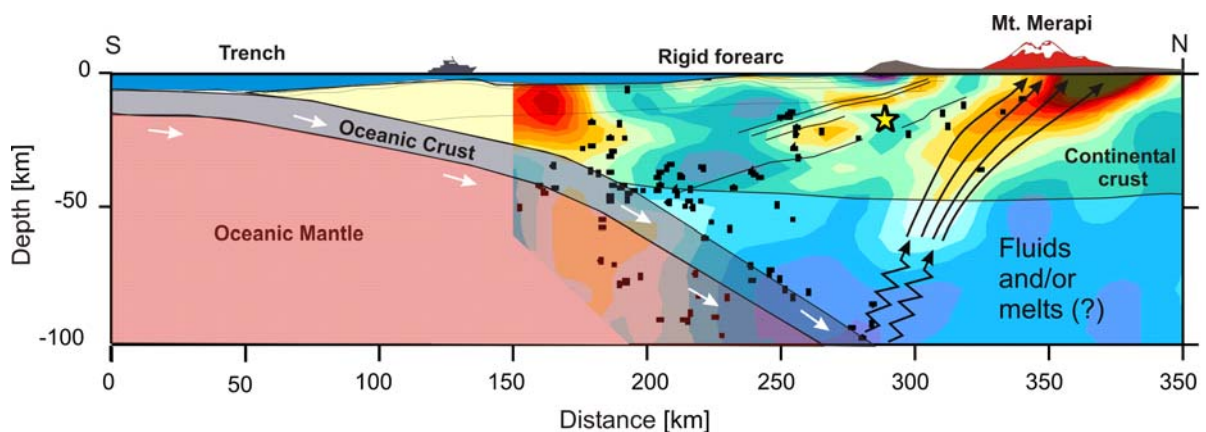


**Figure 7.7:** Sketch and interpretation of the velocity structure in Central Java. The oceanic plate pushes northward and subducts under Java. Partial melting occurs at a depth of about 100 km. Fluids and melts are ascending, thereby feeding the volcanoes located at the edge of the low-velocity anomaly. Stresses accumulate in the forearc region where fractures occur. Black dots show the earthquake distribution of the MERAMEX catalogue. The weakened low-velocity zone in the forearc correlates with the earthquake locations. The yellow star marks the BGR hypocenter of the Java earthquake in May 2006.



## **8. GEOPHYSICAL AND GEOCHEMICAL INSIGHTS INTO FORMATION OF A LARGE MAGMATIC SYSTEM IN CENTRAL JAVA, INDONESIA**

### **8.1 Introduction**

Catastrophic caldera forming (CCF) eruptions, from so-called super volcanoes, may erupt huge volumes of magma, up to 5000 km<sup>3</sup>, in a single event and are typically associated with subduction zones (Jellinek & DePaolo 2003). Extensive work has been carried out to characterise the near surface structure and eruptive products of these large volcanic centres, however, limited work has been devoted to investigating their pre-eruptive origin. The last super-eruption occurred at Toba caldera, Sumatra, Indonesia ~74,000 years ago (Bindeman 2006). Hence, these features are studied long after formation, restricting investigation to numerical modeling and reconstruction. In order to look at the origin of large caldera systems, it is integral to look at volcanic arcs where thermal “pre-conditioning” of the crust is likely to occur. By combining 3D seismic tomography with petrochemical data, we have identified a large body with significant partial melt present in the crust of Central Java, Indonesia and potentially, a supervolcano in the making.

Using seismic tomography, large low-velocity zones have been identified in the crust and upper mantle beneath active large volcanic systems. Low-velocity anomalies with a high ratio of P- to S-wave velocity ( $V_p/V_s$ ) beneath the Taupo volcanic zone, New Zealand, denote the presence of partial melt in the crust (Harrison & White 2004). Tomography, seismicity and gravity analyses of Toba caldera, the largest Quaternary caldera on Earth (Masturyono et al. 2001), identified a strong, shallow, negative anomaly with reductions in seismic velocities of up to 37 % in the upper 10 km of crust and continuity of lower velocities to the upper mantle. This anomaly and a corresponding gravity-low, are thought to be formed by partially-molten material in a large volume-crustal system with mantle roots (Masturyono et al. 2001).

## 8.2 Results

Three-dimensional tomographic studies from active and passive seismic data collected in the MERapi AMphibiuos EXperiments (MERAMEX) in 2004 (Koulakov et al. 2007; Wagner et al. 2007), have identified a large, low-velocity anomaly in the crust and upper mantle of Central Java, analogous to those seen beneath well-documented caldera systems. Seismic signals, emitted from a marine airgun source and from local earthquakes, were recorded with a network covering Central Java (Figure 8.1a). Airgun shots fired along three offshore profiles (Figure 8.1a) provided 50060 first break travel time observations onshore. The passive data consists of 13800 arrival times of P- and S- waves from 292 local earthquakes.

The identified P ( $V_p$ ) and S ( $V_s$ ) wave velocity anomalies show a reduction in seismic velocities of  $> 30\%$  and are largely located in the Kendeng basin just north of the active Sumbing, Merapi and Lawu volcanoes (Figure 8.1b). The Kendeng basin is the main Cenozoic depocentre for the region (Smyth et al. 2005). It contains between 8 km (de Genevraye & Samuel 1972) and 11 km (Untung & Sato 1978) of sediment and overlies a basement of uncertain composition, referred to as immature, arc crust, extending approximately 25 km below the surface (Jarrard 1986; Curray 1977; Van Bemmelen 1949). The velocity anomaly is elliptical and has a diameter of  $\sim 80$  km east-west and 30 km north-south (Figure 8.1b). The size and amplitude of this anomaly decreases with depth, yet it is still evident in the upper mantle down to 50 km. It is inclined towards the slab and has an elevated  $V_p/V_s$  ratio of 1.9 (Koulakov et al. 2007) relative to the crustal average of 1.7. The  $V_p$  and  $V_s$  anomalies are highly correlated with the largest amplitudes of the anomaly located between Merapi and Lawu volcanoes. Synthetic tests were successfully performed to check the reliability of these anomalies (Koulakov et al. 2007; Wagner et al. 2007).

Given the significant seismic velocity anomaly, its extent to the upper mantle and its location in the back-arc of the long-lived and highly active Sunda arc, this anomaly is regarded as an expression of a large melt system in the crust and upper mantle of Central Java. The strong low-velocity anomaly and the elevated  $V_p/V_s$  ratio are indicators for an unusually high fluid content. An average reduction of 20% in  $V_p$  combined with the observed 9% increase in  $V_p/V_s$  corresponds to a melt fraction of 13 - 25% in situ. This estimate is based on an effective elastic moduli model of composite rocks (Berryman 1995), assuming melt is present as randomly oriented elongate pockets with a bulk modulus of  $\sim 24$  GPa, typical of silicate melts (Webb & Courtial 1996). The lower estimate of 13% melt includes a weakening of the host rock matrix by intense fracturing. The upper 25% estimate

applies to unfractured host rock (Rabbel et al. 2004) and is below the critical melt fraction of 30 – 35 % above which, the shear strength of partially melted rock is expected to approach zero (van der Molen & Paterson 1979). The occurrence of earthquakes within the low velocity zone indicates that a melt volume between our estimated percentages is most likely.

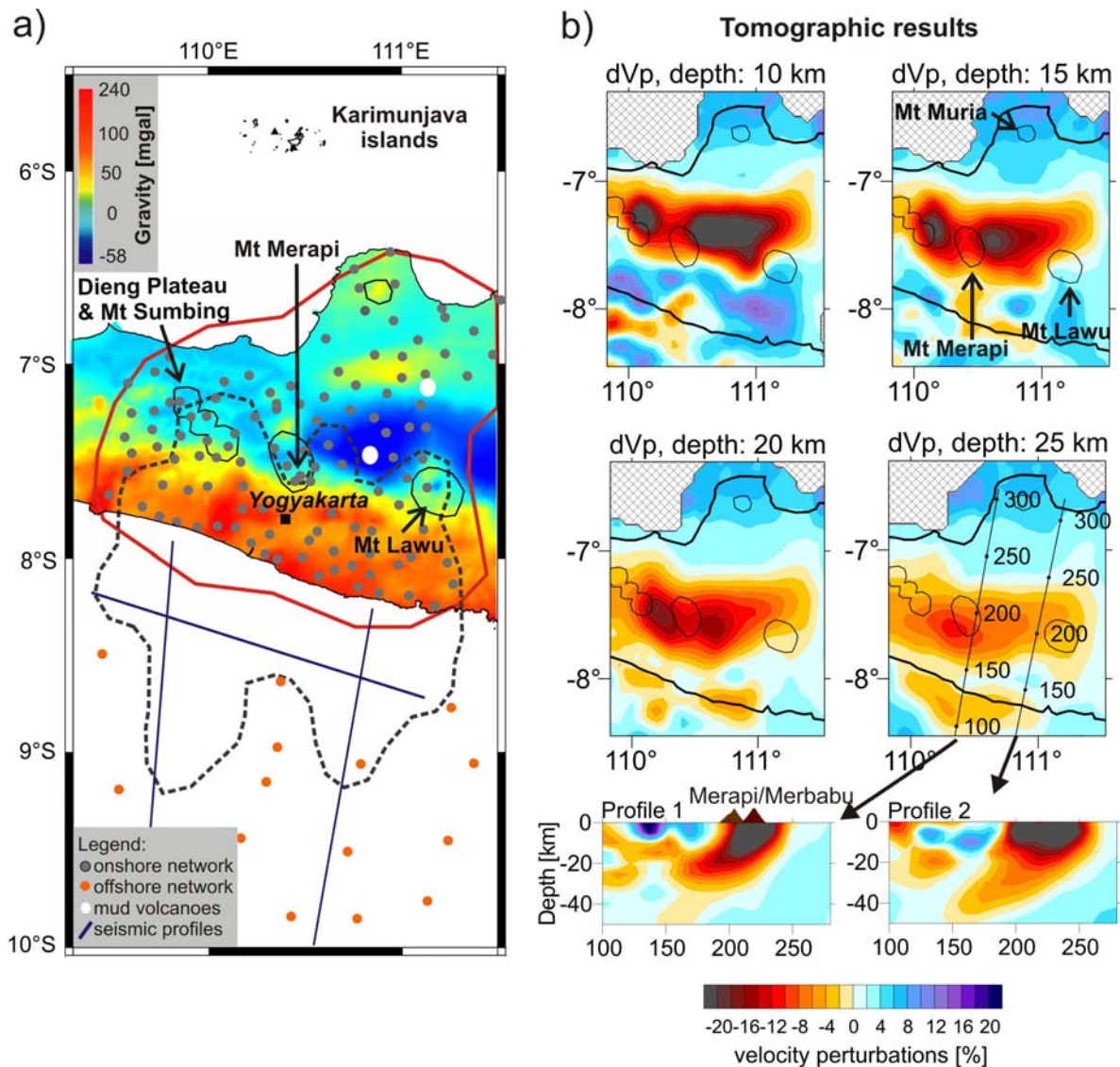


**Figure 8.1.** a) The MERAMEX seismic network superimposed over a gravimetric map (after Smyth et al. 2005) of Central Java. The area enclosed in red is covered by passive data and the area surrounded by a dashed black line is covered by active seismic data and are identified as areas with good recovery of 30 km size checkerboard anomalies at 5 km depth (Koulakov et al. 2007; Wagner et al. 2007). b) Tomographic results after the inversion of both active and passive seismic data. Open ellipses represent volcanoes labelled in 1a. The upper four diagrams are horizontal sections at 10, 15, 20 and 25 km depth, the bottom diagrams show vertical sections along profiles 1 & 2, showing P-velocity perturbations in percent.

Tomographic velocity lows beneath recognised caldera systems (Harrison & White 2004; Masturyono et al. 2001), correspond in size, amplitude and depth range to the identified anomaly. In addition, there is a strong gravity low present in the Kendeng zone of Central Java (Smyth 2005; de Genevraye & Samuel 1972; Untung & Sato 1978; Smith & Sandwell 1997; Waltham et al. 2006) (Figure 8.1a), with a similar amplitude as found at Toba caldera (Masturyono et al. 2001). The main distinction between the structures observed at documented large-volume magmatic systems (e.g. Taupo, Toba, etc.) and the anomaly in Central Java, is the lack of an associated caldera system and CCF eruptive products.

Given the absence of directly associated large-volume volcanic products, lavas and igneous inclusions from Merapi Volcano, an andesitic stratovolcano sited at the southern margin of the low-velocity anomaly, are utilised here as a probe into the crust of Central Java. In agreement with our geophysical results, geobarometric calculations using minerals contained within selected samples require the presence of crystallising melt in a zone spanning the crust and into the upper mantle, from ~3 km to 30 km depth (Figure 8.2). Geochemical and petrological evidence indicates that within this zone, there are melt bodies where magma mixing, crystallisation, crystal settling and assimilation occur. This suggests the anomaly is not one large body but potentially many interconnected smaller magma reservoirs. However, due to the resolution of our tomographic study (Koulakov et al. 2007; Wagner et al. 2007), individual structures of < 15 km size are not resolvable and thus appear as one large anomaly.

Igneous inclusions in lavas may preserve distinct records of crystallisation during ascent and have been identified in previous studies as fractionation residues reflecting crustal processes at arc volcanoes (Beard & Borgia 1989; Heliker 1995). Igneous inclusions from the 1994 and 1998 Merapi basaltic-andesite dome collapse deposits collected in 2002, are abundant, and are of two main types: 1) comagmatic enclaves and 2) plutonic lithic fragments. Magmatic enclaves are basaltic to basaltic-andesite, < 10 cm in diameter, with lobate contacts and occasionally, chilled margins with the host lava, and indicate the interaction of distinct magmas beneath the volcano. They contain crystals of plagioclase, clinopyroxene, and rare hornblende laths. The plutonic lithic fragments are typically < 10 cm in diameter and are subdivided, using modal mineralogy, into diorites with similar composition to the host basaltic andesite and mafic-amphibole to felsic gabbros. Both subgroups are medium to coarsely crystalline, with < 10 % vesiculated glass identified as a late stage addition from the

incorporation into Merapi host magma. The lithics occasionally possess mineral layering (Figure 8.2b) indicative of crystal settling and/or in-situ crystallisation in a magma reservoir. In both sub-groups pyroxene is diopside to augite with hornblende present as large laths > 5 mm often with pronounced reaction rims.

The whole rock Sr and Nd isotope ratios for enclaves and lithics analysed here largely fall within the range defined by data for recent Merapi volcanics (Gertisser 2003) (Figure 8.2). Given their mineralogy, texture and geochemistry, the inclusions analysed in this study are cognate or co-magmatic coarsely crystalline fragments of Merapi magmas that display increasing interaction with the crust with increasing degree of differentiation.

Geobarometric calculations (Nimis 1999; Johnson & Rutherford 1989) were carried out using electron microprobe analyses of pyroxene and amphibole crystals from enclaves and lithics. A range of pyroxene crystallisation pressures (Nimis 1999) from 200 to 1300 MPa ( $\pm 140$ ) was obtained, with a concentration of values between 400 and 700 MPa. Assuming a range of 200 to 1300 MPa, pyroxenes from these inclusions potentially crystallised as shallow as ~3 km beneath the summit to as deep as 31 km, with the bulk of crystallisation occurring in a diffuse zone in the mid to lower crust (Figure 8.2). Lacking an assemblage including quartz and biotite, the experimental Al in hornblende barometer (Johnson & Rutherford 1989) provides an upper limit for pressure. However, results using this barometer largely overlap with those obtained by pyroxene geobarometry, with a range of crystallization pressures for amphibole from 400 to 1600 MPa and the bulk of data falling between 500 and 800 MPa, suggesting crystallisation of Merapi magmas throughout the crust and upper mantle.

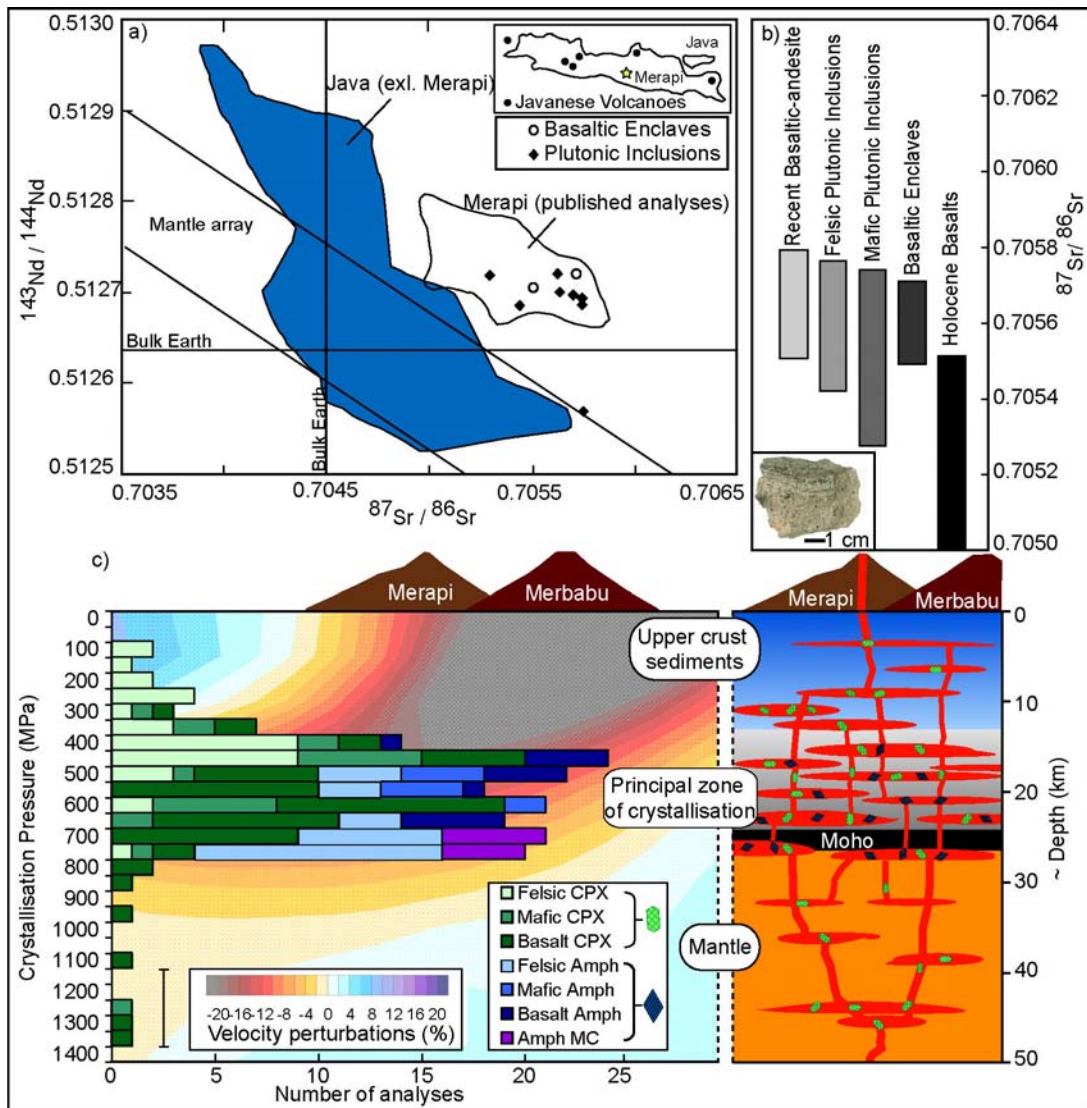


**Figure 8.2 a)** Sr vs Nd isotope plot showing recent Merapi inclusions and enclaves relative to Merapi and Java volcanics (from Gertisser & Keller 2003). Inclusions and enclaves largely plot within the Merapi data field indicating co-magmatic origin. **b)** Sr isotope variation diagram for inclusions plotted relative to recent Merapi basaltic andesite block-and-ash flow deposits and Holocene basalts (from Gertisser & Keller 2003). Inset photograph of a plutonic lithic fragment with fine mineral layering indicating settling or insitu growth in a magma reservoir. Stepwise progression in Sr ratio from more mafic to more felsic inclusions indicates increasing interaction with the crust and storage during ascent. **c)** Histogram of pressure calculations for pyroxene (CPX) and amphibole (Amph) crystals from enclaves, felsic and mafic plutonic inclusions, and amphibole megacrysts plotted relative to a profile through the tomographic anomaly. Cluster of crystallisation depths between 400 and 800 MPa are evident with a total range from 100 to 1350 MPa. A schematic cross section of a system of interconnected magma reservoirs spanning the crust and into the upper mantle beneath Merapi volcano is included.

### 8.3 Interpretation

We therefore propose that the large low-velocity anomaly in Central Java represents numerous bodies of solidified, crystal-rich, semi-molten and molten magma and adjacent crust. The exceptionally high amplitudes of the low-velocity anomaly in the uppermost 10 km of the crust may be amplified by sedimentary deposits and fluids in the Kendeng basin. However, these deposits could not produce the observed strong velocity and gravity lows in isolation, nor the continuity of the velocity anomaly to deeper depth sections of the crust and upper mantle (Koulakov et al. 2007). A viscoelastic combination of crystal-rich melt, solidified magma, and heated host rock and sediment would represent a comparatively impermeable matrix, acting as a barrier to ascending fluids and melts from the mantle wedge, redirecting flow along the bottom of the velocity anomaly, and feeding peripheral volcanism e.g. Merapi Volcano. Surface expressions of hydrothermal fluid flux are evident at Merapi (Commer et al. 2006) and in Central Java, including geothermal systems such as the Dieng Plateau and active mud volcanoes, like Kuwu and the Sangiran dome.

By combining geophysics and petrochemistry, our analytical approach to the deep magmatic structure of an active volcanic arc identifies a large low-velocity anomaly in the crust and upper mantle of Central Java. The  $V_p/V_s$  ratio of this body indicates the presence of liquid and given its extent down to the upper mantle, melt appears to be the most probable explanation. Petrology, geochemistry and geobarometry from Merapi inclusions and enclaves sourced from the periphery of this anomaly, confirms the presence of melt bodies spanning the crust and upper mantle of Java. It is thought that peripheral andesitic volcanism is a precursor to the formation of large volume silicic caldera systems (Price 2005) and is an indication that the crust must be thermally pre-conditioned before rhyolitic magmas typical of catastrophic caldera forming eruptions (CCF), are produced. Similar to Ruapehu volcano in New Zealand, thought to be in this pre-conditioning stage (Price 2005), Merapi lavas are high in groundmass silica (Schwarzkopf et al. 2006), indicating that rhyolite liquid is already present beneath the volcano. In conjunction, our results give strong evidence for the presence of a large magmatic system feeding Merapi volcano and the volcanic systems in Central Java, with numerous interconnected melt bodies resulting in a low-velocity anomaly of  $> 55000 \text{ km}^3$ . In time and given sustained heat flux through repeated injections of melt (Annen & Sparks 2002), this system has the potential to produce a catastrophic caldera forming eruption, providing us with a unique opportunity to monitor and study the evolution of a supervolcano in the making.



## 9. CONCLUDING REMARKS

Many geophysical and geological studies were performed along the Sunda subduction zone, which marks the collision zone between the Indo-Australian plate and Eurasia. The margin has a length of about 5000 km and extends along the islands of Sumatra and Java. The northern and central parts of the margin up to west Java are studied in great detail whereas the Java segment and the segments further to the east were poorly understood. The oblique subduction system along Sumatra and to the north has long been the center of scientific research in Indonesia. The northern and Sumatra segment up to West Java is characterized by higher seismic activity compared to Central Java. Especially after the December 26, 2004 Sumatra megathrust earthquake and tsunami, a number of scientific research project were initiated in this area.

In Central Java previous geophysical studies typically concentrated on the internal structure of Merapi volcano (Müller & Haak 2004; Müller et al. 2002; Wegler & Lühr 2001) leaving the deeper structure and the linkage to the subduction process out of the focus. With the amphibious MERAMEX project this gap of understanding the Central Java segment has been closed (or at least narrowed). The results presented in this work give new insights into the processes that link the subduction of the oceanic Indo-Australian plate beneath Eurasia and the active volcanism in Central Java:

1. A detailed velocity-depth model of the subduction zone offshore Central Java was developed together with A. Wittwer (IFM-GEOMAR) using wide-angle seismic, bathymetric and reflection seismic data. This model provides new findings on the tectonic setting of the subduction zone offshore Central Java and links the offshore with the onshore experiments of the MERAMEX project.
2. Two tomographic codes were used to invert the active, three-dimensional data set. The discussion of the results shows that forward models are indispensable to study the tectonic settings of subduction zones and that they are essential to verify tomographic results. In addition, this study proves the reliability of the tomographic results showing that both applied codes provide comparable images. Although code LOTOS-06 needs still further development and testing, it provides more attractive options to invert active seismic data compared to code 3DTH. I. Koulakov equipped his code with numerous routines for synthetic testing, plotting of velocity perturbations, and absolute velocities, routines to plot the ray coverage and ray density. Therefore, code LOTOS-06 is more comparable to a

user-friendly software package. In contrary, code 3DTH can be obtained as a package including all routines for the inversion. But all additional routines necessary for tomographic studies like plotting or synthetic testing need to be written by the user. Hence, if a user likes to perform tomographic studies of seismic refraction data, both codes obtain comparable results. But nevertheless, the more comfortable and faster way to obtain tomographic results is code LOTOS-06. Supplementary, code LOTOS-06 allows to process both active and passive seismic data simultaneously, which is especially advantageous if both data sets are available for the study area, as it was for Central Java.

3. The tomographic studies of the active seismic data detected a northeast-southwest elongated anomaly that separates the rigid forearc into two blocks. The eastern boundary of this anomaly coincides with the location of one of the most prominent fault zones in the area - the Opak River Fault trending N40°E. In-between the two rigid blocks, the northeast-southwest oriented anomaly is notably correlating with the hypocenter location of the destructive Java earthquake in May 2006. The aftershocks of this event cluster at the eastern edge of the elongated low-velocity zone.
4. The most important feature is a low-velocity anomaly with maximum amplitudes of over -30 % in P and S models obtained after the joint inversion of both active and passive seismic data. The low-velocity anomaly is located in the crust northwards of the volcanoes Sumbing, Merapi and Lawu. The main anomaly extends about 80 km in east-west, 30 km in north-south direction, and over 50 km in depth. It is inclined towards the slab, moves southwards and declines in amplitude with depth. The velocity perturbations and attenuation of P and S waves, the high Poisson's ratio of 0.3 of the anomaly, its correlation to a gravity low and the location in the active Sunda Arc lead to the following interpretation: The detected low-velocity anomaly is caused by multiple magma reservoirs and ascending feeder systems of the volcanic systems of Central Java.
5. Petrological and geochemical data from samples at the margin of the low-velocity anomaly (Chadwick 2007, personal communication) confirm the presence of melt spanning the crust of Central Java and indicate the potential for this feature to develop an explosive volcanic system. Given time and a sustained melt supply, this body has the potential to become the reservoir to a previously unknown super-volcano, similar to Toba caldera in Sumatra, Indonesia, Yellowstone caldera in USA or Taupo caldera in New Zealand and thus provides geoscientists with an unique opportunity to study the formation and development of such a large magmatic system long before an eruption.

**Future investigations:**

Up to now, the MERAMEX earthquake catalogue consists of about 500 picked events corresponding to about 40 % of the data set. Future work should include the picking of all events detectable in the data set, their relocalisation and the definition of the focal mechanisms and magnitudes. The earthquake focal mechanisms as well as well bore breakouts, and drilling-induced fractures (from local oil companies), in-situ stress measurements (like overcoring, hydraulic fracturing) and young geologic data (from fault-slip analysis and volcanic vent alignments) could be used as stress indicators to determine the tectonic stress orientation in the study area. These results could then be implemented in a three-dimensional finite element model aiming in visualizing the stress distribution off- and onshore Central Java. Supplementary, fluid pathways from the subducting oceanic crust to the volcanoes located in Central Java could be modeled.

Gravity modeling in three dimensions could be useful to understand the tectonic setting of the Java segment. An open question is here the origin of the basement high at the cross point of the two seismic profiles P18 and P19 and the structure of the low-velocity anomaly northward of the volcanic arc. How big is the influence of the sedimentary deposits in the Kendeng zone on the low-velocity and the negative gravity anomaly?

Nevertheless, with the existing data set, many open questions cannot be answered. Therefore, new field experiments might be appropriate:

Additional bathymetry data could be useful for the interpretation of the low-velocity anomaly dividing the forearc into two blocks and could enable to identify an extension of this anomaly and its accompanying fault zone in the offshore area. Such data could answer the question if this zone trends south–west to the basement high. Passive long time monitoring in Central and East Java could help to identify events correlating with magma and fluids rising upwards. Such a network could also answer the question if the low-velocity anomaly extends towards the east, because the low-velocity anomaly correlates notably with the gravity-low in Central Java and the gravity anomaly extends from Central to East Java. An open question is also if there is a linkage to the mud volcano near Porong, in the district of Sidoarjo, East-Java, which coincides with the eastern boundary of the negative Bouguer anomaly in the Kendeng zone of Java. Additional active reflection seismic experiments could reveal the structure of the magma body. Anyway, geophysical field experiments should be accompanied by geochemical and petrological studies because only combined studies will enable to interpret the low-velocity body in the crust of Central Java accurately.



## 10. REFERENCES

- Abercrombie, R. E., Antolik M., Felzer, K. & Ekström, G. 2001. The 1994 Java tsunami earthquake: Slip over a subducting seamount, *J. Geophys. Res.*, 106, 6595-6607.
- Ammon, C. J., Kanamori, H., Lay, T. & Velasco, A. A. 2006. The 17 July 2006 Java tsunami earthquake. *Geophys. Res. Lett.*, Vol. 33, L24308.
- Annen, C. & Sparks, R. S. J. 2002. Effects of repetitive emplacement of basaltic intrusions on thermal evolution and melt generation in the crust. *Earth Planet. Sci. Lett.*, v. 203 p. 937-955.
- Beard, J. S. & Borgia, A. 1989. Temporal variation of mineralogy and petrology in cognate gabbroic enclaves at Arenal volcano, Costa Rica. *Contrib. Mineral. Petrology*, v. 103, p. 110–122.
- Beauducel, F. & Cornet, F. H. 1999. Collection and three-dimensional modeling of GPS and tilt data at Merapi volcano, Java, *J. Geophys. Res.*, 104, B1, 725-736.
- Berthommier, P. C. 1990. Étude volcanologique du Merapi (Centre-Java), Téphrostratigraphie et chronologie - produits éruptifs. Thèse Doct., Université Blaise Pascal, Clermont-Ferrand, France, pp. 115.
- Berryman, J. G. 1995. Mixture theories for rock properties. In: T.J. Ahrens (ed.), A handbook of physical constants. American Geophysical Union, Washington D.C., 205-228.
- Bindeman, I.N. 2006. The secrets of supervolcanoes. *Sci. Am.*, 294, 28-33.
- Camus, G., Gourgaud, A., Mossand-Berthommier, P.-C. & Vincent, P.-M. 2000. Merapi (Central Java, Indonesia): An outline of the structural and magmatological evolution, with a special emphasis to the major pyroclastic events. *Volcanol. Geotherm. Res.*, 100, 139-163.
- Clift, P. & Vannucchi, P. 2004. Controls on tectonic accretion versus erosion in subduction zones: Implications for the origin and recycling of the continental crust, *Rev. Geophys.* 42 RG2001.
- Commer, M., Helwig, S.L., Hördt, A., Scholl, C. & Tezkan, B. 2006. New results on the resistivity structure of Merapi Volcano (Indonesia), derived from three-dimensional restricted inversion of long-offset transient electromagnetic data. *Geophys. J. Int.*, v. 167, 1172–1187.
- Curry, J. R., Shor, G. G., Raitt, R. W., Henry, M. 1977. Seismic refraction and reflection studies of crustal structure of the eastern Sunda and western Banda Arcs, *J. Geophys. Res.*, 82, 17, 2479-2489.

- Dziewonski, A. M., Ekström, G. & Salganik, M. P. 1995. Centroid-moment tensor solutions for April-June 1994, *Phys. Earth Planet. Inter.*, 88, 69-78.
- Fujii, Y. & Satake, K. 2006. Source of the July 2006 West Java Tsunami estimated from tide gauge records. *Geophys. Res. Lett.*, Vol. 3, L24317.
- de Genevraye, P. & Samuel, L. 1972. Geology of the Kendeng Zone (Central & East Java). Proceedings First Annual Convention, Indonesian Petroleum Association 17–30.
- Gertisser, R. 2001. Gunung Merapi (Java, Indonesien): Eruptionsgeschichte und magmatische Evolution eines Hochrisiko-Vulkans. *Thesis*.
- Gertisser, R. & Keller, J. 2003. Temporal variations in magma composition at Merapi Volcano (Central Java, Indonesia): magmatic cycles during the past 2000 years of explosive activity. *Volcanol. Geotherm. Res.*, 123, 1-23.
- Hamilton, W. 1979. Tectonics of the Indonesian region 1979: *United States Geological Survey Professional Paper*, v.1078, p.1-345.
- Hamilton, W. 1988. Plate tectonics and island arcs, *Geol. Soc. Am. Bull.*, 100, 1503-1527.
- Harrison, A. J. & White, R. S. 2004. Crustal structure of the Taupo Volcanic Zone, New Zealand: stretching and igneous intrusion, *Geophys. Res. Lett.* 31 (13): art. no.- L13615.
- Heliker, C. 1995. Inclusions in Mount St. Helens dacite erupted from 1980 through 1983. *Volcanol. Geotherm. Res.*, v. 66 p. 115-135.
- Hole, J. A. 1992. Nonlinear High-Resolution Three-Dimensional Seismic Travel Time Tomography. *J. Geophys. Res.*, Vol. 97, NO. B5. Pages 6553-6562.
- Hole, J. A., Clowes, R. M. & Ellis, R. M. 1992. Interface inversion using broadside seismic refraction data and three-dimensional travel time calculations. *J. Geophys. Res.*, Vol. 97, No. B3, p. 3417-3429.
- Hole, J. A., Clowes, R. M. & Ellis, R. M. 1993. Interpretation of three-dimensional seismic refraction data from western Hecate Strait, British Columbia: Structure of the crust. *Canadian Journal of Earth Sciences*, 30, 1440-1452.
- International Seismological Centre 2001, Bulletin Disks 1-9 [CD-ROM], *Internatl. Seis. Cent.*, Thatcham, United Kingdom.
- Jarrard, R. D. 1986. Relations among subduction parameters. *Rev. Geophys.*, v. 24, p. 217-284.
- Jellinek, M. A & DePaolo, D. J. 2003. A model for the origin of large silicic magma chambers: precursors of caldera forming eruptions. *Bull. Volcanol.*, 65, 363-381.

- Johnson, M. C. & Rutherford, M. J. 1989. Experimentally determined conditions in the Fish Canyon Tuff, Colorado, magma chamber. *J. Petrol.*, v. 30, p.711-737.
- Kennett, B. L. N., Engdahl, E. R. & Buland, R. 1995. Constraints on seismic velocities in the Earth from traveltimes, *Geophys. J. Int.*, 122, 108-124.
- Kennett, B. L. N. & Cummins, P. R. 2005. The relationship of the seismic source and subduction zone structure for the 2004 December 26 Sumatra-Andaman earthquake, *EPSL*, 239, 1-8.
- Kirby, S. H., Stein, S., Okal, E. A. & Rubie, D. C. 1996. Metastable mantle phase transformations and deep earthquakes in subducting oceanic lithosphere. *Rev. Geophys.*, Vol. 34, No. 2, Pages 261–306.
- Kopp, H., Klaeschen, D., Flueh, E. R., Bialas, J. & Reichert, C. 2002. Crustal structure of the Java margin from seismic wide-angle and multichannel reflection data. *J. Geophys. Res.*, 107 B2.
- Kopp, H. & Flueh, E. R. FS Sonne Fahrtbericht/Cruise Report SO 176&179. MERAMEX I & II. Merapi Amphibious Experiment. Cilacap-Hongkong & Jakarta-Cilacap, 18.05.-01.06.04 & 16.09.-07.10.04.- IFM-GEOMAR, 2004.- 206 S.- (IFM-GEOMAR Report / Berichte aus dem Leibliz-Institut für Meereswissenschaften an der Christian-Albrechts-Universität zu Kiel; 1).
- Kopp, H., Flueh, E. R., Petersen, C. J., Weinrebe, W., Wittwer, A. & Meramex Scientists 2005. The Java margin revisited: evidence for subduction erosion off Java, *Earth Planet. Sci. Lett.*, 242, 130-142.
- Koulakov, I., Sobolev, S. V. & Asch, G. 2006a. P- and S-velocity images of the lithosphere-asthenosphere system in the Central Andes from local-source tomographic inversion, *Geophys. J. Int.*, 167, 106-126.
- Koulakov, I. & Sobolev, S. 2006b. Moho depth and three-dimensional P and S structure of the crust and uppermost mantle in the Eastern Mediterranean and Middle East derived from tomographic inversion of local ISC data, *Geophys. J. Int.*, Vol. 164, issue 1, 218-235.
- Koulakov, I. & Sobolev, S. 2006c. A tomographic image of Indian lithosphere break-off beneath the Pamir-Hindikush region. *Geophys. J. Int.*, Vol. 164, 425-440.

- Koulakov, I., Bohm, M., Asch, G., Luehr, B.-G., Manzanares, A., Brotopuspito, K.S., Fauzi, Purbawinata, M.A., Puspito, N.T., Ratdomopurbo, A., Kopp, H., Rabbel, W., Shevkunova, E. 2007. P- and S-velocity structure of the crust and the upper mantle beneath Central Java from local tomography inversion, *J. Geophys. Res.*, submitted.
- Lasitha, S., Radhakrishna, M. & Sanu, T. D. 2006. Seismically active deformation in the Sumatra-Java trench-arc region: geodynamic implications. *Current Science*, Vol. 90, No. 5.
- Luetgert, J. H. 1992. MacRay: Interactive two-dimensional seismic raytracing for the Macintosh, *United States Geological Survey Open-File report 92-356*, p1-2.
- Maercklin, N., Riedel, C., Rabbel, W., Wegler, U., Lühr, B.-G. & Zschau, J. 2000. Structural Investigation of Mt. Merapi by an Active Seismic Experiment, In: *Deutsche Geophys. Gesellschaft-Mitteilungen*, Sonderband IV/2000, 13-16.
- Masturyono, McCaffrey, R., Wark, D. A., Roecker, S. W., Fauzi, Ibrahim, G. & Sukhyar 2001. Distribution of magma beneath Toba Caldera complex, north Sumatra, Indonesia, constrained by three-dimensional P wave velocities, seismicity, and gravity data. *Geochemistry, Geophysics & Geosystems*. 2.
- Masson, D. G. 1991. Fault patterns at outer trench walls, *Mar. Geophys. Res.* 13, 209-225.
- Mignan, A., King, G., Bowman, D., Lacassin, R. & Dmowska, R. 2006. Seismic activity in the Sumatra-Java region prior to the December 26, 2004 ( $M_w=9.0-9.3$ ) and March 28, 2005 ( $M_w=8.7$ ) earthquakes, *EPSL*, 244, 639-654.
- Moore, G. F., Curray, J. R., Moore, D. G. & Karig, D. E. 1980. Variations in geologic structure along the Sunda Fore Arc, Northeastern Indian Ocean, in: D. E. Hays (Eds.), *The tectonic and geological evolution of Southeast Asian Seas and Islands*, *Geoph. Mon.*, 23, 145-160.
- Müller, A. & Haak, V. 2004. 3-D modeling of the deep electrical conductivity of Merapi volcano (Central Java): integrating magnetotellurics, intuition vectors and the effects of steep topography. *Volcanol. Geotherm. Res.*, 138, pp 205-222.
- Müller, M., Hördt, A. & Neubauer, F. M. 2002. Internal structure of Mount Merapi, Indonesia, derived from long-offset transient electromagnetic data, *J. Geophys. Res.*, 107(B9), 2187.
- National Earthquake Information Center (NEIC) for Seismology, Denver, 2007.
- Newhall, C. G., Bronto, S., Alloway, B., Banks, N. G., Bahar, I. & Marmol, M. A. D. 2000. 10000 Years of explosive eruptions of Merapi volcano, Central Java: Archaeological and Modern Implications, *Volcanol. Geotherm. Res.*, 100, 9-50.

- Nimis P. 1999. Clinopyroxene geobarometry of magmatic rocks. Part 2. Structural geobarometers for basic to acid, tholeiitic and mildly alkaline magmatic systems. *Mineral. Petrol.*, v. 135:62-74.
- Peacock, S. A. 1990. Fluid Processes in Subduction Zones. *Science*, Vol. 248. no. 4953, pp. 329 – 337.
- Price, R. C., Gamble, J. A., Smith, I. E. M., Stewart, R. B., Eggins, S. & Wright, I. C. 2005. An integrated model for the temporal evolution of andesites and rhyolites and crustal development in New Zealand's North Island. *Volcanol. Geotherm. Res.*, v.140, p. 1-24.
- Rabbel, W., Beilecke, T., Bohlen, T., Fischer, D., Frank, A., Hasenclever, J., Borm, G., Kück, J., Bram, K., Druivenga, G., Lüschen, E., Gebrande, H., Pujol, J. & Smithson, S. B. 2004. Super-deep vertical seismic profiling at the KTB deep drill hole (Germany): Seismic close-up view of a major thrust zone down to 8.5 km depth. *J. Geophys. Res.*, 109, B09309, 20 p. (doi: 10.1029/2004JB002975).
- Ratdomopurbo, A. & Poupinet, G. 2000. An overview of the seismicity of Merapi volcano (Java, Indonesia), 1983 – 1994. *Volcanol. Geotherm. Res.*, 100, pp 193-214.
- Ruepke, L. H., Morgan, J. P., Hort, M. & Connolly, J. A. D. 2002. Are the regional variations in Central American arc lavas due to differing basaltic versus peridotitic slab sources of fluids? *Geology*, 30: 1035 - 1038.
- Schöffel, H.-J. & Shamita, D. 1999. Fine details of the Wadati-Benioff zone under Indonesia and its geodynamic implications. *J. Geophys. Res.*, Vol. 104, No. B6, pages 13,101-13,114.
- Špičák, A., Hanuš, V., Vaněk, J. 2005. Seismotectonic pattern and the source region of volcanism in the central part of Sunda Arc. *Journal of Asian Earth Sciences* 25, 583-600.
- Špičák, A., Hanuš, V., Vaněk, J. 2007. Earthquake occurrence along the Java trench in front of the onset of the Wadati-Benioff zone: Beginning of a new subduction cycle? *Tectonics*, Vol., 26, No. 1, TC1005.
- Schwarzkopf, L. M., Schmincke, H.-U., & Troll, V.R. 2001. Pseudotachylite on impact marks of block surfaces in block-and-ash flows at Merapi volcano, Central Java, Indonesia. *International Journal of Earth Sciences*, v. 90, 769–775 .
- Smith, W. H. F. & Sandwell, D. T. 1997. Global seafloor topography from satellite altimetry and ship depth soundings, *Science*, 277, p. 1957 – 1962.

- Smyth, H. R., Hall, R., Hamilton, J. & Kinny, P. 2003. Volcanic origin of quartz-rich sediments in East Java. *Indonesian Petroleum Association, Proceeding, 29th Annual Convention & Exhibition*, Jakarta, 541-559.
- Smyth, H.R., Hall, R., Hamilton, J. & Kinny, P. 2005. East Java: Cenozoic Basins, Volcanoes and Ancient Basement. *Indonesian Petroleum Association, Proceeding, 30th Annual Convention & Exhibition*, Jakarta, 251-266.
- Tiede, C., Camacho, A.G., Gerstenecker, C. & Fernández, J. 2005. Modelling the density at Merapi volcano area, Indonesia, via the inverse gravimetric problem, *Geochemistry, Geophysics, Geosystems (G3)*, 6(9), 1-13.
- Tregoning, P., Brunner, F. K., Brock, Y., Puntodewo, S. S. O., McCaffrey, R., Genrich, J. F., Calais, E., Rais, J. & Subarya, C. 1994. First geodetic measurement of convergence across the Java Trench, *Geophys. Res. Lett.*, 21, 19, 2135-2138.
- Tsuji, Y., Imamura, F., Matsutomi, H. Synolakis, C. E., Nanangm P. T., Jumadi, Harada S., Han, S. S., Arai, K. & Cook, B. 1995. Field survey of the East Java earthquake and tsunami of June 3, 1994, *Pure and applied geophysics*, Vol. 144, No. 3-4.
- Um, J. & Thurber 1987. A fast algorithm for two-point seismic ray tracing, *Bull. Seism. Soc. Am.*, 77, 972-986.
- Untung, M., & Sato, Y. 1978. Gravity and Geological Studies in Java, Indonesia: Geological Survey of Indonesia and Geological Survey of Japan, Special Publication, 6, 207 pp.
- Van Bemmelen, R. W. 1949. The Geology of Indonesia: The Hague, *Government Printing Office, General Geology*, v.1A.
- Van der Molen, I., & Paterson, M. S., 1979. Paterson Experimental deformation of partially-melted granite. *Contrib. Mineral. Petrol.*, 70, 299-318.
- Van der Sluis, A. & Van der Vorst, H. A. 1987. Numerical solution of large, sparse linear algebraic systems arising from tomographic problems, in: *Seismic tomography*, edited by G.Nolet, pp. 49-83, Reidel, Dordrecht.
- Vidale, J. E. 1990. Finite-difference calculation of traveltimes in three dimensions. *Geophysics*, 55, 521-526.
- Wagner, D., Koulakov, I., Rabbel, W., Luehr, B.-G., Wittwer, A., Kopp, H., Bohm, M., Asch, G. & the MERAMEX Scientists 2007. Joint Inversion of Active and Passive Seismic Data in Central Java. *Geophys. J. Int.*, doi: 10.1111/j.365-246X.2007.03435.x.

- 
- Waltham, D., Hall, R. & Smyth, H. R. 2006. Basin formation by volcanic-arc loading. GSA Special Paper: Formation and applications of the sedimentary record in arc collision zones (ed A Draut), in press.
- Wasserman, J. M., Ohrnberger, J. M., Scherbaum, F., Gossler J. & Zschau, J. 1998. Continuous Measurements at Merapi Volcano (Java, Indonesia) Using a Network of Small-Scale Seismograph Arrays, In: DGG-Mitteilungen, Sonderband III/1998, 81.
- Webb, S., and P. Courtial, 1996. Compressibility of melts in the CaO-Al<sub>2</sub>O<sub>3</sub>-SiO<sub>2</sub> system. *Geochim. Cosmochim. Acta*, 60, 75-86.
- Wegler, U. & Lühr, B.-G. 2001. Scattering behavior at Merapi volcano (Java) revealed from an active seismic experiment. *Geophys. J. Int.*, 145, 579-592.
- Westerhaus, M., Rebscher, D., Welle, W., Pfaff, A., Körner, A. & Nandaka, I. G. M. A. Deformation Measurements at the Flanks of Merapi Volcano. - in: DGG-Mitteilungen, Sonderband III/1998, 93-99.
- Wittwer, A., Kopp, H., Wagner, D., Flueh, E. R. & Rabbel, W. 2007. Crustal and upper mantle structure of the central Java subduction zone from marine wide-angle seismics. In preparation.
- Zhao D. 2000. Seismological structure of subduction zones and its implications for arc volcanism and dynamics, *Physics of the Earth and Planetary Interiors*, 3999, (2001) 1-18.



## APPENDIX A: Seismic sections

The airgun signals recorded at onshore receivers were sorted to receiver gathers. A bandpass butterworth filter with filter corners of 3-12 Hz and a linear moveout (reducing velocity) of 6 km/s was applied to the raw data to generate the images of the seismic sections presented in the following (see Figure A.1 for receiver locations). Eleven seismic sections represent receivers gathers of profile P19 (Figure A.2a, b, c, d), three examples are presented for signals emitted along the western dip line P18 (Figure A.3) and six sections are shown as examples for the eastern dip line P16 (Figure A.4a and b).

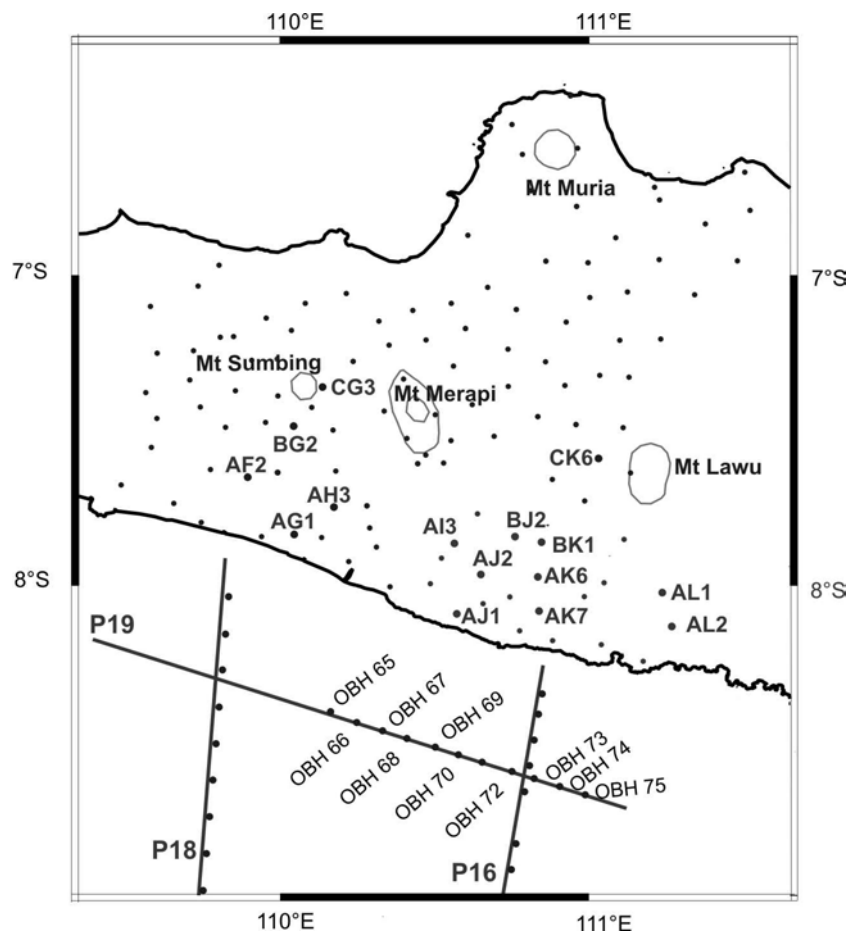


*Figure A.1: Onshore receiver locations of the seismic sections presented in Appendix A.*

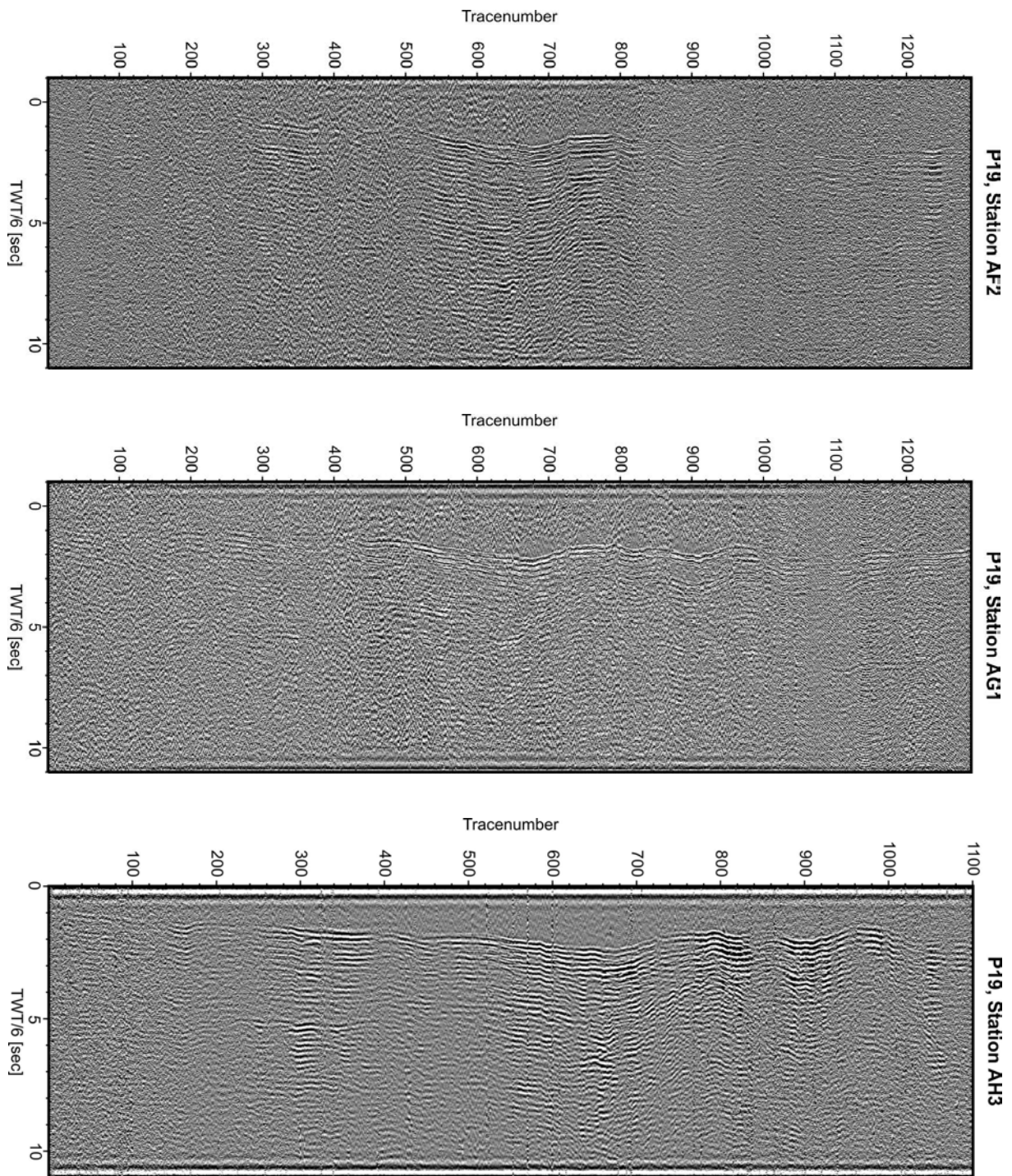


**Figure A.2a:** Seismic sections of the onshore stations AF2, AG1 and AH3 which are located close to the southern coast. The sections show the recorded airgun signals of the coast parallel profile P19.

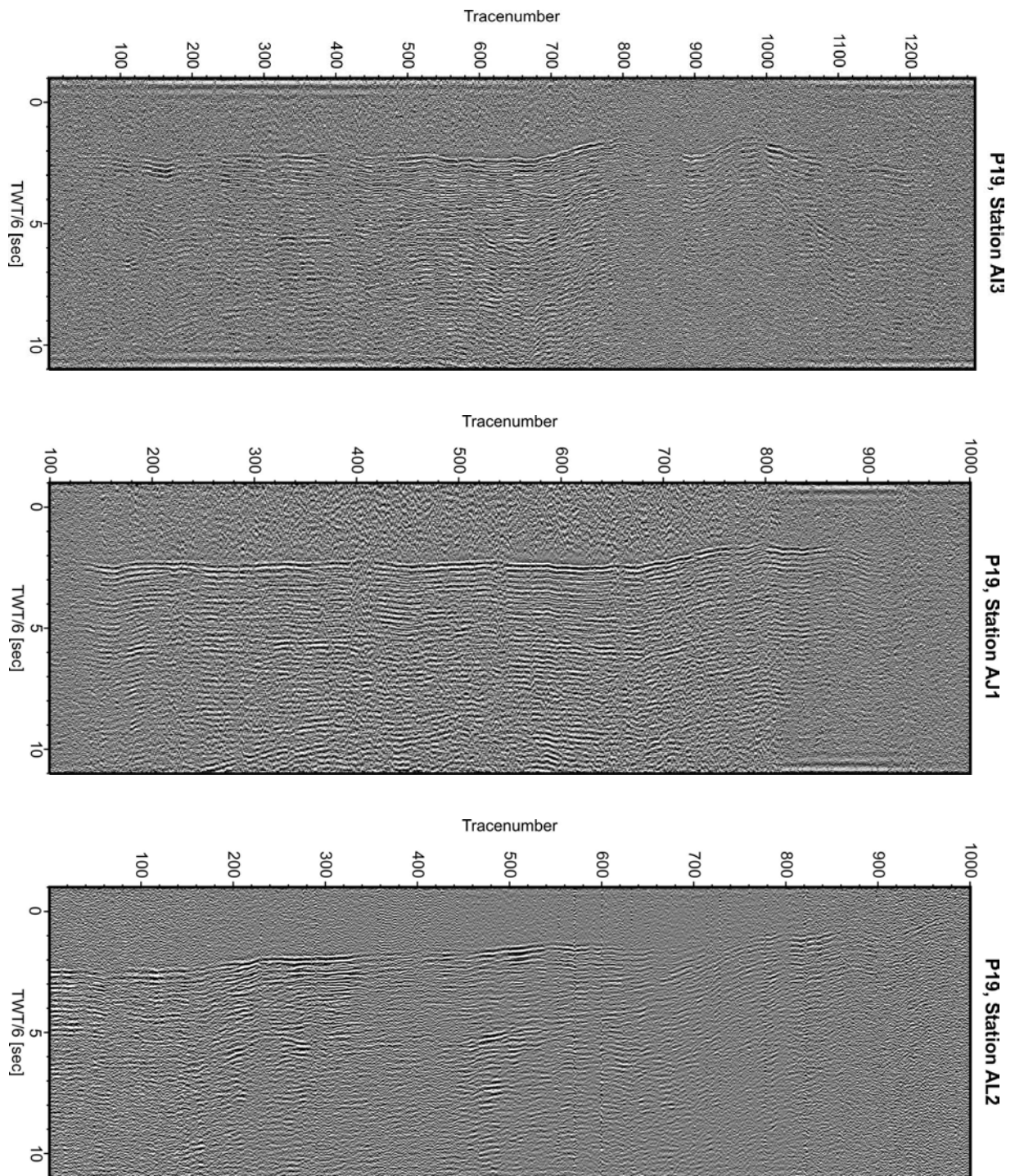


**Figure A.2b:** Seismic sections of the onshore stations AI3, AJ2 and AL2. They show the good data quality of the airgun profile P19 recorded onshore.

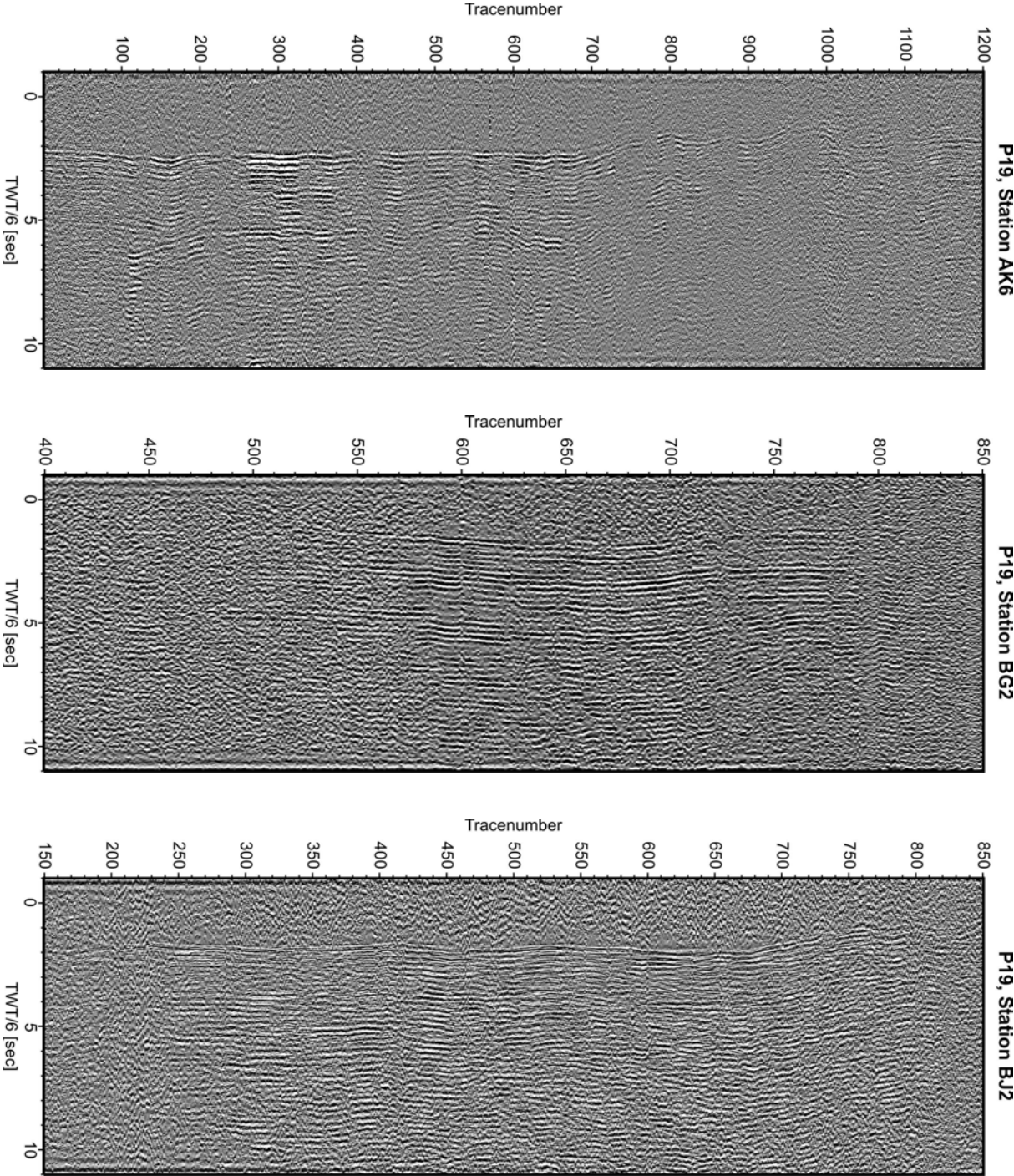


*Figure A.2c: Seismic sections of the onshore stations AK6, BG2 and BJ2 showing airgun signals of profile P19.*

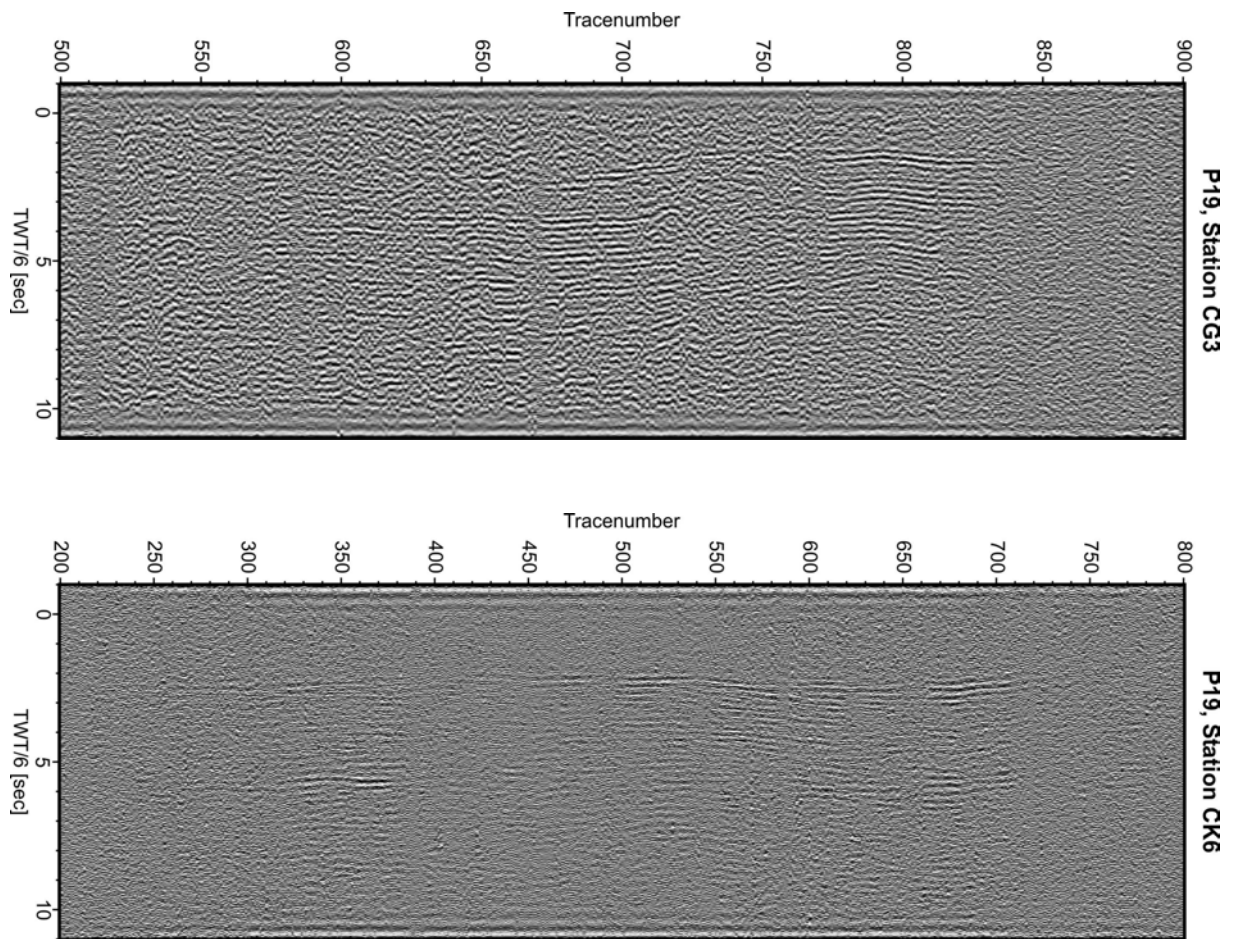


**Figure A.2d:** Seismic sections of the onshore stations CG3 and CK6. These stations represent the data quality for large offsets between offshore airgun shots along profile P19 and onshore receivers.

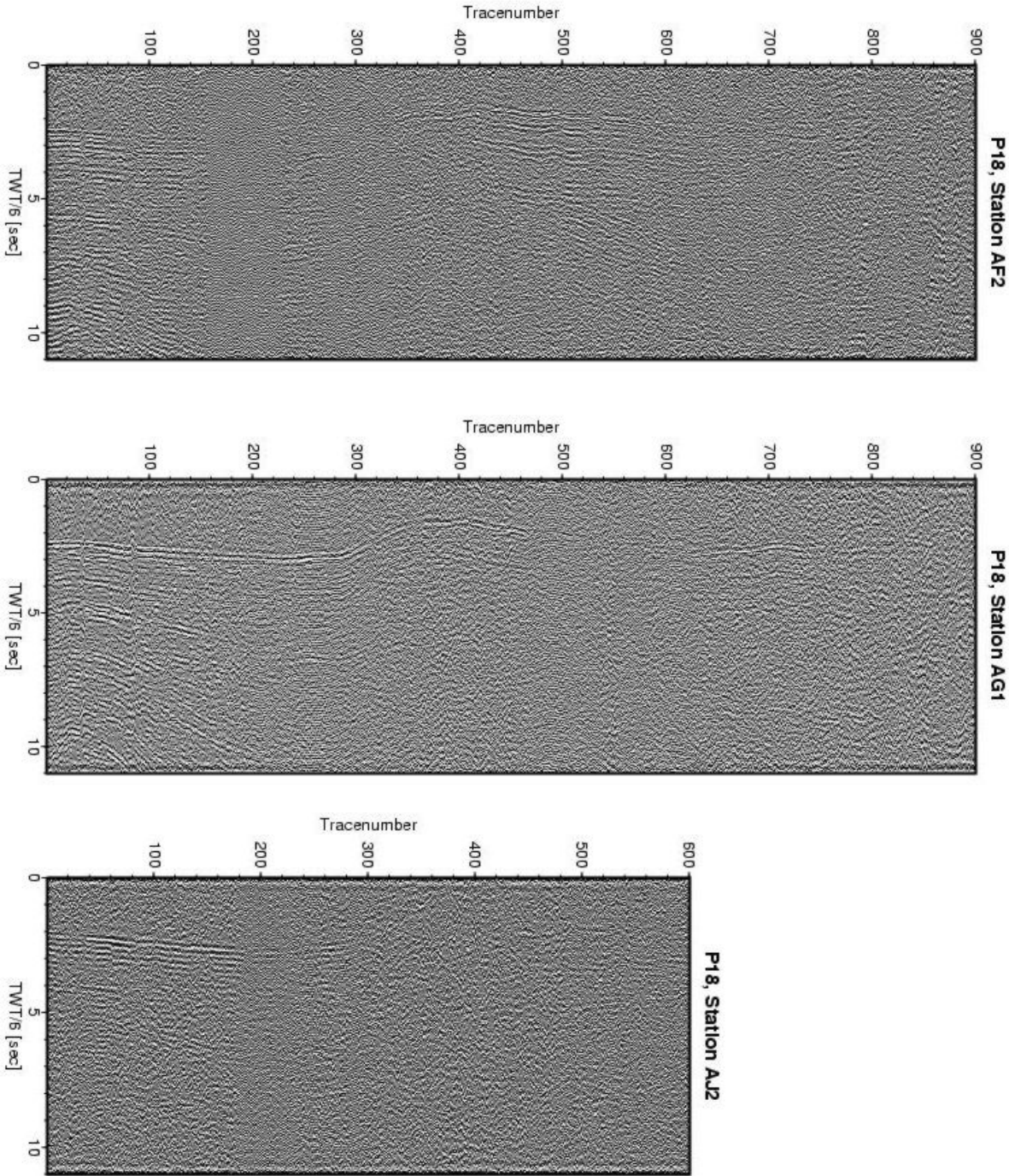


*Figure A.3: Seismic sections of the onshore stations AF2, AG1 and BJ2, having recorded airgun signals of the western airgun profile P18.*

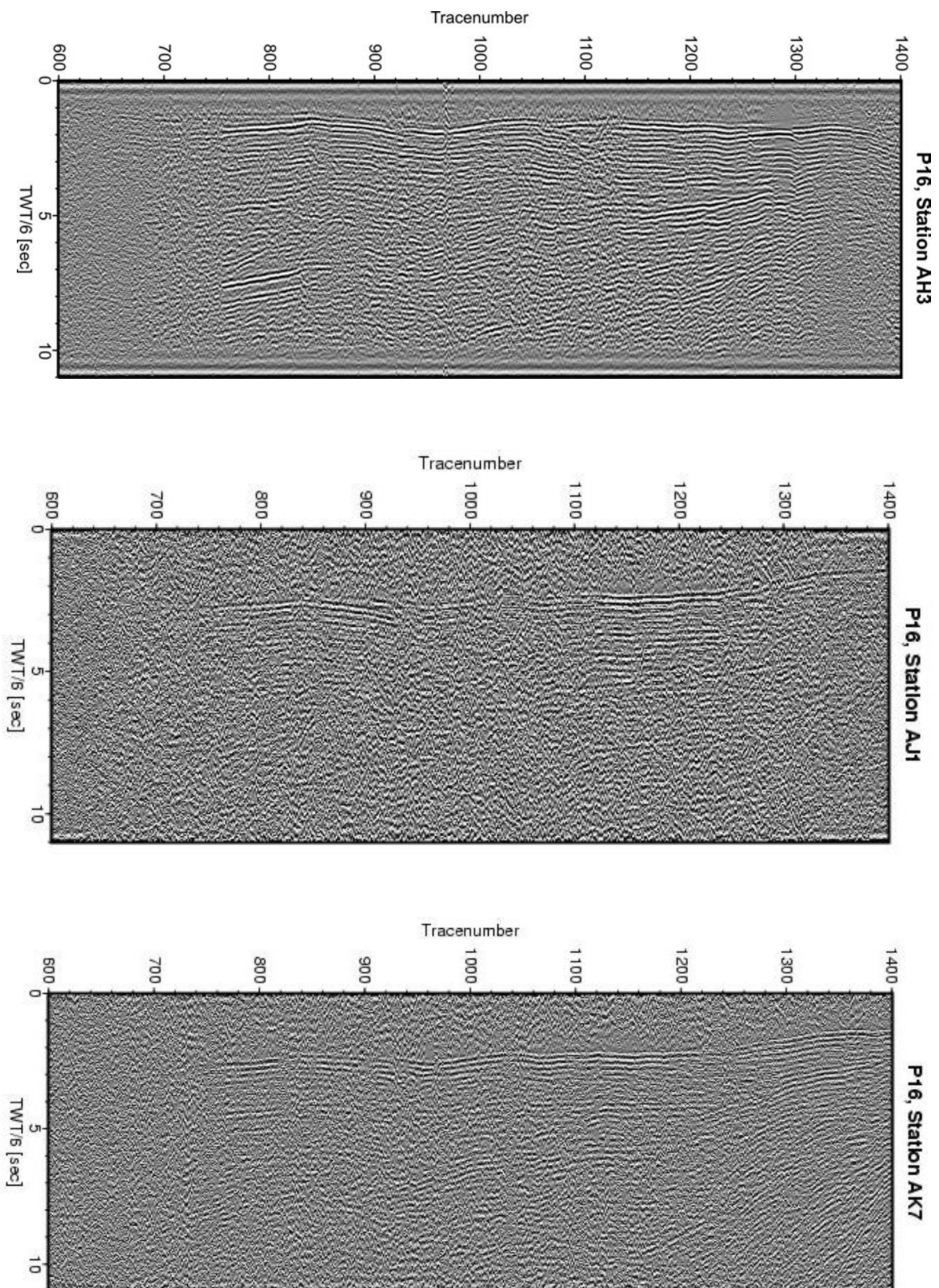


**Figure A.4a:** Seismic sections of the onshore stations AH3, AJ1 and AK7. They show the good data quality of the airgun signals emitted along profile P16.

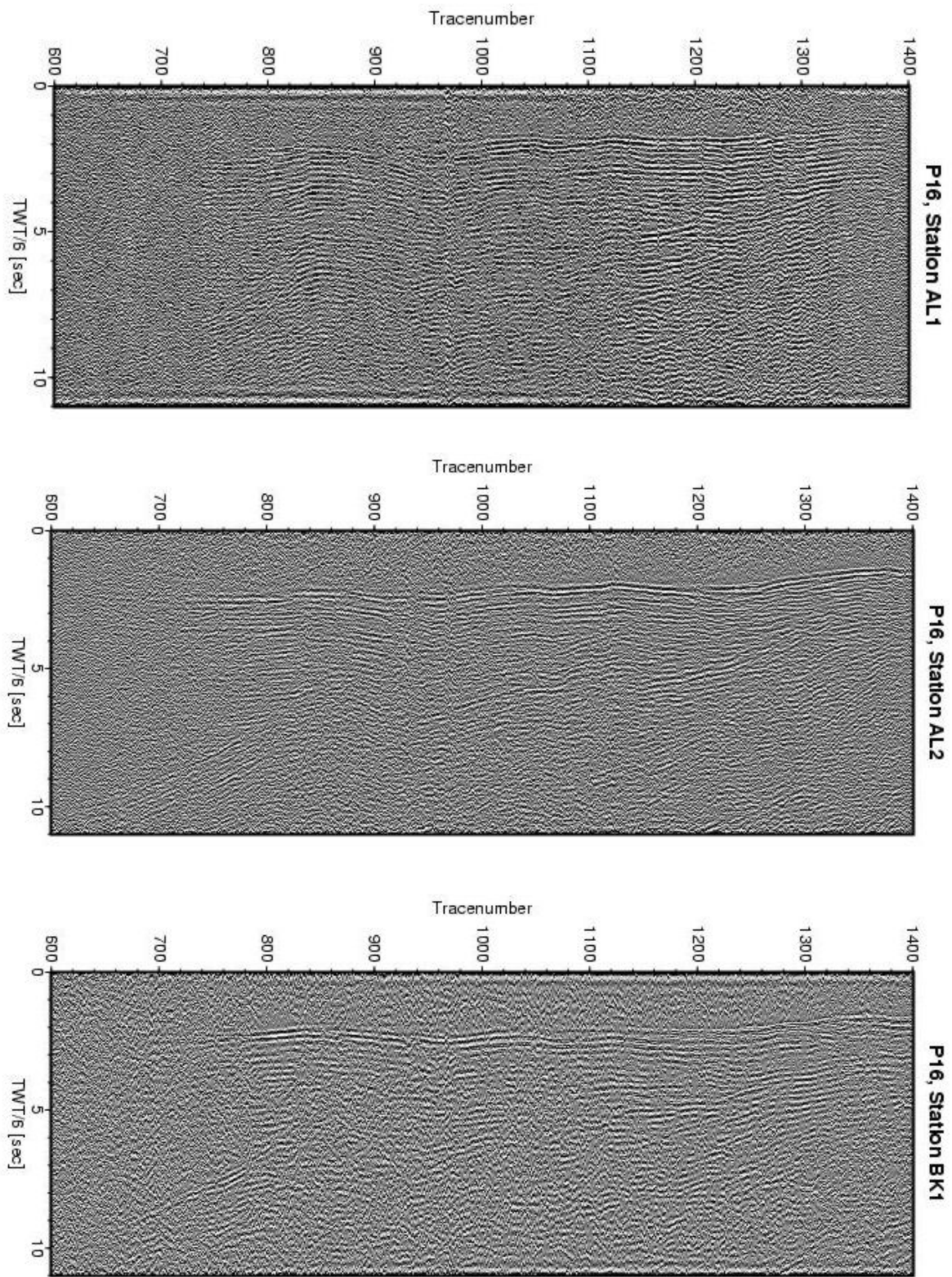


**Figure A.4b:** Seismic sections of the onshore station AL1, AL2 and BK1 showing airgun signals of profile P16.

## APPENDIX B: OBH stations

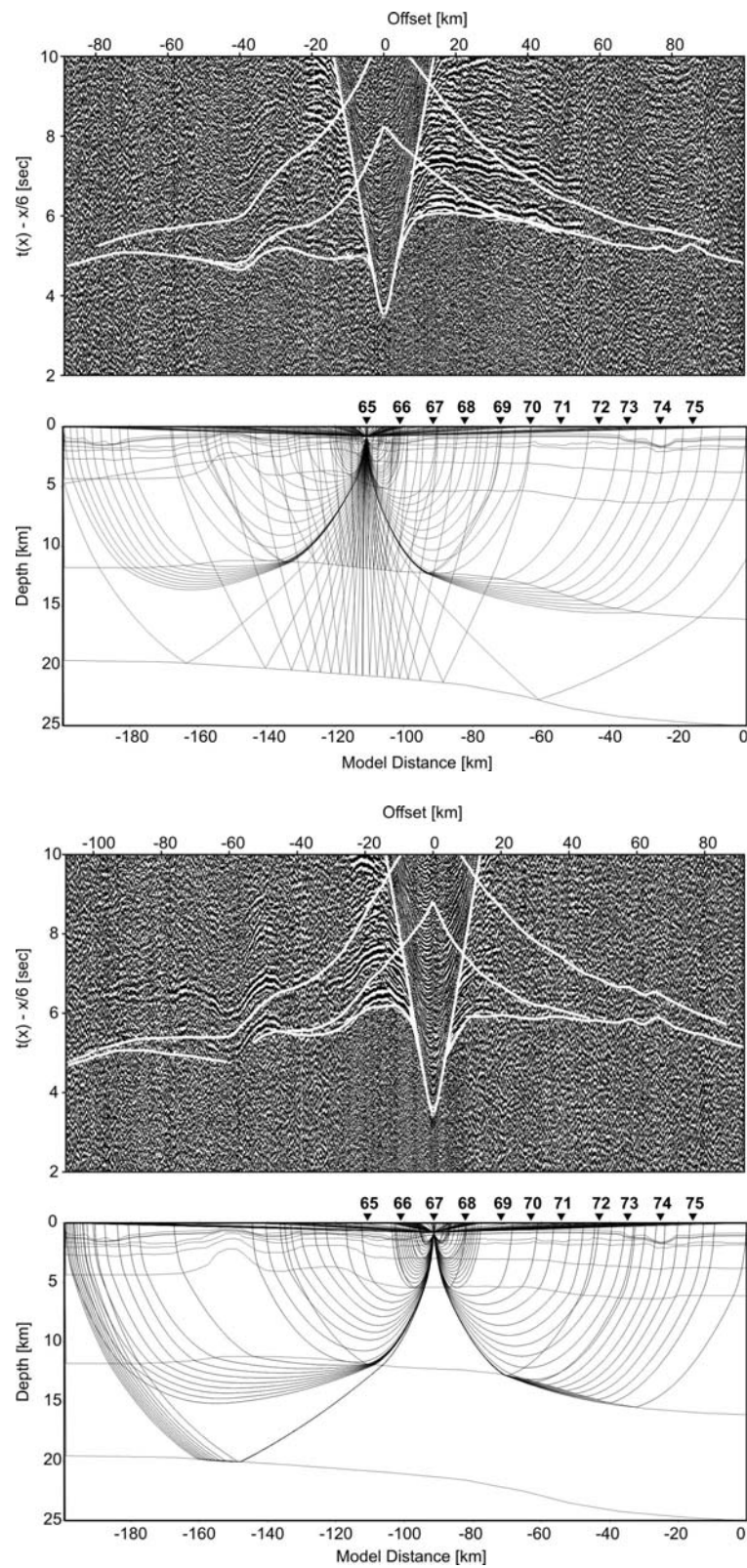


**Figure B.1:** OBH 65 (the upper two diagrams) and OBH 67 (the lower two diagrams) are located in the center of the coast parallel profile P19. The diagrams show the processed data and the model with the modeled ray paths respectively.

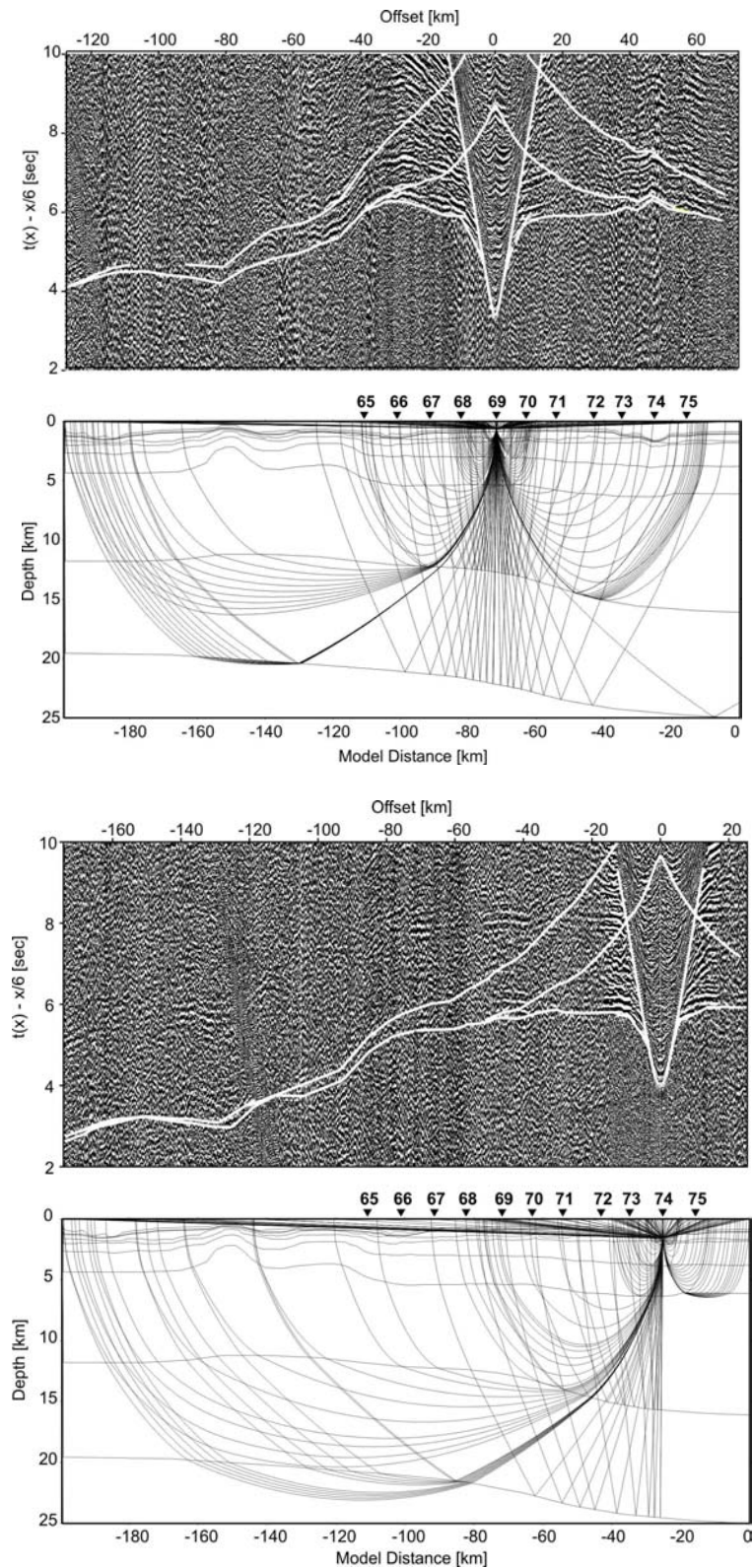


**Figure B.2:** OBH 69 (the upper two diagrams) and OBH 74 (the lower two diagrams) are located along the coast parallel profile P19. The diagrams show the processed data and the model with the modeled ray paths respectively.

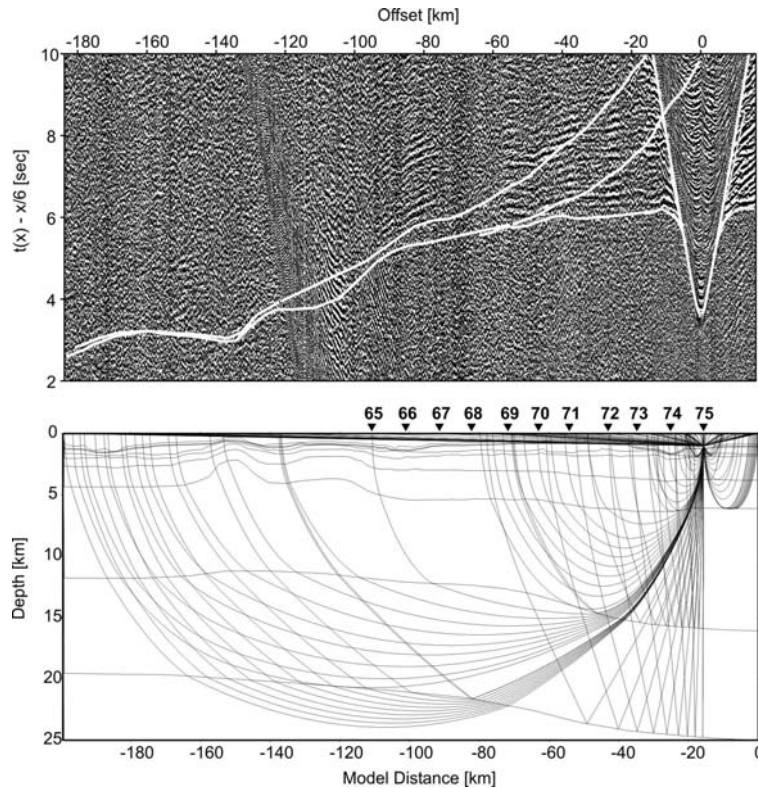


**Figure B.3:** OBH 75 is the easternmost OBH station of profile P19. The diagrams show the processed data and the model with the modeled ray paths respectively.

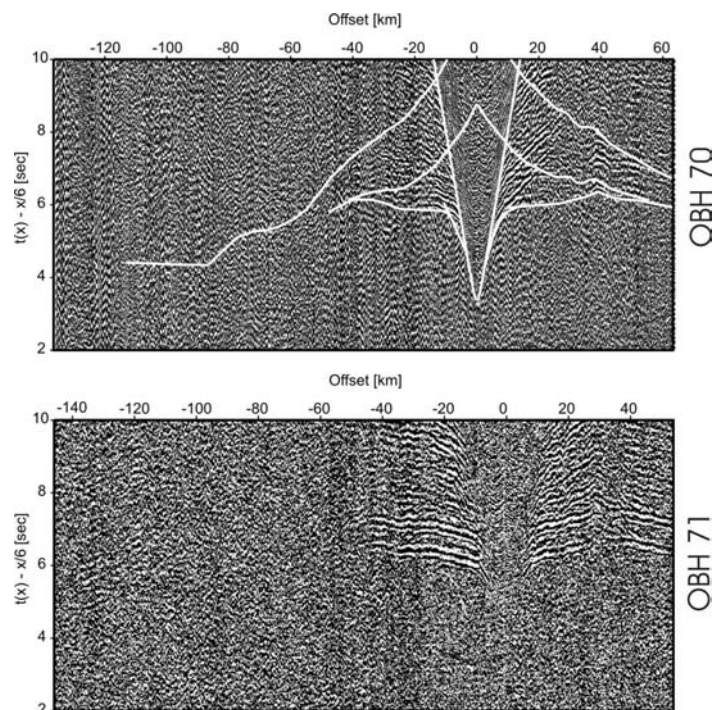


**Figure B.4:** The upper diagram shows the processed data of OBH 70 and the modeled ray paths. The lower diagram represents the processed data of OBH 71, which was not included in the modeling process of profile 19.



## APPENDIX C: Tables

*Table C1: Land receiver coordinates and station description for receivers located close to the south coast of Central Java.*

Station name	Latitude [°]	Longitude [°]	Elevation [m]	Begin of recording period	End of recording period	Station description			
AI1	-7.9955	110.4870	180	08.05.2004	04.10.2004	3031	EDL	MS	L4-3D
AI2	-8.0053	110.3560	390	09.06.2004	08.10.2004	3139	EDL	MS	T40
AI3	-7.8649	110.5643	250	07.05.2004	04.10.2004	3093	EDL	MS	L4-3D
AI4	-7.9125	110.5222	245	29.09.2004	05.10.2004	3092	EDL	MS	L4-3D
AJ1	-8.0925	110.5718	240	08.05.2004	07.10.2004	3076	EDL	MS	L4-3D
AJ2	-7.9659	110.6495	230	10.05.2004	04.10.2004	3035	EDL	MS	L4-3D
AH1	-7.9817	110.2929	40	07.05.2004	24.05.2004	3123	EDL	MS	L4-3D
AH2	-7.9238	110.2226	75	25.05.2004	08.10.2004	3123	EDL	MS	L4-3D
AH3	-7.7476	110.1749	400	07.05.2004	06.10.2004	3132	EDL	MS	L4-3D
AH4	-7.8115	110.2939	180	21.05.2004	05.10.2004	3087	EDL	MS	L4-3D
AH5	-7.7440	110.2810	170	13.07.2004	08.10.2004	3105	EDL	MS	T40
AK1	-7.9730	110.8344	232	11.05.2004	07.10.2004	3113	EDL	MS	L4-3D
AK2	-8.1475	110.7756	292	11.05.2004	07.10.2004	3067	EDL	MS	L4-3D
AK3	-8.0398	110.9838	210	12.05.2004	22.05.2004	3074	EDL	MS	L4-3D
AK4	-8.1790	110.8823	200	12.05.2004	07.10.2004	3069	EDL	MS	L4-3D
AK5	-8.0366	110.9842	230	22.05.2004	08.10.2004	3138	EDL	MS	T40
AK6	-8.0380	110.7436	423	02.09.2004	06.10.2004	3149	EDL	MS	L4-3D
AK7	-8.0839	110.8384	256	03.09.2004	06.10.2004	3097	EDL	MS	L4-3D
AK8	-7.9922	111.0480	529	08.09.2004	08.10.2004	3112	EDL	MS	L4-3D
AE1	-7.7362	109.6564	50	14.05.2004	05.10.2004	3109	EDL	MS	L4-3D
AE2	-7.6763	109.4866	50	07.06.2004	05.10.2004	3141	EDL	MS	L4-3D
AE3	-7.5556	109.5844	255	15.05.2004	05.10.2004	3106	EDL	MS	L4-3D
AF1	-7.8213	109.8334	42	12.05.2004	05.10.2004	3135	EDL	MS	L4-3D
AF2	-7.6511	109.8954	120	08.05.2004	05.10.2004	3061	EDL	MS	L4-3D
AF3	-7.7865	109.7447	50	19.05.2004	08.06.2004	3099	EDL	MS	L4-3D
AF4	-7.7974	109.7450	32	08.06.2004	05.10.2004	3099	EDL	MS	L4-3D
AG1	-7.8364	110.0464	215	12.05.2004	06.10.2004	3134	EDL	MS	L4-3D
AG2	-7.6340	109.9957	210	22.05.2004	05.10.2004	3148	EDL	MS	L4-3D
AG3	-7.8434	109.9403	40	28.05.2004	05.10.2004	3158	EDL	MS	L4-3D
AG4	-7.8425	110.1390	160	21.05.2004	06.10.2004	3100	EDL	MS	L4-3D
AL1	-8.0238	111.2370	633	08.09.2004	08.10.2004	3137	EDL	MS	L4-3D
AL2	-8.1328	111.2679	639	08.09.2004	04.10.2004	3033	EDL	MS	L4-3D
AL3	-8.2457	111.1751	380	10.09.2004	06.10.2004	3055	EDL	MS	L4-3D
AL4	-8.1917	111.0390	368	10.09.2004	06.10.2004	3059	EDL	MS	L4-3D

*Table C2: Land receiver coordinates and station description for receivers installed in the volcanic arc region of Central Java.*

Station Name	Latitude [°]	Longitude [°]	Elevation [m]	Begin of recording period	End of recording period	Station description			
<b>BH1</b>	-7.6315	110.1807	417	08.05.2004	06.10.2004	3072	EDL	MS	L4-3D
<b>BH2</b>	-7.5265	110.4107	1285	08.05.2004	29.09.2004	3054	EDL	MS	L4-3D
<b>BH2</b>	-7.5265	110.4107	1285	29.09.2004	04.10.2004	3140	EDL	MS	L4-3D
<b>BH3</b>	-7.4373	110.3370	885	11.05.2004	06.10.2004	3089	EDL	MS	L4-3D
<b>BI1</b>	-7.5803	110.4713	1125	08.05.2004	04.06.2004	3090	EDL	MS	L4-3D
<b>BI2</b>	-7.5328	110.5535	650	10.05.2004	04.10.2004	3057	EDL	MS	L4-3D
<b>BI3</b>	-7.6075	110.4453	830	25.08.2004	29.09.2004	3043	EDL	MS	T40
<b>BI3</b>	-7.6075	110.4453	830	29.09.2004	06.10.2004	3101	EDL	MS	T40
<b>BI4</b>	-7.6058	110.5296	582	11.05.2004	04.10.2004	3080	EDL	MS	L4-3D
<b>BJ1</b>	-7.7698	110.6387	154	10.05.2004	29.09.2004	3129	EDL	MS	L4-3D
<b>BJ1</b>	-7.7698	110.6387	154	29.09.2004	05.10.2004	3133	EDL	MS	L4-3D
<b>BJ2</b>	-7.8430	110.7601	230	11.05.2004	04.10.2004	3128	EDL	MS	L4-3D
<b>BK1</b>	-7.8614	110.8459	214	12.05.2004	04.10.2004	3034	EDL	MS	L4-3D
<b>BK2</b>	-7.6589	110.8809	132	27.07.2004	29.09.2004	3122	EDL	MS	L4-3D
<b>BK2</b>	-7.6589	110.8809	132	29.09.2004	05.10.2004	3142	EDL	MS	L4-3D
<b>BK3</b>	-7.7283	110.9860	304	15.05.2004	05.10.2004	3114	EDL	MS	L4-3D
<b>BG1</b>	-7.4254	110.1027	1300	01.07.2004	06.10.2004	3028	EDL	MS	L4-3D
<b>BG2</b>	-7.4868	110.0444	800	15.05.2004	06.10.2004	3121	EDL	MS	L4-3D
<b>BG3</b>	-7.3893	109.9938	1060	17.05.2004	07.09.2004	3033	EDL	MS	L4-3D
<b>BE1</b>	-7.3784	109.5666	270	17.05.2004	07.10.2004	3082	EDL	MS	L4-3D
<b>BE2</b>	-7.4621	109.6021	210	18.05.2004	06.10.2004	3083	EDL	MS	L4-3D
<b>BE3</b>	-7.3371	109.7087	570	18.05.2004	07.10.2004	3108	EDL	MS	L4-3D
<b>BF1</b>	-7.3719	109.8565	830	17.05.2004	07.10.2004	3058	EDL	MS	L4-3D
<b>BF2</b>	-7.4903	109.8246	525	17.05.2004	07.10.2004	3059	EDL	MS	L4-3D
<b>BF3</b>	-7.4750	109.9537	910	19.05.2004	31.08.2004	3060	EDL	MS	L4-3D

*Table C3: Land receiver coordinates and station description for receivers installed north of volcanic arc.*

Station Name	Latitude [°]	Longitude [°]	Elevation [m]	Begin of recording period	End of recording period	Station description			
CG1	-7.2699	109.9903	1866	13.05.2004	04.06.2004	3112	EDL	MS	L4-3D
CG2	-7.1772	110.0377	905	14.05.2004	27.09.2004	3066	EDL	MS	L4-3D
CG3	-7.3591	110.1386	990	15.05.2004	26.05.2004	3047	EDL	MS	L4-3D
CI1	-7.4500	110.5023	1070	11.05.2004	06.10.2004	3095	EDL	MS	L4-3D
CI2	-7.4174	110.6216	500	14.05.2004	02.09.2004	3097	EDL	MS	L4-3D
CI3	-7.2925	110.5610	500	15.05.2004	06.10.2004	3091	EDL	MS	L4-3D
CH1	-7.2740	110.2406	691	18.05.2004	04.10.2004	3049	EDL	MS	L4-3D
CH2	-7.2246	110.3530	993	18.05.2004	01.10.2004	3051	EDL	MS	L4-3D
CJ1	-7.5190	110.6924	201	19.05.2004	04.10.2004	3038	EDL	MS	L4-3D
CJ2	-7.3585	110.7383	230	19.05.2004	06.10.2004	3027	EDL	MS	L4-3D
CK1	-7.6377	111.1336	1190	19.05.2004	10.06.2004	3071	EDL	MS	L4-3D
CK2	-7.3549	110.9214	150	22.05.2004	01.10.2004	3104	EDL	MS	L4-3D
CF1	-7.2732	109.9087	1250	20.05.2004	07.10.2004	3079	EDL	MS	L4-3D
CF2	-7.1973	109.8503	1780	20.05.2004	16.06.2004	3137	EDL	MS	L4-3D
CE1	-7.2426	109.7201	1185	20.05.2004	07.10.2004	3117	EDL	MS	L4-3D
CE2	-7.2509	109.6025	700	21.05.2004	07.10.2004	3111	EDL	MS	L4-3D
CG4	-7.3599	110.1380	960	26.05.2004	04.10.2004	3047	EDL	MS	L4-3D
CE3	-7.1001	109.5816	651	05.06.2004	28.09.2004	3074	EDL	MS	L4-3D
CK3	-7.4916	111.1096	236	05.06.2004	07.10.2004	3102	EDL	MS	L4-3D
CG1	-7.2699	109.9903	1866	04.06.2004	10.08.2004	3136	EDL	MS	L4-3D
CK4	-7.4817	110.9580	126	07.06.2004	21.07.2004	3112	EDL	MS	L4-3D
CK1	-7.6377	111.1336	1190	10.06.2004	07.10.2004	3071	EDL	MS	T40
CK6	-7.5904	111.0306	427	12.06.2004	07.10.2004	3144	EDL	MS	L4-3D
CF3	-7.1996	109.8073	1600	16.06.2004	06.09.2004	3137	EDL	MS	L4-3D
CK4	-7.4817	110.9580	126	21.07.2004	07.10.2004	3107	EDL	MS	L4-3D
CJ3	-7.4558	110.8340	140	15.07.2004	07.10.2004	3146	EDL	MS	L4-3D
CG1	-7.2699	109.9903	1866	10.08.2004	08.10.2004	3136	EDL	MS	T40

*Table C3: Locations of the OBH station deployed along profile P19.*

<b>Station</b>	<b>Longitude [°]</b>	<b>Latitude [°]</b>	<b>Depth [km]</b>
<b>OBH 65</b>	110.16	-8.42	0.841
<b>OBH 66</b>	110.25	-8.44	1.052
<b>OBH 67</b>	110.33	-8.47	0.812
<b>OBH 68</b>	110.41	-8.49	0.727
<b>OBH 69</b>	110.50	-8.52	0.618
<b>OBH 70</b>	110.58	-8.55	0.576
<b>OBH 71</b>	110.65	-8.57	0.573
<b>OBH 72</b>	110.75	-8.60	0.631
<b>OBH 73</b>	110.82	-8.62	1.055
<b>OBH 74</b>	110.91	-8.65	1.599
<b>OBH 75</b>	110.99	-8.68	1.001

*Table C4: Number of picked first onsets at onshore receiver stations sorted after the airgun profiles P16, P18 and P19 along which the signals were emitted.*

<b>Onshore receiver</b>	<b>Profile 16 Number of picked first onsets [trace number]</b>	<b>Profile P18 Number of picked first onsets [trace number]</b>	<b>Profile P19 Number of picked first onsets [trace number]</b>
AE2		1-211	
AE3	977-1420	1-691	749-967, 1092-1289
AF1		1-230	
AF2	803-1392	1-1053	261-1290
AF3		1-291	
AF4		1-320	
AG1	814-1420	1-833	216-1290
AG2	868-1420	1-245	425-932
AG3		1-710	
AG4		1-370	
AH2	1051-1420	1-796	413-1290
AH3	645-1420	1-878	29-1290
AH4	1122-1368		
AH5	761-1420	1-1190	201-1290
AI1		1-1108	78-1290
AI2	760-1420	1-993	1-1290
AI3	773-1420	1-319	5-1197
AI4	736-1420	1-992	2-1290
AJ1	752-1420	1-253, 403-587	1-856
AJ2	760-1420	1-337	1-910
AK1	1129-1420		
AK2	742-1420	1-392	1-837
AK4	1079-1420		1-837
AK5	734-1420		1-958
AK7	732-1420	1-337	1-841
AK8	721-1420	1-659, 881-1189	1-745
AL1	792-1420		145-766
AL2	722-1420		1-616
AL3	658-1420		1-630
AL4	546-1420	1-1290	1-777
BG1		1-154	589-876
BG2		1-110	506-847
BH1	168-367	1-317	415-831
BJ2	753-1420		1-890
BK1	648-1420	115-350	1-1247
BK3	1026-1420		
CF1	790-1175		771-1095
CG1			525-854
CG2	956-1418		
CG3			517-1290
CG4			559-1239
CI3	1058-1420		
CK1	725-1420		126-800
CK3	758-1402		396-737
CK6	741-1420		148-801



## **ACKNOWLEDGEMENTS**

Many people have helped me in numerous ways during the preparation of this thesis.

First of all, I very much like to thank Prof. Dr. Wolfgang Rabbel for being the principal adviser during the last three years. His ideas, questions, suggestions, advices and criticism lead to the successful completion of this thesis.

The continuous support and advice of Prof. Dr. Heidrun Kopp is warmly acknowledged.

I would like to thank Dr. Ivan Koulakov for providing his tomographic code and his patience answering my questions. Thanks to Dr. John Hole for providing his tomographic inversion program.

Many thanks to Andreas Wittwer for his fast responses on all my emails and questions.

I'm grateful to Birger Lühr for his organization of the Marapi workshop and his connection to Valentin Troll. This led to a very nice working environment together with Jane Chadwick combining geophysical and geochemical results. Many thanks also to Jane – it is really nice to prepare a publication together with you.

Many thanks for the support of the Indonesian partners, the crew of RV Sonne, all people who assisted during fieldwork and Dr. Mirjam Bohm for her advice during the field work onshore Java.

Special thanks to Christoph, Susi, Martin and Nilay for their help in understanding the tomographic codes and their assistance.

Finally, many thanks to Michael and my family for their patience and support during the last years.

If there is anyone I have forgotten, I apologize and thank them.



## **CURRICULUM VITAE**

Name	Diana Wagner
Date and Place of Birth	October 17, 1977 in Kehl
Citizenship	German

### **Education**

1984-1988	Grundschule Kehl-Marlen
1988-1997	Einstein-Gymnasium Kehl, Abitur
1997-2003	Study of Geophysics at the Technical University of Karlsruhe, Diploma thesis: 'Contemporary tectonic Stress – derived from 6-arm Caliper logs'
2003-2004	Research Assistant at the Geophysical Institute of the Technical University Karlsruhe
since June 2004	PhD student at the Institute for Geosciences, Department of Geophysics, Christian-Albrechts Universität zu Kiel



Hiermit erkläre ich, dass ich die vorliegende Arbeit abgesehen von der Beratung durch den Betreuer nach Inhalt und Form meine eigene Arbeit ist, die ich ohne unzulässige Hilfe Dritter und ohne Benutzung anderer als der angegebenen Hilfsmittel angefertigt habe. Die aus anderen Quellen direkt oder indirekt übernommenen Daten und Konzepte sind unter Angabe der Quelle gekennzeichnet.

Diese Arbeit wurde in gleicher oder ähnlicher Form keiner anderen Prüfungsbehörde vorgelegt oder veröffentlicht.

Diana Wagner